UNIVERSITY OF CRETE

DEPARTMENT OF MATERIALS
SCIENCE AND TECHNOLOGY

Nanostructured Doped Nickel Oxide Thin Films Made by RF Sputtering as Hole Transfer Layers for Transparent Optoelectronic Devices

Master Thesis

Chrysoula Aivalioti

Supervising Professor: Nikos Pelekanos

Supervising Scientist: Elias Aperathitis

Microelectronics Research Group
Institute of Electronic Structure & Laser Foundation for
Research and Technology (FORTH)

Heraklion, 2021

CONTENTS

Abstract

The increasing energy consumption and consequently, the increase in air pollutants have led to phenomena such as global warming (greenhouse effect) with the well-known effects on the environment and human health. Buildings are responsible for consuming about 40% of the total produced energy, while windows are responsible for the loss of 10-25% of the thermal energy of buildings. A properly designed smart window can control and modulate solar heat and lighting and it is possible, at the same time, to produce and store solar energy. In the last years, there has been increasing interest in metal oxides due to their outstanding properties. The emerging class of wide gap oxide semiconductors can be fabricated as transparent solar cells, harvesting UV solar radiation, and integrated into optoelectronics as power producers. Thus, transparent solar cells can be used for energy-autonomous smart windows like electrochromics and/or tandem solar cells.

In this work, undoped NiO and Nitrogen (N) or Niobium (Nb) single or co-doped NiO thin nanostructured films were fabricated by rf sputtering by employing Ni and Ni-Nb targets in plasma containing % (Ar-O_2-N_2) gases. All films were p-type oxide semiconductors but only N-doped NiO films were transparent. The oxide layers were characterized by AFM, XRD, SEM-EDX, XPS, Hall-effect and UV-Vis-NIR spectroscopy and the optimum ones were used to demonstrate all oxide UV photovoltaics. Heterostructures based on metal oxides were fabricated, namely p-NiO/n-TiO_2 and the properties of the heterodiodes were investigated in the dark and as UV-sensitive solar cells. The layers of TiO_2 consisted of double mesoporous/compact TiO_2 films, as the ones used in high efficiency perovskite solar cells.

Περίληψη

Η αυξανόμενη κατανάλωση ενέργειας και κατά συνέπεια η αύξηση των ατμοσφαιρικών ρύπων έχουν οδηγήσει σε φαινόμενα όπως η υπερθέρμανση του πλανήτη (φαινόμενο του θερμοκηπίου) με τις γνωστές επιπτώσεις στο περιβάλλον και την ανθρώπινη υγεία. Τα κτίρια ευθύνονται για την κατανάλωση περίπου 40% της συνολικής παραγόμενης ενέργειας, ενώ τα παράθυρα ευθύνονται για την απώλεια του 10-25% της θερμικής ενέργειας των κτιρίων. Ένα σωστά σχεδιασμένο έξυπνο παράθυρο μπορεί να ελέγχει και να διαμορφώνει την ηλιακή θερμότητα και τον φωτισμό και είναι ταυτόχρονα δυνατή η παραγωγή και αποθήκευση ηλιακής ενέργειας. Τα τελευταία χρόνια, υπάρχει αυξανόμενο ενδιαφέρον για τα οξείδια μετάλλων λόγω των εξαιρετικών ιδιοτήτων τους. Η αναδυόμενη κατηγορία ημιαγωγών οξειδίου μεγάλου χάσματος μπορεί να κατασκευαστεί ως διάφανα ηλιακά κύτταρα, να συλλέγει την ηλιακή ακτινοβολία UV και να ενσωματωθεί στην οπτοηλεκτρονική ως παραγωγοί ενέργειας. Έτσι, τα διάφανα ηλιακά κύτταρα μπορούν να χρησιμοποιηθούν για ενεργειακά αυτόνομα έξυπνα παράθυρα όπως ηλεκτροχρωμικά ή/και αλλεπάλληλα ηλιακά κύτταρα.

Σε αυτήν την εργασία, νανοδομημένα υμένια NiO χωρίς προσμίξεις ή με προσμίξεις αζώτου (N) ή νιοβίου (Nb) ή συνδυασμό αζώτου και νιοβίου κατασκευάστηκαν με rf sputtering χρησιμοποιώντας στόχους Ni και Ni-Nb σε πλάσμα που περιέχει % (Ar-O_2-N_2) αέρια. Όλα τα υμένια ήταν ημιαγωγοί οξειδίου τύπου p, αλλά μόνο τα υμένια NiO με προσμίξεις N ήταν διαάφανα. Τα στρώματα οξειδίου χαρακτηρίστηκαν με AFM, XRD, SEM-EDX, XPS, Hall-effect και UV-Vis-NIR φασματοσκοπία και τα βέλτιστα χρησιμοποιήθηκαν για την επίδειξη όλων των φωτοβολταϊκών οξειδίων UV. Κατασκευάστηκαν ετεροδομές βασισμένες σε οξείδια μετάλλων, δηλαδή p-NiO/n-TiO_2 και οι ιδιότητες των ετεροδιόδων ερευνήθηκαν στο σκοτάδι και ως ηλιακά κύτταρα ευαίσθητα στην υπεριώδη ακτινοβολία. Τα στρώματα του TiO_2 αποτελούνταν από διπλά μεσοπορώδη/συμπαγή TiO_2 υμένια, όπως αυτά που χρησιμοποιούνται στα ηλιακά κύτταρα περοβσκίτη υψηλής απόδοσης.

Introduction

This master thesis was carried out for the Master of Science degree of Materials Science and Technology at the University of Crete. I would like to thank Dr. Elias Aperathitis, Principal Scientist of the Microelectronics Research Group, who was my supervising scientist, for his help, guidance and valuable knowledge providing me during my master thesis. I would also like to thank Prof. Nikolaos Pelekanos, Professor of Materials Science and Technology Department at the University of Crete who was my supervising professor, for the opportunity he gave me to work on this project. Moreover, I would like to thank Prof. Constantinos Stoumpos, an Associate Professor of Materials Science & Technology Department at the University of Crete for his valuable advice and help. In addition, I would like thank Prof. Ioannis Remediakis for his advice and his participation in my three member committee. I would like to thank Ms. Maria Androulidaki for UV photo measurements and her guidance for optical measurements, Ms. Katerina Tsagaraki for SEM photos, EDX measurements and her guidance for AFM measurements and Ms. Maria Kayambaki for her guidance for electrical measurements. Also I would like to thank Prof. Eleutherios Hliopoulos for his guidance for Hall measurements, Dr. Zacharias Viskadourakis for Seebeck measurements, Dr. Emmanuel I. Spanakis for XPS measurements and Mr. Athanasios Kostopoulos for the preparation of substrates in the clean room area and measuring their thickness. Furthermore, I would like to thank especially Emmanouil Manidakis for the preparation of TiO_2/FTO/glass samples in Chemistry Department and the valuable help which has provided me and the entire Microelectronics Research Group for the great cooperation. Finally, I would like to thank my parents because I would not have achieved anything without them.

Chapter 1 - *State of the art*

In the last years there had been increasing interest in metal oxides due to their outstanding properties and potential applications in electronic and optoelectronic devices. Nickel oxide (NiO) is an earth abundant semiconductor and it has a rock salt crystalline structure (NaCl). NiO is a p-type oxide semiconductor and its p-type conductivity is due to non-stoichiometric defects such as Ni vacancies and oxygen interstitials. Because of its hole dopability (p-type behavior), conductivity, high chemical stability and combined with the wide band gap energy (3.1-3.8 eV), it is the most widely used p-type transparent conductive oxide [1],[2].

There is a wide range of methods of NiO fabrication. Some of them are expensive, like atomic layer deposition (ALD) and chemical vapor deposition (CVD) and some others are less expensive like physical vapor deposition (PVD), electron beam evaporation or vacuum evaporation [3]–[5]. There are also cheaper fabrication techniques like spin-coating, screen printing, spray pyrolysis, or sol-gel [4][6][7]. In some cases well-defined and controllable geometries are required which can be obtained by photolithographic techniques for oxide based optoelectronic applications, and for achieving it dry (solid state) methods are used and one of them is the physical vapor deposition technique of sputtering [8].

NiO has found a lot of applications as a coating or single layer due to its chemical stability and non-toxicity. Some of these applications are sensing [9], microbatteries [10], photo-bio-catalysis [11]–[13] and transparent optoelectronics such as smart windows [14], ultra-violet (UV) photodetectors [15] and photovoltaics (PVs). In PVs, NiO has been used in conventional PVs as well as ultra-violet PVs, in addition to perovskite PVs, in which it is used as a hole transport layer [16]–[19].

The as-deposited NiO presents an O-rich NiO phase. Increasing the percentage of oxygen gas in Ar plasma, the resistivity and transmittance of NiO is decreased [20]. Previous works had shown that a film grown in pure oxygen plasma had minimum resistivity (ρ) of 1.6×10^{-2} Ω·cm, a visible transmittance (T) of 40% and energy band gap almost 3.2 eV. While a film, which was grown at 30% oxygen in Ar plasma, had shown a higher transmittance of 54%, a band gap of about 3.3 eV and a resistivity of 1.1×10^{-1} Ω·cm. This dependence of transmittance and resistivity on the amount of oxygen during the sputtering process has be explained in terms of the amount of Ni^{3+} in Ni-O structure[20].

Moreover, NiO film deposited from NiO target on substrate with 0% oxygen content had a polycrystalline structure and small grain size [21]. With the introduction of oxygen gas in plasma, NiO had cubic phase, a preferential orientation to (200) and larger grain size. By increasing of oxygen content it showed compressive strain and it gradually turned into tensile strain which leaded to the narrowing of band gap. The band gap of NiO decreased to 3.12 eV with the increase of oxygen. X-ray photoelectron spectroscopy showed that the Ni^{+3}/Ni^{+2} ratio can explain the origin of p-type NiO. The ratio increased from 1.32 to 2.63 by increasing the oxygen content from 0% to 100% in plasma, which caused more defects, oxygen interstitials and nickel vacancies [21].

NiO has attracted attention because its properties can be improved with doping. Some dopants which have been used are: Al [22], Li [23], Cu [24], Nb [25], N [26], also co-doping has been reported, such as Li-Al [27], Li-Mg [28] and Cu-N [29]. In this project, NiO has doped with nitrogen (N), niobium (Nb) and co-doping nitrogen and niobium.

The nitrogen is one of the best anionic dopants because it can change the properties of NiO by altering the band gap structure. Previous works had shown that the obtained diffraction peaks of N-doped NiO were consistent with the NiO face centered cubic structure [30]. No secondary phases like nickel nitride were observed indicating the purity of the deposited samples. Generally, when N is doped with metal oxides, there is a possibility for the formation of a secondary nitride phase in the product [31]. The preferential plane of N-doped NiO films was the (200) one [30]. Also it was observed that the thickness of grains decreased with the increase in N doping.

The transmittance of N-doped NiO decreased due to the degradation in the crystalline quality caused by the nitrogen incorporation. Moreover the energy gap of undoped NiO was 3.50 eV while the energy gap of N-doped NiO was 3.41 eV because the bands of 2p states of nitrogen were within the band gap of NiO[30]. Finally theoretical predictions had shown that nitrogen doping induce 2p impurity states into the bandgap- which narrows the bandgap significantly [32].

In the case of Nb doped NiO, XRD results had shown that doping with Nb the intensity of NiO peaks were decreased and no other Nb related peaks were noticed. From optical measurements had been noticed that the optical band gap for the prepared films decreased from 3.60 to 3.48 eV by Nb doping

[33]. Moreover the NiO lattice parameter was found to decrease for Nb doped NiO films compared to undoped NiO due to the lower ionic radius of Nb^{5+} compared to Ni^{2+} [25].

As mentioned NiO is a p-type semiconductor with a wide bandgap between 3.5 eV and 4.0 eV. The properties of NiO make it a promising material for solar cells. Similarly, TiO_2 is a desirable material for harvesting solar energy due to its optoelectronic properties, high affordability and stability. A pn junction can be created when a p-type semiconductor (NiO) and a n-type semiconductor (TiO_2) are placed in contact. In previous works, I-V characteristics at room temperature in the dark showed that the forward current of the cells increased slowly with increasing voltage. Moreover the the formed junction had rectification properties since the dark J-V plots were similar to the Shockley diode characteristics. The solar cell fabricated from this diode exhibited the short-circuit current (I_{sc}) of 16.8 mA and the open-circuit voltage (V_{oc}) of 350mV [34].

The N-doped NiO has been used in a lot of applications, such as hole transport layer for perovskite solar cells, sensors, electrochromic applications, batteries and photo-catalysis. On the other hand niobium doped NiO has been used until now only in photo-catalysis and sensing. It has not been used in transparent optoelectronics such as smart windows, ultra-violet (UV) photodetectors and photovoltaics (PVs). The purpose of this project is to investigate the effect of nitrogen or niobium as single dopants and nitrogen and niobium as co-dopants on the optical, structural, surface and electrical properties of NiO, as well as their potential application in heterojunction diodes. Firstly undoped NiO films made in different deposition conditions will be presented with their optical, structural, surface and electrical characterization. Afterwards N-doped NiO (NiO:N) and niobium doped NiO (NiO:Nb) with their corresponding characterization results will be presented, as well as results on double doped NiO films (NiO:Nb-N). Finally, undoped and doped NiO films with optimum properties were chosen for the fabrication of NiO/TiO_2 heterodiodes and their characterization/properties will be presented in the last section.

Chapter 2 – *Sputtering Technique*

2.1 Introduction

The sputtering technique is a vacuum process which is used for the deposition of thin films on a substrate. It can be used in conductors, semiconductors, insulators and alloys. It differs from method of sublimation as the deposited material does not need to be heated.

2.2 The Sputtering Process

The sputtering is generally a natural process that can be compared to a collision of a steel ball with a wall. As a result, the ball removes some parts of the wall, but these parts retain their chemical and physical composition. If the process continues, the surfaces, which are close to the collision, are covered by a thin layer of wall.

In the sputtering the steel balls are ionized atoms. The wall is a piece of material and is called target. The sputtering process takes place in a vacuum chamber. The chamber contains the substrate and the target material to be deposited. When the chamber vacuum is satisfactory ($<10^{-6}$ mTorr), a gas is introduced into the chamber. The process of sputtering begins when the gas is ionized by the potential difference which develops between two electrodes of anode and cathode, that is, target - substrate. The positively charged atoms of gas react with the atoms of the target with a force and in this way is removed material. The gas atoms are not absorbed by the target but fall violently on it, like steel balls on a wall, and extract material from it. As the chamber is under vacuum the atoms are permanently deposited on everything in the chamber and especially on the substrate.

The above explanation is too simple and does not take into account various relevant parameters such as: ion kinetic energy, electronic structure of atoms, plasma molecules, the target or even substrate. The principles of sputtering process will be explained in detail below.

2.3 Different Types of Sputtering Technique

There are basically two kinds of sputtering technique, one is Direct Current (DC) sputtering and the other is Radio Frequency (RF) sputtering technique. In this master thesis RF sputtering was used and it is analyzed below.

2.3.1 RF Sputtering Technique

In RF sputtering a voltage between the cathode (target) and the anode (substrate) is developed and the electrons are repelled from the cathode. Then they collide with the atoms of the gas, creating ions and new electrons. The positive ions are accelerated toward the target, they collide with the target, in resulting the sputtering of target. After the collision of positive ions with the target, atoms removed from the target surface and they are transported to the substrate as seen in fig. 2.1.

Except from the atoms, electrons are also emitted because of the interaction of ions with the target surface. These electrons are known as the secondary electrons and the amount of them depends on the properties of the target material, the energy and the type of bombarding particles. They are necessary for the ionization of the gas and the maintenance of the discharge. The electrons and negative ions are moved from the target to the substrate, which with the reflected neutral argon atoms will arrive at the substrate and they start the growth of the film.

The plasma is determined by the deposition parameters such as the gas pressure, target-substrate distance, and target bias voltage. Control of these parameters is essential to modify the structural properties of film, its composition and mechanical characteristics. The thermal and energetic conditions at the substrate surface influenced by the different plasma species determine the elementary processes (adsorption, diffusion, and chemical reactions) as well as the microstructure and stoichiometry of the film growth. Functional properties of the thin films are largely determined by the intrinsic coating features, which defined not only by the material properties but, to a large extend, also by the thin film growth mechanism. Passing through several stages, adsorption and increase film thickness, a defined film structure is formed [35].

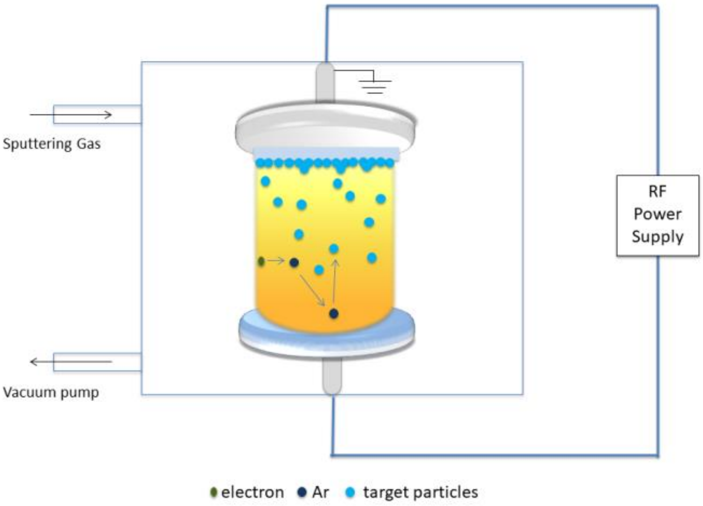

Fig. 2.1: A schematic form of RF Sputtering

2.3.2 RF Magnetron Sputtering Technique

The principle of operation of RF magnetron sputtering technique is similar to the RF sputtering technique. The only difference between the magnetron and other sputtering systems is that behind the target is a rod-shaped magnet whose north and south poles are spaced apart. The dynamic lines of the magnetic field originating from the north pole are directed towards the space between the two electrodes, they are curved and one part of them is parallel to the level of the target in the space between the two electrodes. Finally, the magnetic field returns to the south pole perpendicular to the target surface as seen in fig. 2.2. In this way the dynamic lines close. Therefore, electrons, which do not eject vertically from the target surface, often causing heating of the target and chamber, follow circular orbits. This increases the useful length of their orbit, so in the area above the target there are more elements in the plasma. It results in the probability of hitting to the target is greatly increased, even by an order of magnitude compared to RF Sputtering. So, deposits can be made at even 100 times lower pressure or at shorter distance between the target and substrate. Therefore,

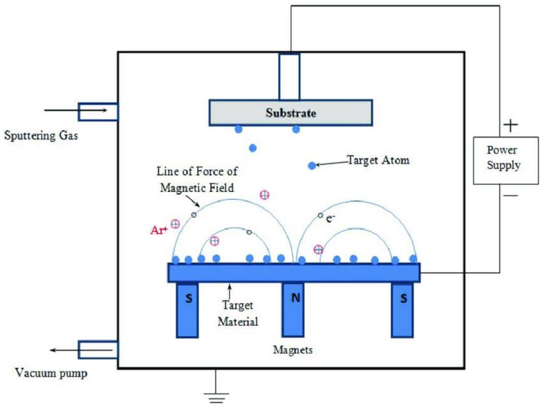

Fig. 2.2: Schematic form of Magnetron Sputtering [36]

due to the lower pressure, the probability of collision of the removable elements from the target with plasma atoms decreases and thus they reach the substrate with greater energies. So the deposition rate increases [37].

2.4 Parts of RF Sputtering

2.4.1 Chamber

The whole process of sputtering takes place in a cylindrical stainless steel chamber. The Sputtering system, which is used in this experimental process, contained three different targets and a rotating support system of holders, where each holder (substrate) can be placed on top of each target. Underneath the target there is a water cooled system. RF power is applied to the electrodes of targets and the holders are grounded.

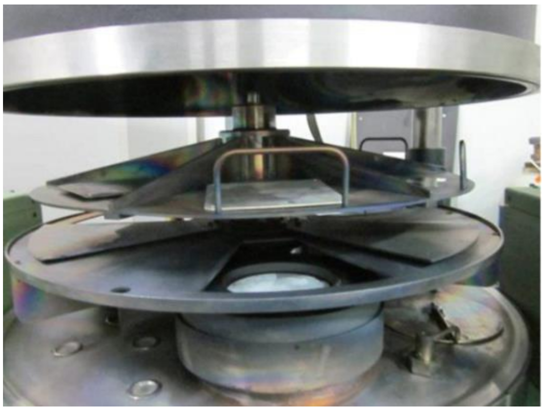

Fig. 2.3: The chamber of RF Sputtering System

The material of target could be insulator, metal or composite semiconductor as well as oxide. The atoms, which are on the surface of the target, are subject to bombarding by rapidly moving particles. The atoms are removed from the target and deposited on one or more substrates located a short distance above the target, in this way a film is formed. Inside the chamber, a suitable vacuum has been created, such that the atoms, which have sputtered from the target surface, are able to be transported to the substrate.

The achievement of a large number of fast particles, which will bomb the target, is carried out by immersing the target in plasma. The plasma contains positive ions and electrons and it is created between the two electrodes of target (cathode) and substrate (anode). A high negatively voltage is developed on the target in order to attract the positive ions from the plasma to the target surface. In this way, the desired deposition rate, the appropriate thickness and quality of thin films on the substrate can be achieved.

The creation of plasma is achieved on the one hand by injecting inert or any other re-active gas into the chamber which is already under low pressure and on the other hand in the existence of an electron, which with the help of high voltage, will create the initial ionization of the gas. In these experiments Ar has the role of inert gas. In addition, the assumption of electron existence can always be made when there is no obvious external cause, because on the one hand cosmic secondary radiation constantly causes weak ionization of the gas and on the other hand collisions due to thermal motion of the gas, cause ionization[37].

2.4.2 Plasma

The plasma is a homogeneous mixture, in a fluid state, consisting mainly of protons, electrons and neutrons, without being composed of atoms. Plasma behaves like a body without distinct chemical properties, although it contains in the form of impurities a small percentage of ionized atoms and molecules. It is an electrically neutral body with high electrical conductivity, due to the free protons (p+) and electrons (e-).

The sputtering plasma for the deposition of films is achieved on the one hand by injecting inert gas (Ar) into the chamber, which is kept at low pressure and on the other hand by assuming the existence of an electron, which with the help of high power we apply, creates the initial ionization of the gas. The ions bombard the target, resulting in the extraction of material from the target and electrons that contribute to the maintenance of the plasma. Also, many electrons reconnect with the plasma ions, so emitting photons, giving the plasma its characteristic color depending on the ionized gas.

2.4.2.1 The Properties of Plasma

Every gas, under normal conditions, usually behaves as an insulator, that is, as a bad conductor of electricity. However, with increasing temperature, its conductivity also increases, due to the ionization that occurs with the increasing frequency of collisions between molecules. At some temperature the gas, although completely ionized, is externally electrically neutral, since the number of positive particles is equal to the number of negative particles. At even higher temperatures ionization proceeds inside the nuclei (when it is not pure hydrogen) and in this way the plasma is formed. The study of its properties is independent of its original chemical composition, since the concept of chemical composition stops to exist. The existence of complex interactions between its species requires the introduction of statistical methods.

In each gas there are only elastic and inelastic collisions and the total frequency of collisions is equal to the sum of the elastic and inelastic frequencies. In elastic collisions the kinetic energy of each particle remains as kinetic energy, but in contrast to inelastic collisions a percentage is consumed for quality changes, such as when a photon collides with a bound electron. In this case the change of energy converts the bound electron to free electron and the phenomenon is characterized as photionization.

2.4.3 Vacuum Systems

Each sputtering system has a vacuum system which performs two basic functions. The vacuum system pumps the chamber up to a satisfactory low pressure (between 10^{-7} and 10^{-6} mTorr) and maintains the vacuum in the chamber during sputtering operation at a pressure 5mTorr, while the gas is continuously introduced into the chamber. During the initial pumping of the chamber, the vacuum pumps have to deal with the gases that remain in the chamber and the gases that are eliminated due to adsorption at the permanent parts of the chamber such as the walls, the target and the substrate. The base pressure, which is achieved in the chamber, depends on the rates of outgas of the various chamber parts, provided that there are no leaks.

The rate of elimination of gases is measured in $\text{Torr}\cdot\text{sec}^{-1}$ units and is related to the pressure (P) and the pumping speed (S), when the pressure does not change, according to the formula $Q = (P \times S)$. Thus, in an RF sputtering system with a chamber, which consists of a cylinder with stainless steel base and top, the rate of elimination of adsorbed gases is generally between $6\text{x}10^{-4}$ and $6\text{x}10^{-5}$ $\text{Torr}\cdot\text{sec}^{-1}$. Finally, a substrate, that has not yet been deposited, increases the elimination rate and can reach up to ~ 10^{-4} $\text{Torr}\cdot\text{sec}^{-1}$. During the process of sputtering, and in particular when evacuation occurs, all surfaces, which are in contact with the evacuation, will expel absorbed gases at a faster rate than normal.

All the above rates of elimination of adsorbed gases are in case the system is pumped satisfactorily and the pressure remains constant. In case the pressure inside the chamber must reach the value of 760 Torr to open the chamber, the introduction of atmospheric air is avoided because it has a high content of water vapor. For this reason nitrogen gas is introduced into the chamber.

It should be noted that, although the system pumps the chamber at pressures up to 10^{-7} mTorr, it is possible to find in it foreign impurities such as water vapor, hydrocarbons, etc. When the system is maintained at high pressures, most of the residual gas is water vapor which is constantly released from the walls of the chamber and other parts. Water vapor can also react with the target material going to the substrate. Thus the residual gases can not only prevent the creation of thin films from clean targets, but also create great and unpredictable consequences in that sputtering operation where thin films with impurities are sought. The pumping system of the specific RF sputtering, which was used, consists of the diffusion pump and the rotary pump.

2.4.3.1 The Diffusion Pump

The diffusion pump is one of the most popular high vacuum pumps in sputtering systems due to its reliability, simplicity and low cost. This pump does not operate mechanically. At its bottom there is suitable oil which is heated, evaporates and rises upwards. The oil molecules are forced to pass through thin nozzles on its walls and to be directed downwards at high speed, taking with them lighter molecules of air. When the hot oil comes in contact with the walls of the tank, which are kept cool by the circulation of water, they condense and return to the bottom of the tank, following the same cycle again. In this way the gas molecules are concentrated at the bottom of the pump which is connected to a mechanical (rotary) pump.

Fig. 2.4: The Diffusion Pump

The pressures are smaller than 10^{-5} mTorr so the main component in the gases, which remain in the chamber, is water vapor. A liquid nitrogen trap is used so that the partial pressure of the water vapor is very low. This liquid nitrogen trap is placed between the diffusion pump and the high vacuum valve connecting the chamber, so that the trap is not exposed to air when the chamber is opened and the pumping system is fully operational. In that system the pump, which was used, was an Edwards diffusion pump, 1400 ls^{-1} 8 inch with a pumping speed in the area of the high vacuum valve ~360 ls^{-1}. The pump is connected to the chamber with a tube with a diameter of 150 mm and a length of 200 mm. At the inlet of the chamber, when the high vacuum valve is open, the pump has a pumping speed of 110 ls^{-1} and the pressure for a stainless steel chamber reaches between 10^{-6} and 10^{-7} mTorr.

2.4.3.2 The Rotary Pump

The rotary pump has two basic functions. One function is the initial pumping of the chamber to the point where the diffusion pump can be started to create the high vacuum. The second function is to maintain the pressure at the outlet of the pump (diffusion) at low price throughout the operation of the diffusion pump. The rotary pump must be suitable to maintain the pressure at the outlet of the diffusion pump below a specific value. If it is not then the first jet of the diffusion pump will stop working and large amounts of oil vapor will diffuse into the chamber. The first jet stops working if the pressure at the diffusion inlet is higher than 10^{-3} mTorr.

The diffusion pump of 6 inch has a pumping speed about 1400 ls^{-1} at the inlet. Thus the maximum gas load, that the pump can handle, is 1.3 mTorr ls^{-1}. All gases that will enter the diffusion, after passing to the tubes will be pumped by the rotary pump. The critical value for the 6inch diffusion pump is approximately 0.5 mTorr. However, to be sure of the results, the pressure should not exceed 0.2 mTorr. Thus, at the outlet of the diffusion pump a pumping speed of 1.3 mTorr ls^{-1}/0.21 s^{-1} is required, that is to say 6.5 ls^{-1}.

Fig. 2.5: The Rotary Pump

The rotary pump is connected to the diffusion pump via a 25mm diameter tube in which the gases have a pumping speed of 25 ls^{-1}. Finally, the pumping speed S_p, that the rotary pump must have, can be calculated using the equation that gives the series connection of elements: $1/S_p = 1/S_1 + 1/S_2$ Where $S_2 = 6.5ls^{-1}$ is the pumping speed, which is required at the outlet of the

diffusion pump, $S_1 = 25ls^{-1}$ is the pumping speed through the tube and Sp is the pumping speed which is required by the rotary pump.
So, $1/S_p = 1/S_2 - 1/S_1 = 1/6.5 - 1/25 = 530\ l\ min^{-1}$

2.4.3.3 Pressure measuring instruments

One of the most important points in the whole operation of sputtering is the monitoring of the pressures prevailing in every part of the system at any given time, because the pressure affects the properties of the film. There are thermocouple manometers that measure pressures in the range of $1\text{-}10^{-3}$ mTorr. The Penning manometer is used for pressures in the range 10^{-3} to 10^{-7} mTorr. During deposition the pressure is measured by a Hastings CVT-15 manometer, the head of which is placed at the base of the chamber [37].

Chapter 3 – *Characterization of Thin Films*

3.1 Introduction

This chapter presents all the characterizations techniques which were used for determining the properties of films. The purpose of this chapter is to understand the basic principles of these specific characterizations techniques and the properties each one can give after monitoring the measurement and extracting and analyzing the data.

3.2 Surface Characterizations

3.2.1 Scanning Electron Microscopy (SEM)

A scanning electron microscopy (SEM) is a type of electron microscope which uses a focused electron beam to scan the surface of samples in order to produce images. The electron beam interacts with the atoms of the sample, producing various signals which contain information about the surface topography and the composition of the sample.

The electrons are produced at the top of the column by the electron source. They are emitted when their thermal energy overcomes the work function of the source material. Then they are accelerated down and passed through a combination of lenses and apertures to produce a focused electron beam that hits the surface of the sample. The sample is on a motorized stage in the chamber area and both the column and the chamber are in vacuum.

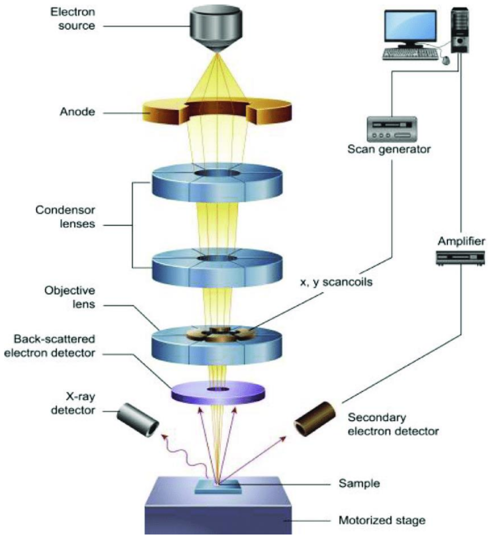

Fig. 3.1: Schematic form of SEM [38]

SEM produces images when a focused beam of high energy electrons scans the sample. When the electron beam hits the surface of sample, it penetrates the sample to a depth of a few microns and interacts with it. The depth of penetration depends on the accelerating voltage and the density of the sample. A lot of signals are produced by interaction of the electron beam and the sample. In SEM only secondary electrons and backscattered electrons are used for formation of the image.

The backscattered electrons are high energy electrons which originate from the electron beam. They are reflected or back-scattered out of the specimen interaction volume by elastic scattering interactions with atoms of specimen. The secondary electrons are low energy electrons (<50 eV) which are ejected from conduction or valence bands of the atoms of specimen by inelastic scattering interactions with beam electrons. Due to their low energy, the secondary electrons originate from within a few nanometers below the sample surface.

These signals are collected by one or more detectors and turn them into a picture. The SEM image is a 2D intensity map, that is each image pixel on the display corresponds to a point on the sample, which is proportional to the signal intensity captured by the detector at each specific point **[2][3]**.

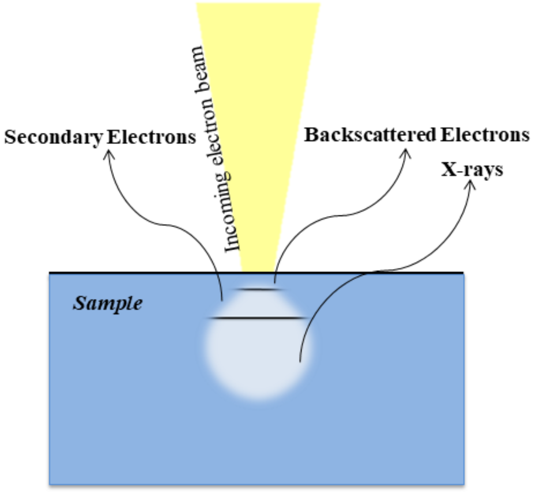

Fig. 3.2: Schematic of electron beam interaction with the sample in SEM

3.2.2 Atomic Force Microscopy (AFM)

The Atomic Force Microscope (AFM) is alternatively known as the Scanning Force Microscope (SFM). It is a high resolution non-optical technique and it is a powerful measurement tool for surface analysis in three-dimensional (3D) detail down to the nanometer scale. It allows accurate and non-destructive measurements of the topographical, electrical, magnetic, chemical, optical and mechanical properties of a sample surface with very high resolution in air, liquids or ultrahigh vacuum. AFM can measure conductive, semiconductor and insulating surfaces [41][42].

The AFM mainly consists of a sharp tip, a cantilever, piezoelectric element, a laser and a detector of deflection of the cantilever. The sharp tip is located on one end of the cantilever. The piezoelectric element moves the sample on x, y and z axes under the tip which scans over surface. As the cantilever deflects, a laser beam is reflected from the back of the cantilever and the signal of deflection is detected by a split photodiode, as a result an image of measured sample can be created [40].

The measurements of this technique are based on the local attractive or repulsive force between the tip and sample. These forces are electrostatic, magnetic, Van der Walls or others, depending on the properties of the measured material and the mode of scanning, which has been selected. These forces cause a deflection of the cantilever towards or away from the sample as the tip scan over surface [43].

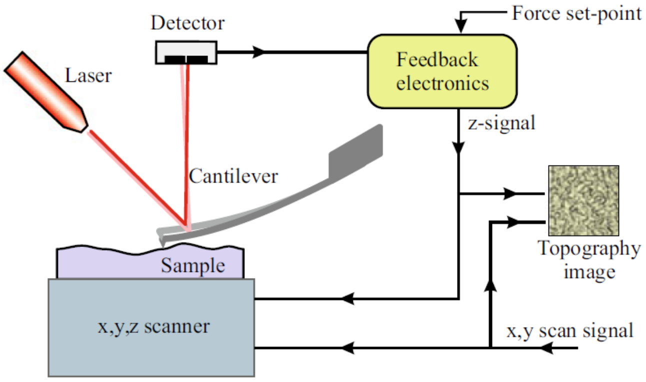

Fig. 3.3: Schematic of atomic force microscopy operation [43]

3.3 Chemical Characterizations

3.3.1 Energy Dispersive X-ray (EDX)

Energy Dispersive X-ray spectroscopy (EDS, EDX, EDXS or EDAX) is an analytical technique which is used for analytical or chemical characterization of materials. This system is generally attached to an electron microscopy instrument such as transmission electron microscopy (TEM) or scanning electron microscopy (SEM). It uses a beam of high energy electrons and its function is based on the emission of a specimen characteristic X-rays.

In particular, in the sample when the atoms are at rest they contain unexcited electrons in discrete energy levels. When the beam penetrates the sample then it may excite an electron in an inner shell, ejecting it from the shell while creating a hole where the electron was. An electron from a higher binding energy shell falls into the hole and the difference in energy between the higher and the lower energy shells may be released in the form of an X-ray [44]. The released energy is on the order of keV.

EDX analysis gives a spectrum that displays peaks which are correlated to the elemental composition of the investigated sample. Especially, the energy levels of the emitted x-rays correlate to individual elements, while the proportional counts relates to the quantity of the element [40].

3.3.2 X-ray Photoelectron Spectroscopy (XPS)

X-ray Photoelectron Spectroscopy (XPS) is also referred as Electron Spectroscopy for Chemical Analysis (ESCA). It is a surface characterization technique, which can analyze samples to a depth of about 5 nm. Also, it can analyze a broad range of samples, for example solids, gases and liquids. This technique uses the measurement of kinetic energy of photoelectrons to determine the binding energy and reveal the chemical elements, which are present at the surface of test sample as the chemical bond that exists between these elements.

XPS technique needs ultrahigh vacuum conditions (~10^{-7} mTorr) and the source of radiation is a high energy X-rays (1000-1500 eV), so it can eject electrons from the core and atomic orbitals. It uses an electron energy analyzer to measure the energy of the emitted electrons (photoelectrons). The elemental identity, chemical state, and quantity of a detected element can be determined from the binding energy and intensity of a photoelectron peak. Because of detection of electrons rather than photons to examine the electronic structures of a sample it differs from the conventional methods of spectroscopy.

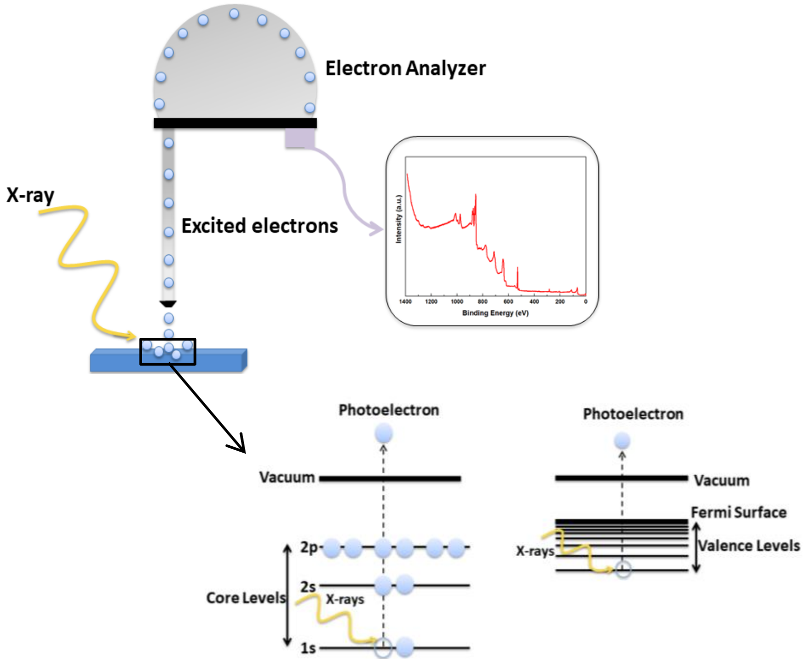

Fig. 3.4: Schematic form of XPS

The principles of photoelectron spectroscopy are based on the photoelectric effect. When an electromagnetic radiation bombards a sample, some electrons become excited enough to escape from the atom. The ejected electrons are called photoelectrons. The photoelectric effect is described from the following equations:

$$\mathrm{hv} + \mathrm{E_i} = \mathrm{E_f} + \mathrm{E_k}$$

$$\Rightarrow \mathrm{E_k} = \mathrm{hv} - (\mathrm{E_f} - \mathrm{E_i})$$

$$\Rightarrow \boxed{\mathrm{E_k} = \mathrm{hv} - \mathrm{E_I}} \quad (3.1)$$

Where hv is the energy of X-ray photon, E_i the initial energy of the target atom, E_f is the final energy of the ionized atom, E_k is the kinetic energy of photoelectron and E_I is the ionization energy of electron, that is, the binding energy of electron. The binding energy provides detailed quantitative information about electronic structure of molecules. Ionization is defined by transitions from the ground state of a neutral molecule to the ion states [45][46][47].

3.4 Structural Characterizations

3.4.1 X-Ray Diffraction (XRD)

The X-ray diffraction (XRD) is a nondestructive technique for the characterization of materials' structure, mainly at the atomic or molecular level. It functions best for crystalline or partially crystalline materials but it is also used to study for non-crystalline materials. It provides information on structures, preferred crystal orientations, phases, and other structural parameters, like average grain size, strain, crystal defects and crystallinity.

An x-ray diffractometer consists of three basic parts: an X-ray tube, a sample holder and an X-ray detector. Electrons are produced by heating a filament, then they are accelerated by applying a voltage and they bombard a metal target (Cu). When electrons have sufficient energy, they eject inner shell electrons of the target creating holes. An electron from a higher binding energy shell falls into the hole and the difference in energy between the higher and the lower energy shells may be released in the form of an X-ray. The produced x-rays passed through a diaphragm and focus slit and they are directed to the measured sample.

The beam of x-rays is parallel, monochromatic, and coherent. Its wavelength (λ=1.5405nm) is similar to the spacing between atoms in crystalline materials. In this way, the crystals act as diffraction barriers for x-rays. The x-rays pass through the sample, scatter from the atoms of material at points O, P and R, as seen in figure 3.5, changing the direction of the beam at different angle (theta). This is the angle of diffraction. Constructive interference of scattered beams occurs when the path length difference between two beams is equal to a whole number, n, of wavelengths. That is, the condition for diffraction is:

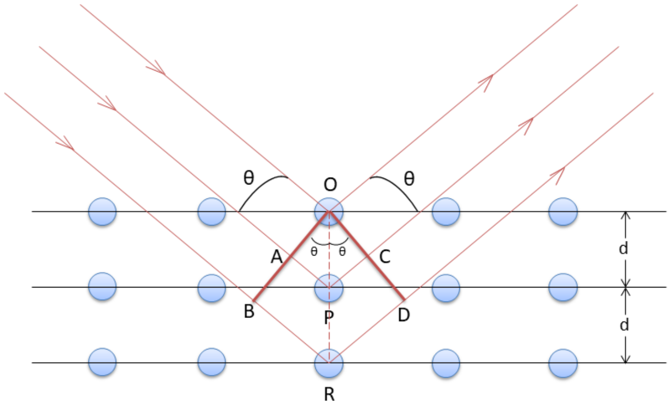

Fig. 3.5: Diffraction of x-rays from a crystal

$$n\lambda = BR + RD$$

$$\Rightarrow n\lambda = d\sin\theta + d\sin\theta$$

$$\Rightarrow \boxed{n\lambda = 2d\sin\theta} \qquad (3.2)$$

Equation 3.2 is known as Bragg's law. Also, n is the order of reflection and it may be any integer (1, 2, 3,…). If Bragg's law is not satisfied, then the interference will be destructive so as to yield a very low-intensity diffracted beam. From equation 3.2 the interplanar space can be calculated as wavelength (λ), the order of reflection (n) and the angle of diffraction (θ) are already known.

The distance between two adjacent and parallel planes of atoms (d_{hlk}) is a function of the Miller indices (h, k, and l). For crystal structures that have cubic symmetry the relation between distance of parallel planes and Miller indices is:

$$\boxed{d_{hkl} = \frac{\alpha}{\sqrt{h^2+k^2+l^2}}} \qquad (3.3)$$

In which α is the lattice parameter. From equation 3.3, the lattice parameter can be calculated as anything else is known [48].

Peak broadening may be observed in graphs. It is due to two factors, instrumental broadening and the broadening caused by specimen. The instrumental broadening was eliminated by using a diffraction pattern. The peak broadening from specimen is due to crystallite size (grain size) and lattice strain. Crystallite size (D) is the mean size of crystalline and it can be calculated by Scherer's law which can be written as:

$$\boxed{D = \frac{k \cdot \lambda}{\beta \cos\theta}} \quad (3.4)$$

Where θ: Bragg angle

λ : X-ray wavelength

k: A dimensionless shape factor and is equal to 0.89 for integral breadth of spherical crystals with cubic symmetry.

β: Full Width Half of the Maximum intensity (FWHM).

Crystal imperfection and distortion create lattice strain. The lattice strain induces not only peak broadening but also shifts the position of peaks. It can be determined using Wilson formula which is [49][50]:

$$\boxed{\varepsilon = \frac{\beta \cot\theta}{4}} \quad (3.5)$$

In addition, dislocation density can be calculated by XRD measurements. It is a measure which shows the number of dislocations in a unit volume of a crystalline material. It can be calculated by equation[51]:

$$\boxed{\delta = \frac{1}{D^2}} \quad (3.6)$$

Where D: crystallite size

3.5 Optical Characterization

The optical measurements are based on the interaction of electromagnetic radiation with the sample. In these measurements a beam of light is used, which hits and penetrates the sample. The transmittance and reflectance can be measured and optical absorption coefficient (α) and energy gap (E_g) can be calculated.

The electromagnetic radiation, which is used, is from ultraviolet to infrared wavelengths. When a beam of light hits the sample, a percentage of light will be reflected, a percentage will be absorbed and a percentage will penetrate the sample. Suppose a sample consists of two layers, the first is the film having thickness d and absorption coefficient α, and the second is substrate (glass). Also there is air before film and after substrate. As seen in figure 3.6 the initial intensity of light is I_o. When it hits film, the radiation which will penetrate and arrive the next layer is $I_T=T_{af}e^{-\alpha d}I_o$, while the radiation, which will be reflected is $I_R=R_{af}I_o$. The term T_{af} is the percentage of transmittance, which passes through air-film interface, and R_{af} is the percentage of reflectance which is reflected back at the air-film interface. Moreover, when the beam is passed through a film, there is absorption. The absorption is indicated by the term $e^{-\alpha d}$, where α is absorption coefficient and d is the thickness of layer.

If the following assumptions apply, then the total transmittance and reflectance of incident radiation, which are measured, is given by the following equations. 1) The layer of substrate does not have absorption ($a_s=0$). 2) The incident radiation on the surface is vertical. 3) The film is thin enough that the optical path of light within the film is the same before and after reflection at the film-glass interface. 4) The reflectance of radiation from layer 1 to layer 2 is the same as the reflectance from layer 2 to layer 1 ($R_{12}=R_{21}$). 5) The reflectance of radiation from glass to air is equal to zero ($R_{ga}=0$). 6) The transmittance at two interfaces of film is equal ($R_{af} = R_{fg}$).

$$\boxed{T_T = \frac{(1-R_{af})^2 e^{-ad}}{1-R_{af}^2 e^{-2ad}} \quad \text{and} \quad R_T = \left[\frac{R_{af} + R_{fg}(1-2R_{af})e^{-\alpha d}}{1- R_{fg}R_{fa}e^{-\alpha d}}\right]} \qquad (3.7)$$

Where R_{af} is the reflectance from air to film, R_{fg} is the reflectance from film to glass, R_{fa} is the reflectance from film to air, a is the absorption coefficient and d is the thickness of film.

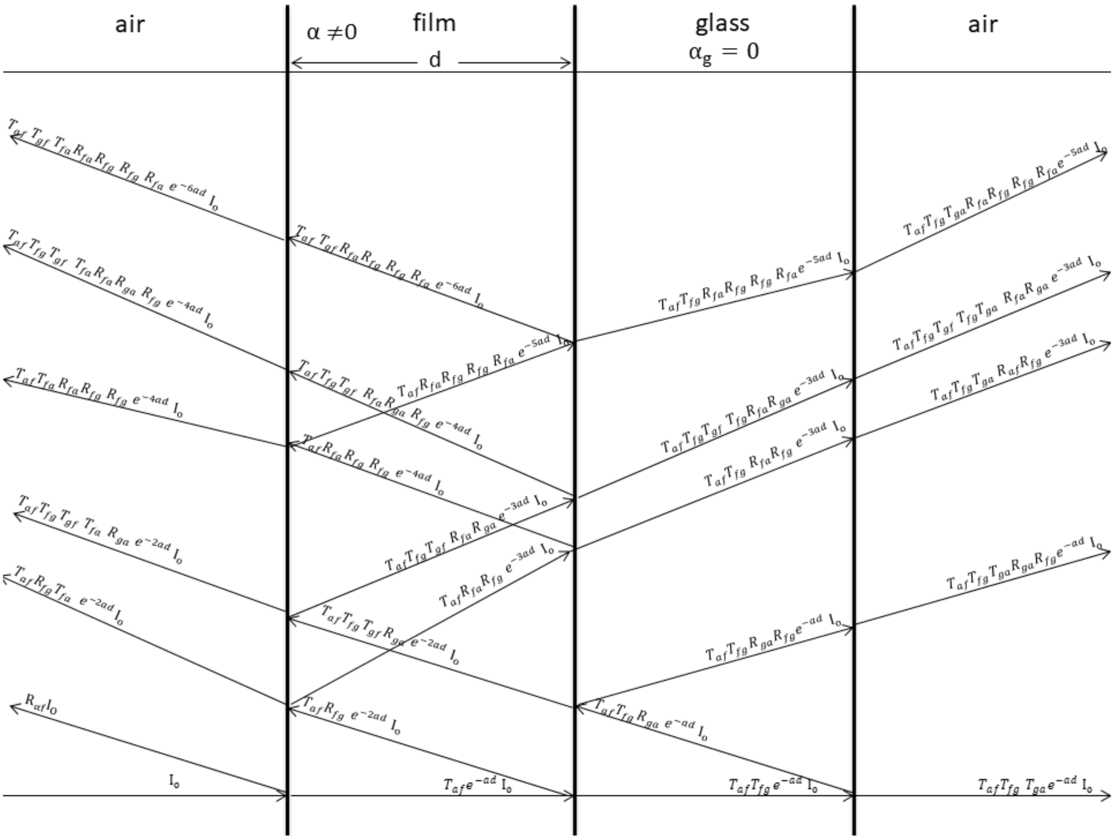

Fig. 3.6: Schematic of light's path

From the equation of transmittance, the relation of absorption coefficient (cm^{-1}) can be calculated and it is equal to:

$$\boxed{\alpha = \frac{1}{d}\ln\left(\frac{(1-R)^2+\sqrt{(1-R)^4+4R^2T^2}}{2T}\right)} \qquad (3.8)$$

Where R is the measured total reflectance, T is the measured total transmittance and d is the thickness of the sample. The absorption coefficient describes the percentage of light which is absorbed by a given thickness. The proof of absorption coefficient is presented in Appendix 1. From the calculation of absorption coefficient, the energy gap (E_g) of semiconductor can be calculated as follows.

The transitions in semiconductors can be two types, the direct and indirect transitions as seen in figure 3.7. The direct transitions include one photon, while the indirect transitions include an additional particle, except the photon, which is phonon. In direct transitions a photon, which has energy equal or greater than energy gap, is absorbed and an electron is excited from the valence band to the conduction band. In indirect transitions, a photon cannot excite an electron directly because the electron must pass through an intermediate state to the conduction band. The intermediate state is phonon, which helps to electron to change momentum and go to conduction band. The energy gap for direct and indirect transitions can be calculated by relation:

$$\boxed{\alpha h v = A\left(h v - E_g\right)^n} \quad (3.9)$$

Where α is the absorption coefficient, hv is the energy of photon, A is a constant, Eg is the energy gap and n is a constant which is equal to 2 for indirect transitions and ½ for direct transitions. For direct band gap semiconductors, plotting $(ahv)^2$ against hv the direct optical band gap E_g is determined from the extrapolated intercept. While for indirect band gap semiconductors the optical band gap E_g is determined, plotting $(ahv)^{1/2}$ against hv.

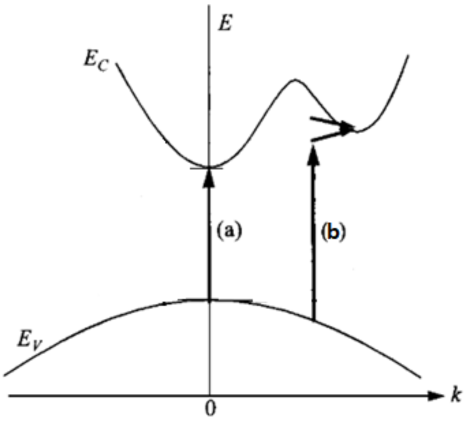

Fig. 3.7: Optical transitions: (a) allowed and (b) indirect transition involving phonon

3.6 Electrical Characterizations

3.6.1 Van der Pauw Method

The resistivity of a sample/semiconductor is one of the most important measurements for characterization of samples. To be calculated the resistivity, initially two or four point resistance measurements are made on sample and then resistance is converted into resistivity by means of some geometrical factor. These geometrical factors depend on the shape and size of the sample as well as the position of contacts.

The Van der Pauw method is a 4-point measurement which determines the resistivity and the Hall coefficient of samples. In that kind of measurements, the sample must be flat, its thickness must be homogenous and small in relation to the distance between the contacts. Also the four contacts must be on the edge of the sample and they must be small in relation to the area of the sample.

In sheet resistance measurements, a current is applied and a voltage is measured. These measurements are made with help four probes, which are placed in this way that they fit perfectly on the contacts. The voltages for the respective currents are symbolized in the following way:

$$\boxed{R_{ij,kl} = \frac{V_{kl}}{I_{ij}} = \frac{V_k - V_l}{I_{ij}}} \quad (3.10)$$

The current flows from contact i to contact j and the voltage is measured between the k and l contacts.

All possible combinations for voltage measurement are:

$V_1 = V_{+12,43}$ $V_2 = V_{-12,43}$ $V_3 = V_{+23,14}$ $V_4 = V_{-23,14}$

$V_5 = V_{+43,12}$ $V_6 = V_{-43,12}$ $V_7 = V_{+14,23}$ $V_8 = V_{-14,23}$

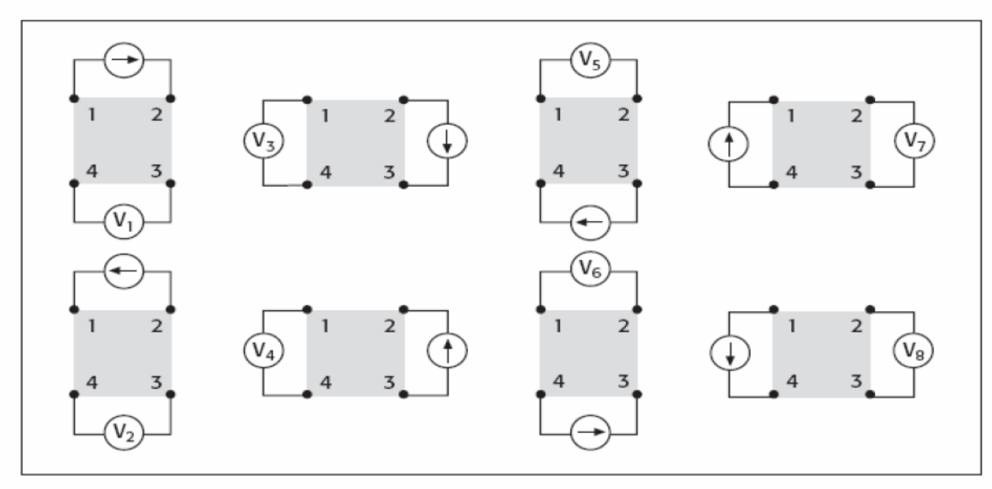

Fig. 3.8: All possible combinations for voltage measurement

As shown in figure 3.8, the current flows from point 1 to point 2 and the voltage is measured between points 4 and 3 ($V_{+12,43} = V_1$). By inverting the direction of the current, the voltage between points 4 and 3 is measured ($V_{-12,43} = V_2$). These measurements are repeated for all possible combinations that can be performed along the circumference of the sample following always a circular direction. After measuring all the voltages (8 in total), two values for the sheet resistance are calculated [52].

$$\boxed{R_A = \frac{\pi}{\ln 2} f_A \frac{(V_{+12,34} - V_{-12,34} + V_{+23,14} - V_{-23,14})}{4I}} \quad (3.11)$$

$$\boxed{R_B = \frac{\pi}{\ln 2} f_B \frac{(V_{+43,12} - V_{-43,12} + V_{+14,23} - V_{-14,23})}{4I}} \quad (3.12)$$

Where R_A and R_B are two values of sheet resistance (Ohm/square), I is the current, f_A and f_B are correction factors and π/ln2 is as known as the van der Pauw constant.

The symmetry factors (Q_A and Q_B) are calculated by measured voltages using the below equations:

$$\boxed{Q_A = \left(\frac{V_{+12,43} - V_{-12,43}}{V_{+23,14} - V_{-23,14}}\right)} \quad \text{and} \quad \boxed{Q_B = \left(\frac{V_{+43,12} - V_{-43,12}}{V_{+14,23} - V_{-14,23}}\right)} \quad (3.13)$$

The symmetry factors (Q_A and Q_B) are related to the geometric correction factors (f_A and f_B) , which are equal to 1 if the sample is perfect symmetry, with the relation:

$$\boxed{\frac{Q-1}{Q+1} = \frac{f}{0.693} \arccos\left(\frac{e^{0.63/f}}{2}\right)} \quad (3.14)$$

The graph of this relation is given in fig. 3.9:

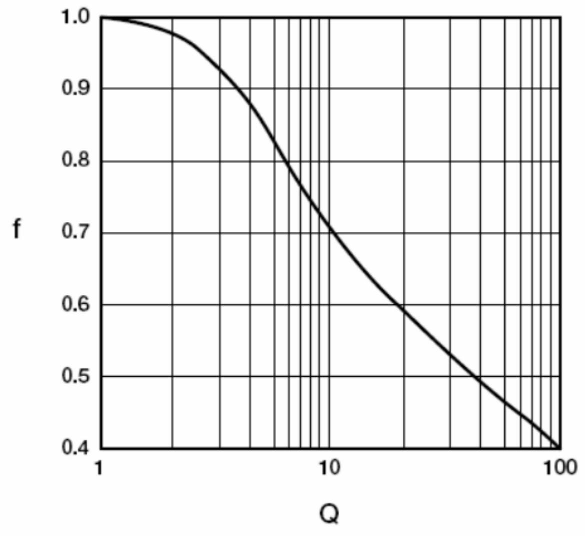

Fig 3.9: Graph f vs Q

So, if the value of Q has been calculated by measured voltages, then the respective value of f can be found from this graph. Finally, the total value of sheet resistance is calculated according to Van der Pauw theory from the relation [53]:

$$\boxed{\exp\left(\frac{-\pi R_A}{R_{sh}}\right) + \exp\left(\frac{-\pi R_B}{R_{sh}}\right) = 1} \quad (3.15)$$

The sheet resistance (R_{sh}) is given from the equation:

$$\boxed{R = \rho \frac{l}{S} = \rho \frac{l}{wd}} \quad (3.16)$$

If l = w then:

$$\boxed{R_{sh} = \frac{\rho}{d}} \quad (3.17)$$

Where l is the length, w is the width and d is the thickness of the sample. The sheet resistance helps to the calculation of resistivity (Ohm·cm), which is the main determination for the conductivity of a sample [53][54][55].

$$\boxed{\sigma = \frac{1}{\rho}} \quad (3.18)$$

3.6.2 Hall Measurements

Hall measurements are very important in the characterization of samples/semiconductors because the mobility, the concentration of carriers as well as the type of conduction carriers (electrons or holes) and the type of semiconductors (n- or p-type) can be calculated. Hall Effect is based on the principle that when current flows in one direction in a conductor or semiconductor, and a magnetic field is introduced perpendicular to this direction, then a voltage can be measured at right angles to the current path.

Current is the movement of charged particles (electrons or holes) through a path. If a current is supplied to a conductor or semiconductor, current will start to flow in it. So, the charge carriers will flow from one end to the other end of sample. As the charge carriers are flowing, they produce magnetic field. When the sample is placed in a magnetic field, then this magnetic field will distort the magnetic field of the charge carriers. As a result, the flow of charge carriers will be disturbed. The force, which disturbs the flow of charge carriers, is known as Lorentz force. Due to this phenomenon, the electrons will be deflected to one side of the sample and the holes to other side of the samples. For this reason a potential difference, which is known as Hall Voltage, will generate between both sides of the sample in a direction perpendicular to current and magnetic field. This voltage can be measured and this effect is known as Hall Effect [56].

In Hall measurements, fig. 3.10, a positive magnetic field B_p is applied to the sample and current flows between points 1 and 3. Then the voltage between points 2 and 4 ($V_{13,24\,P}$) can be measured. Afterward the current is reversed and the voltage between points 4 and 2 can be measured ($V_{31,42\,P}$). The above procedure is repeated for the other pair of antidiameter points. That is to say current flows between points 2 and 4, and the voltage between points 1 and 3 ($V_{42,13\,P}$) can be measured and vice versa $V_{24,31\,P}$. Finally, the direction of the magnetic field is reversed and the same measurements are repeated. So from the measured 8 voltages, the following Hall voltage pair can be calculated.

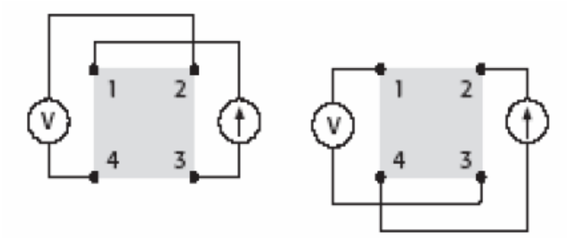

Fig 3.10: Combinations of Hall voltage

$$\boxed{\begin{gathered} V_{HC} = V_{13,24\,P} - V_{13,42\,N} + V_{13,42\,P} - V_{31,24\,N} \\ \text{and} \\ V_{HD} = V_{42,13\,P} - V_{24,13\,N} + V_{24,31\,P} - V_{42,31\,N} \end{gathered}} \qquad (3.19)$$

If the sum of V_{HC} and V_{HD} is positive then the sample is p-type semiconductor, otherwise the sample is n-type semiconductor.

The Hall coefficient is the ratio of the induced electric field to the product of the current density and the applied magnetic field. It is a characteristic of the material from which the semiconductor is made. Its value depends on the type, number, and properties of the charge carriers constituting the current. The Hall coefficient (cm^3/C) is calculated by:

$$\boxed{R_H = \frac{E}{BI}} \qquad (3.20)$$

where B is the applied magnetic field, E is the induced electric field and I is the current density. In the system, in which the measurements were made, the value of the magnetic field is 0.32 Tesla, but the calculation of the Hall coefficient requires the magnetic field to be in units $V \cdot s/cm^2 = 10^8$ Gauss. The electric field is equal to: $E = V \cdot d$. So the Hall coefficients (cm^3/C) for the pair of Hall voltages are:

$$\boxed{R_{HC} = d\,\frac{V_{HC}}{BI}} \quad \text{and} \quad \boxed{R_{HD} = d\,\frac{V_{HC}}{BI}} \qquad (3.21)$$

The total Hall coefficient is equal to the mean of R_{HC} and R_{HD}.

$$\boxed{R_H = \frac{R_{HC} + R_{HD}}{2}} \quad (3.22)$$

In addition, the density of carriers (cm^{-3}) is given by the relation:

$$\boxed{N_D = \frac{1}{qR_H}} \quad (3.23)$$

While the mobility ($cm^2/V\cdot sec$) is given by [57]:

$$\boxed{\mu = \frac{R_H}{\rho}} \quad (3.24)$$

In this way, sheet resistance, resistivity, conductivity, doping type, sheet carrier density and mobility of majority carriers can be calculated [55].

3.6.3 Seebeck Effect

The Seebeck effect is a phenomenon which is appeared when a temperature difference (ΔT) is applied between two dissimilar electrical conductors or semiconductors. From this temperature difference, a voltage difference is produced between these substances.

When one of the two conductors or semiconductors is heated, then valence electrons from the warm region of the material have more energy (thermal energy), and therefore higher velocities, compared to those in the cold region. So, they will diffuse from the hot to the cold region. Electrons prefer to go there, where the energy is lower. For this reason they move from warmer to the colder place which leads to the transporting energy, and thus equilibrating temperature eventually. As a result, in the cold region accumulation of electrons will be existed and in the hot region naked positive ions will be created.

This process results in the creation of a potential (Seebeck voltage), which will eventually take a value capable of preventing any further electron displacement. If this pair is connected through an electrical circuit then direct current (DC) will flow the circuit. The Seebeck voltage is small, usually is a few microvolts per kelvin of temperature difference at the junction. Some devices, if the temperature difference is large enough, can produce a few millivolts. The open circuit potential difference in the circuit for temperatures T_h and T_c ($T_c<T_h$) is given by:

$$\boxed{\Delta V = -\alpha(T_h - T_c)} \quad (3.25)$$

where α is known as thermionic power or the Seebeck coefficient (V/k). The Seebeck coefficient describes the magnitude of this effect. Its value depends on the type of majority carriers (holes or electrons). If the sample is p-type semiconductor, then the value of α is positive. Otherwise the value of α is negative for n-type semiconductor [58].

Chapter 4
Theory & Characterization of *pn Junction*

4.1 Introduction

The following chapter is an introduction to the theory of p-n heterojuctions and the theory of solar cells, with purpose to understand the basic principles of diodes.

4.2 p-n heterojunctions

The pn junctions are two terminal devices and they are very important in modern electronic applications and in understanding other semiconductor devices. It depends on the doping profile, device geometry and biasing condition. The basic theory of current-voltage characteristics of the pn junctions was established by Shockley but this theory was extended by Sah, Noyce, Anderson and Moll.

A p-n heterojunction is a junction which is formed between two dissimilar semiconductors. When the heterojunctions consist of two semiconductors with the same conductivity, the junction is called isotype heterojunctions (n-n or p-p junctions). When the heterojunctions consist of two semiconductors with the different conductivity, the junction is called anisotype heterojunctions (p-n heterojunctions).

In a p-n junction, the p-type semiconductor is on one side, and the n-type semiconductor is on the other side. In this brief theory the two semiconductors are assumed that they have different energy gaps (E_g), different work functions (ϕ_m) and different electron affinities (χ). The work function is defined as the energy required removing an electron from the Fermi level (E_F) to a position just outside the material (vacuum level). While the electron affinity is defined as the energy required removing an electron from the bottom of the conduction band (E_c) to a position just outside the material (vacuum level).

The following figure presents the energy band diagrams for two different p-n heterojunctions in equilibrium. In figure 4.1a the semiconductors are isolated and the n-type semiconductor has the smaller bandgap, while in figure 4.1b presents when they are into contact. Also In figure 4.1c the semiconductors are isolated and the p-type semiconductor has the smaller bandgap, while in figure 4.1c presents when they are into contact.

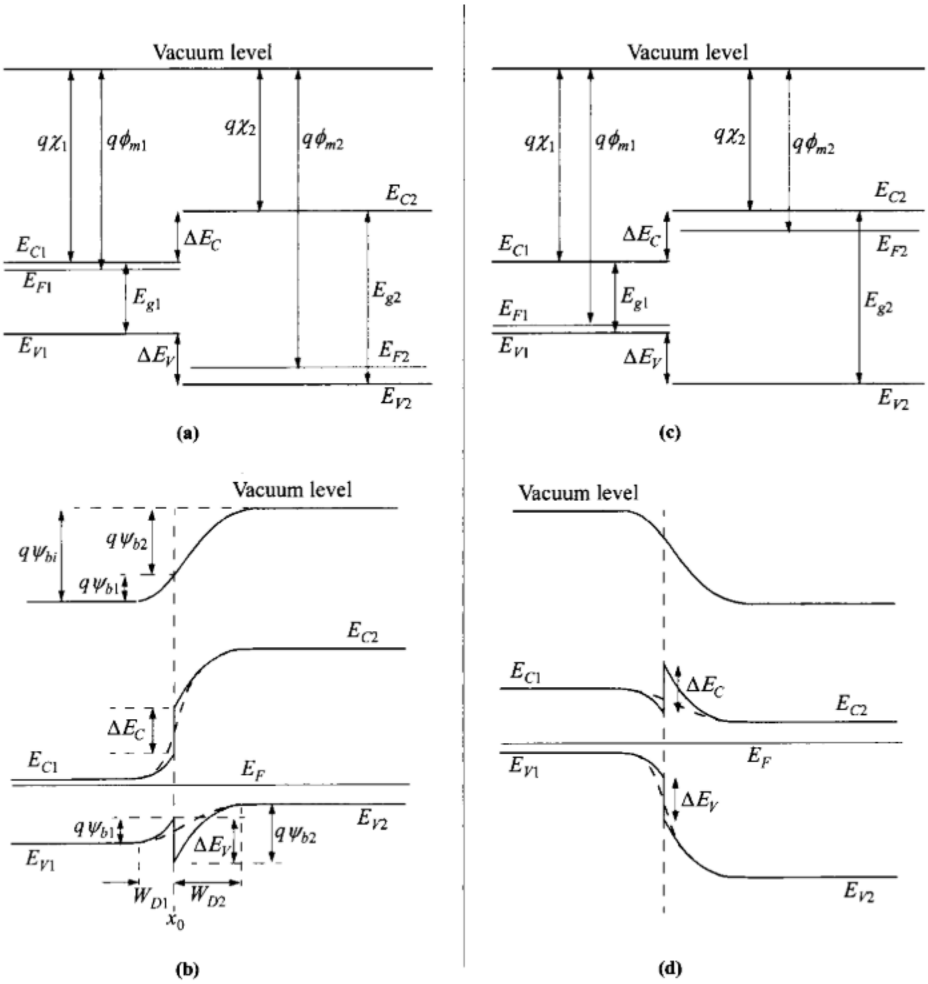

Fig. 4.1: Energy-band diagrams [59]

The difference in energy of the conduction-band edges in the two semiconductors is represented by ΔE_C, and that in the valence-band edges by ΔE_V. The Fermi level must coincide on both sides in equilibrium and the vacuum level is everywhere parallel to the band edges and continuous. The discontinuity in the conduction-band edges (ΔE_c) and valence-band edges (ΔE_V) does not change with doping in these cases where Eg and χ are not functions of doping (i.e., nondegenerate semiconductors). The total built-in potential ψ_{bi} is equal to the sum of the partial built-in voltages (ψ_{b1} + ψ_{b2}), where ψ_{b1} and ψ_{b2} are the electrostatic potentials supported at equilibrium by semiconductors 1 and 2, respectively. From the figure 4.1, it is apparent that since at equilibrium, $E_{F1} = E_{F2}$, the total built-in potential is given by [59][52]:

$$\boxed{\psi_{bi} = |\varphi_{m1} - \varphi_{m2}|} \quad (4.1)$$

4.3 Dark I-V

If a time-independent external electrical voltage U is applied to a p-n junction then the thermal equilibrium is destroyed. This situation in the p-n junction can be described as a stationary state in the vicinity of thermal equilibrium. There are two different ways to apply voltage to the diode, forward and reverse.

In the forward bias, the p-type semiconductor is attached to the positive terminal and the n-type semiconductor is attached to the negative terminal of the source as seen in fig 4.2a. In this situation, an electric field with the opposite direction to that in the depletion region is applied across the device, as a result the electric field at the junction is reduced. When the electric field reduces, the equilibrium of junction disturbs, the barrier reduces and the diffusion of carriers from one side of the junction to the other increases. While the diffusion current increases, the drift current remains essentially unchanged since it depends on the number of carriers generated within a diffusion length of the depletion region or in the depletion region itself. Since the depletion region is only reduced in width by a minor amount, the number of minority carriers swept across the junction is essentially unchanged.

On the other hand in the reverse bias, the p-type semiconductor is attached to the negative terminal, while the n-type semiconductor is attached to the positive terminal of the source, and as a result the electric field at the junction increases as seen in fig. 4.2b. The higher electric field in the depletion region decreases the probability which carriers can diffuse from one side of the junction to the other, hence the diffusion current decreases. As in forward bias, the drift current is limited by the number of minority carriers on either side of the p-n junction and is relatively unchanged by the increased electric field.

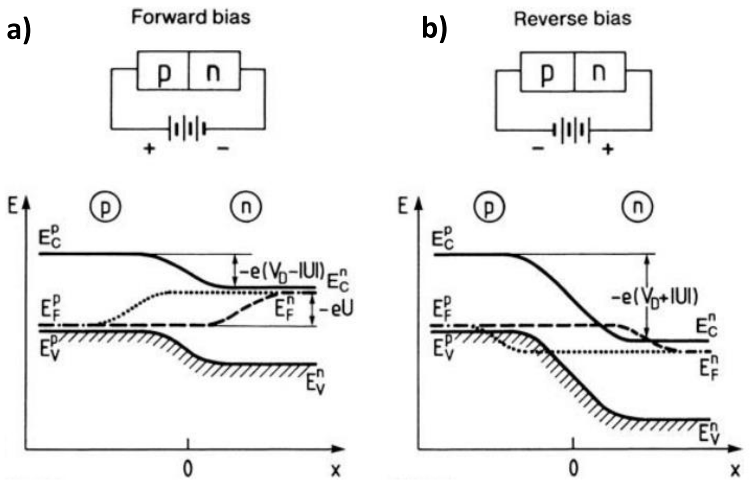

Fig. 4.2: Forward- and reverse-biased p-n junctions[52].

The circuit performance of a semiconductor device is mainly degraded by series and shunt resistance on the current flowing through the device, and on a number of other parameters. The series resistance (R_s) depends on the semiconductor resistivity, on the contact resistance, and sometimes on geometrical factors. The device must have negligibly small series resistance for a better performance.

The current of a pn junction is often written as a function of the diode voltage as:

$$\boxed{I = I_s\left[\exp\left(\frac{qV_d}{nkT}\right) - 1\right]} \qquad (4.2)$$

Where I_s is the saturation current and n the diode ideality factor [60].
The proofs of electrical measurements' analysis, which are used, are presented in Appendix 2.

4.4 Function of Solar Cells

A solar cell is a pn junction that converts the light energy into electrical energy. The conversion of energy consists of absorption of light energy (photon) producing electron-hole pairs in a semiconductor and charge carrier separation.

In a pn junction there are large carrier concentration gradients, which cause the diffusion of carriers. Holes diffuse from p-type semiconductor to n-type semiconductor and electrons diffuse from n-type semiconductor to p-type semiconductor. Because of this diffusion a layer without mobile charge carriers is formed. This space charge sets up an electric field which opposes the diffusion across the junction.

When the pn junction is illuminated by light, electron-hole pairs are generated by the photons, which have greater energy than the band gap. The number of electron-hole pair is proportional to the light intensity. In the depletion region there is electric field due to ionized impurity atoms, as a result the drift of electrons toward n-side and the drift of holes toward p-side. This charge separation results in the current flow from n-side to p-side when an external wire is short circuited. The electron–hole pairs generated within a distance of diffusion length from the edge of the depletion region contribute to the photo current because of the diffusion of excess carriers up to the space charge region as seen in fig. 4.3.

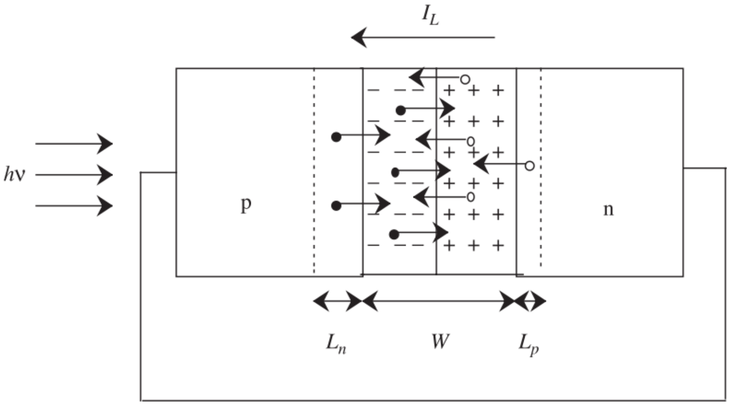

Fig. 4.3: A schematic form of carrier flow in illuminated p-n junction [61]

When the illuminated p–n junction is open-circuited, the voltage is generated due to the charge carrier separation. When the p- and n-side are short-circuited, the current is called short-circuit current (I_{sc}) and equals to the photogenerated current (I_{ph}), if the series resistance is zero. When the p- and the n-side are isolated, electrons move toward n-side and holes toward p-side, resulting in the generation of potential, as seen in fig. 4.4. The developed voltage is called open-circuit voltage (V_{oc}) [61].

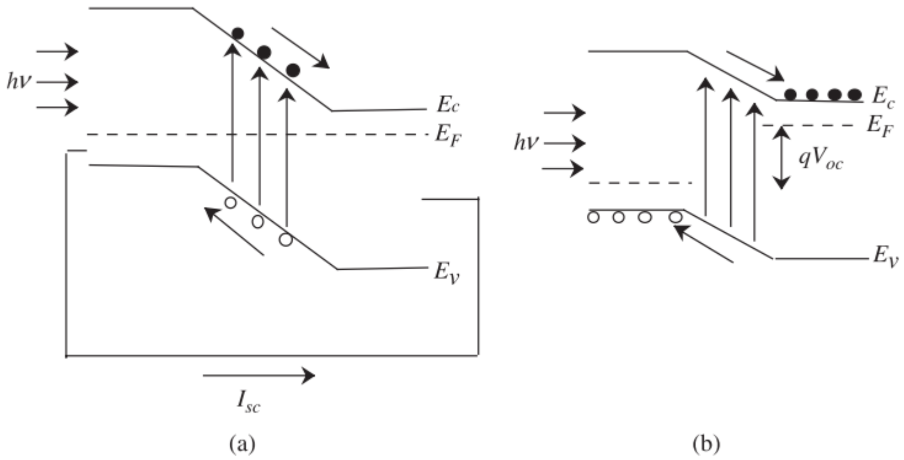

Fig 4.4: Energy band diagrams of illuminated p–n junction in (a) the short-circuited and (b) open-circuited current. [61]

The current-voltage characteristics of the p–n junction under illumination and dark are schematically shown in fig. 4.5

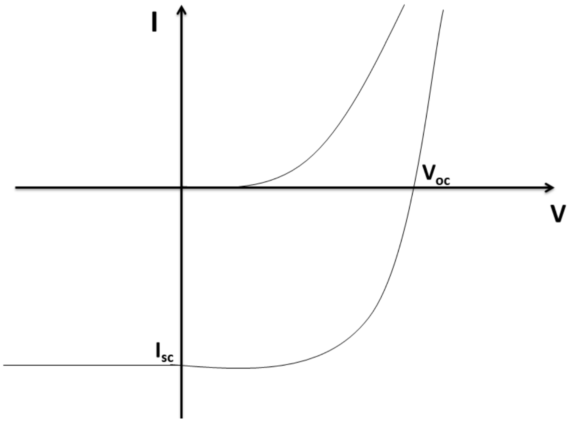

Fig. 4.5: Current vs voltage characteristics of p–n junction under illumination and darkness.

Chapter 5 – *Films & Diodes Preparation*

5.1 NiO Films Preparation

Undoped and doped NiO films (NiO, NiO:N, NiO:Nb & NiO:Nb-N) were fabricated by RF sputtering (Nordiko NS2500). The target of sputtering was a 6 in. diameter nickel (Ni) (purity 99.99%). Niobium (Nb) (purity 99.99%) pellets were placed on nickel target. They had 1 cm diameter and 2 mm thick. In plasma the gases, which were used during deposition, were Ar, O_2 and N_2 (purities: Ar 99.999%, O_2 99.95% and N_2 99.999%).

All films were deposited on unintentionally heated Si (100) wafer pieces and fused silica glass substrates. The substrates were mounted 10 cm above the sputtering target. The glass substrates were ultrasonically cleaned in acetone and isopropanol, rinsed with deionized water and dried in the flow of nitrogen gas. The Si substrates were dipped in 10% HF solution for 30 s to remove the native oxide from the surface before placing them into the sputtering chamber.

Before depositions, the target was pre-sputtered for at least 20 min in Ar plasma, at 5 mTorr and 300 W RF power to remove any contaminants from the target surface and to enable equilibrium conditions to be reached. During deposition the RF power was set at the desired power (300W or 400W) and the total pressure was kept at 5 mTorr. The percentage of gases in plasma was adjusted by the ratio of their flow rates through a set of mass flow controllers. The thicknesses of film were measured by a Veeco Dektak 150 profilometer.

For the characterization of films, as mentioned above, two different substrates were used, fused silica and silicon. On the fused silica substrate photolithographic mask was used which is seen in fig. 5.1. For the optical and structural (GIXRD) characterization of films the geometry (a) was used, for their electrical characterization the geometry (b) was used, and for Hall measurements the geometry (c) was used. In GIXRD measurements, the incidence angle of x-rays was 1.6^{o}. In Appendix 3 some measurements of GIXRD in different incidence angles are presented. For electrical characterizations Au ohmic contact was used on the points, which appear darker in fig. 5.1. The brown color in the fig. 5.1 shows the places where thin films are coated, while the black color shows the metallization with Au. The Si substrate was used for SEM, AFM and XPS measurements

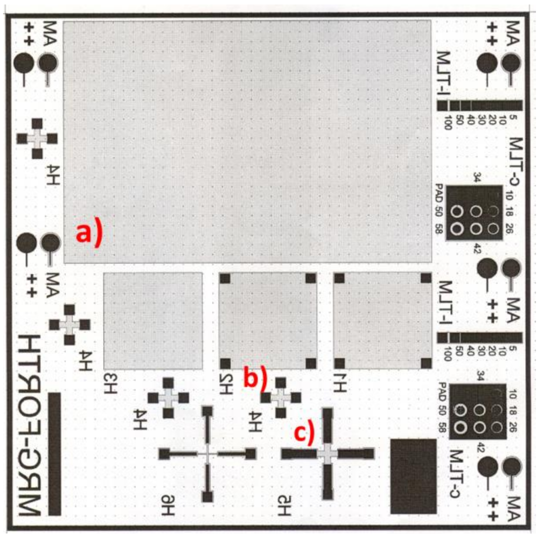

Fig 5.1: Photolithographic Mask

5.2 TiO_2 Films Preparation

Compact and mesoporous TiO_2 films were fabricated by spin coating following the standard procedure which is used when these layers are to be used as electron transfer layers for perovskite PVs. According to the perovskite solar cell technology, a thin compact TiO_2 layer is used so to eliminate the contact of the perovskite layer with the Sn_2O_3:F (FTO) layer of the FTO-covered glass, which is used as the substrate. Above this, the mesoporous TiO_2 is used to increase the effective area of the perovskite-TiO_2 interface.

More precisely, commercially available FTO-coated glass was used as substrate (FTO and glass were 600 nm and 2 mm thick, respectively) which was cleaned employing a standard procedure: sonicated for 10 min in deionized water solution followed by an extra sonication step in acetone and then in isopropanol for 10 min, rinsed with acetone and dried in N_2-gas flow. After the cleaning process and properly masking part of the FTO layer by vacuum tape mask, the TiO_2 containing solution was spin-coated (2000 rpm, 30 s) on the FTO substrates. The solution was 50 μL of HCl (37%), 2.3 mL of ethanol and 150 μL of titanium isopropoxide, which was stirred for several hours. In this way, a compact TiO_2 (c-TiO_2) film, having a thickness of around 60 nm, was formed, which was followed by thermal treatment at 500 ◦C for 15 min in ambient air.

After the annealing of the c-TiO_2 layer, the substrates were plasma treated in oxygen and then a commercially available TiO_2 mesoporous paste diluted in ethanol was spin-coated (6000 rpm, 30 s) on top of the c-TiO_2/FTO/glass substrate. The mesoporous TiO_2 (m-TiO_2) layer formed was around 200 nm thick, and was afterward annealed at 500 ◦C for 15 min in air. The formed m-TiO_2/c-TiO_2/FTO/glass substrates were used for depositing the NiO layers.

5.3 Fabrication of NiO/TiO_2 Heterojunction

After preparing the m-TiO_2/c-TiO_2 layers as described above, the m-TiO_2/c-TiO_2/FTO/glass substrates were placed in the sputtering chamber. When the base-pressure was better than 10^{-6} Torr, the deposition conditions for desirable NiO film were applied. When the sputtering of films finished, the samples were removed from the chamber. The device was completed by sputtering deposition of 150 nm thickness and 1 mm diameter Au as the ohmic contact on the NiO and FTO layers, using the appropriate shadow mask, which defined the junction area of the diode. A schematic representation of the fabricated NiO/TiO_2 heterodiodes can be seen in Figure 5.2. The diodes were characterized just after fabrication and after thermal treatment (TT) in a glass tube furnace (Elite Thermal Systems Ltd) at 300 ◦C for 15 min in flowing N_2.

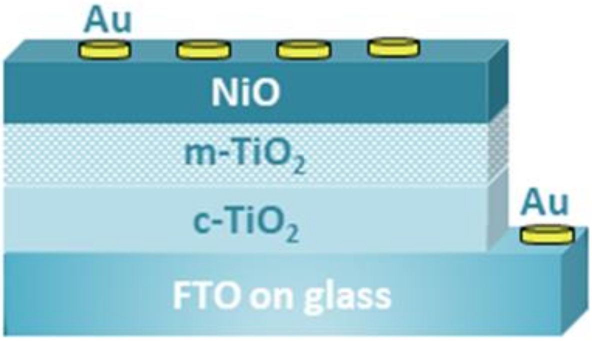

Fig 5.2: Schematic form of the fabricated NiO/TiO_2 heterodiode

5.4 Characterization of films & devices

In the following table experimental devices are presented, which were used for the characterization of films and heterojunction diodes.

Table 1: Experimental Devices and their characterization

Characterization of films		
Measurements	**Results**	**Instruments**
Scanning Electron Microscopy (SEM)	Surface morphology	Jeol JSM-7000 F
Atomic Force Microscopy (AFM)	Surface morphology-Roughness	Multimode Nanoscope IIA/Digital Instruments
Energy Dispersive X-ray (EDX)	Materials composition (at.%)	Oxford Instrument-INCA
X-ray Photoelectron Spectroscopy (XPS)	Materials composition-bonding	SPECS LAB
Grazing Incident X-Ray Diffraction (GIXRD)	Structural properties	Bruker D8
UV-Vis-NIR spectroscopy	T, a, Egap (Tauc plot)	Perkin Elmer Lambda 950
Seebeck measurements	Type of carriers	Home made
Hall effect	electrical properties (ρ, R_{sh}, $N_{A,D}$, type of conduction)	Biorad 2500
Characterization of devices		
Dark I-V	I_O, n, Φ_b, R_{sh} (Schottky & Cheung model)	Agilent 4200-SCS
UV Photo I-V	J_{SC}, V_{OC}	Laser HeCd, 325nm, 0.71W/cm^2

Chapter 6 – *Experimental Results*

6.1 Introduction

In this chapter the experimental results of films and diodes will be presented. Initially the characterization of undoped NiO will be presented and analyzed. Afterwards the characterization of doped NiO (NiO:N, NiO:Nb & NiO:Nb-N) will be showed and analyzed. Some experimental results of TiO_2 will be referred and finally the results of devices will be presented and explained.

6.2 Properties of undoped NiO

Undoped NiO films were made in different deposition conditions (gases in plasma and power) in order to observe the differences of their properties. As seen from the following table 1, three undoped NiO samples were made under different deposition conditions. The plasma gases for the X22 film were $Ar:O_2$ = 50:50 and power at 300 W. For the X23 film the same deposition conditions were used but the power was at 400 W. Moreover the plasma gases for the X24 film were $Ar:O_2$ = 95:5 and power at 300 W. The Argon atoms are heavier than the Oxygen atoms, as a result the deposition rate of X24 was increased from 1.59 nm/min to 2 nm/min. Moreover the more energetic plasma, power at 400W for film X23, resulted in films with higher deposition rate than the less energetic plasma, 300W for film X22.

Table 1: Details for deposition conditions of undoped NiO films

NiO	**Flow Rates Ratio (%)**		**Power (W)**	**Deposition Time (min)**	**Thickness (nm)**	**Deposition Rate (nm/min)**	**EDX**
	Ar	**O_2**					**O:Ni**
X22	50	50	300	126	200	1.59	1.36
X23	50	50	400	90	170	1.89	1.32
X24	95	5	300	100	200	2.00	1.26

6.2.1 Surface Characterization

As seen from the following SEM photos (fig. 6.1), the undoped NiO samples, which were made in the same plasma gases but different power, did not present differences on their surfaces and the grain size of both of them was almost the same. Consequentially the difference in power, from 300W to 400W, did not cause surface changes. The differences were observed in X24 sample, which was grown in plasma containing 95% Ar and 5% O_2. It had bigger grain size that may be due to the big rate of Ar.

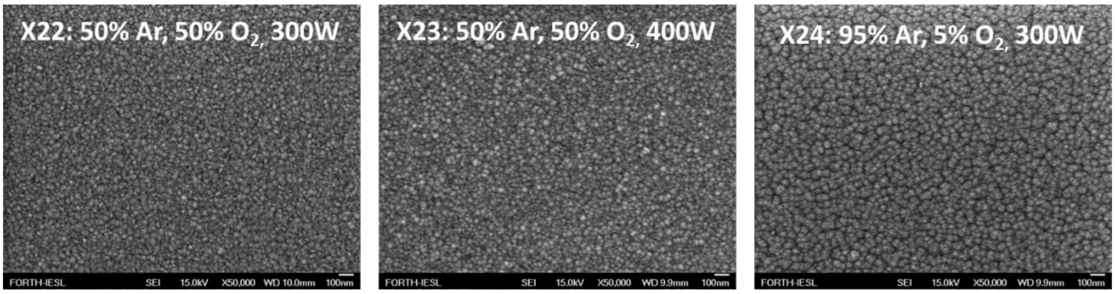

Fig 6.1: SEM photos of undoped NiO samples

Moreover from AFM measurements differences in roughness were observed on the surface of undoped NiO samples. The X24 sample had the biggest roughness because of the higher Ar amount and deposition rate. A difference in roughness between X22 and X23 samples also was observed because at different power used during deposition. The sputtered atoms obtain more kinetic energy when they arrive at the substrate surface because of extra higher kinetic energy provided by the high power. Hence, the atoms when arrive at the substrate, part of the kinetic energy might convert into thermal energy, and they had a higher probability to reach the equilibrium positions when they have the minimum energy and lead to a surface with less roughness.

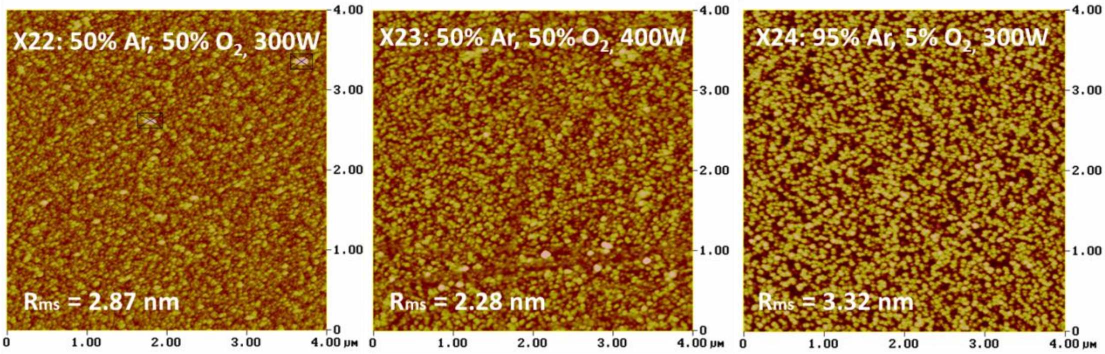

Fig 6.2: AFM photos of undoped NiO samples

6.2.2 Structural Characterization

In the following graphs (fig. 6.3) as prepared (AS) and after thermal treatment (TT1) measurements of undoped NiO samples deposited on glass are presented. As seen from graphs NiO samples presented NiO crystallographic cubic phase with a preferred (200) crystallographic plane at ~43.29° (JCPDS card No: 78-0429). EDX measurements showed that undoped NiO samples were oxygen rich (O/Ni ≈ 1.30). After thermal treatment at 300°C (TT1), the width of peaks decreased, which shows the increase of grain size. Moreover an increase of peaks' intensity was observed, which indicates the improvement of crystallinity. In some samples, an extra peak at ~38.3° was presented which did not belong to this crystallographic phase and it was very intense in the X24 sample. This peak may belong to $Ni(OH)_2$ (JCPDS card No:74-2075) and it is due to the interaction of samples with the atmosphere.

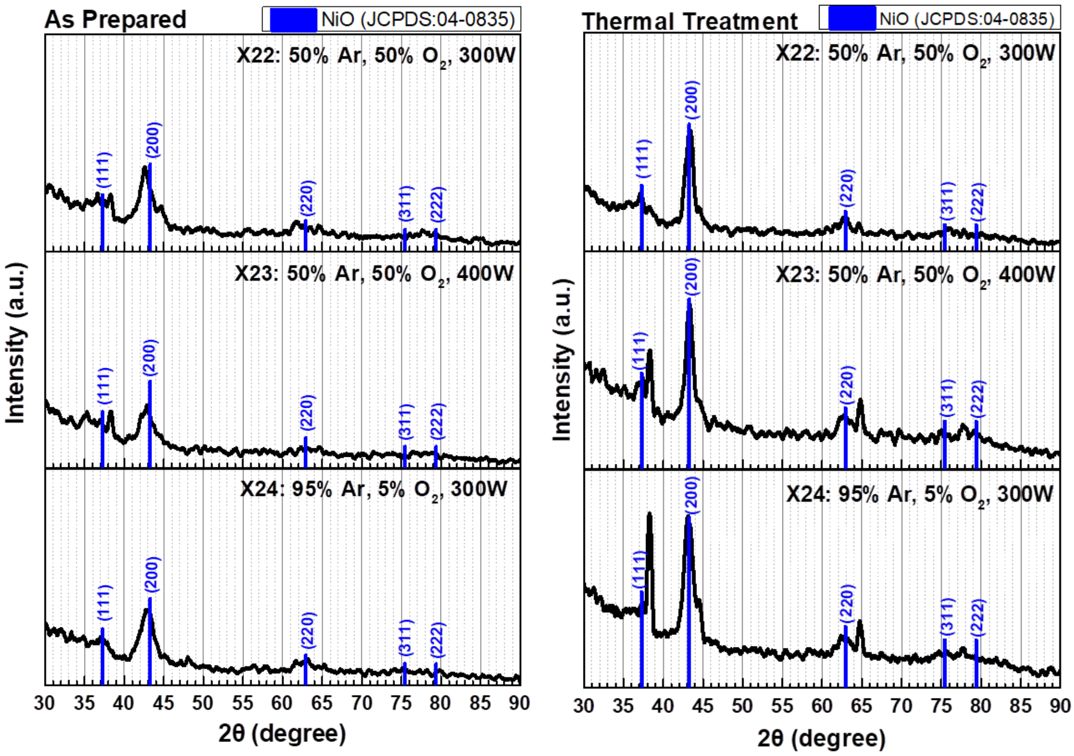

Fig. 6.3: XRD measurements before and after thermal

From analysis of XRD measurements, as mentioned in chapter 3, crystallite size, lattice strain, dislocation density, interplanar space and lattice constant can be obtained. A lot of differences between the samples were observed before and after thermal treatment (Table 2). First of all, the thermal treatment shifted the diffraction peaks to higher angles and decreased the lattice strain. This indicated that the structural disorder of the undoped NiO was decreased. Moreover the increase of crystallite size was also confirmed by analysis of XRD measurements. Finally the interplanar spacing and the lattice constant were decreased. These were due to the aggregation of the grains with thermal treatment.

Table 2: Analysis of XRD measurements (**AS**: as-prepared, **TT1**: thermal treatment at 300^oC)

NiO	Peak Position (degree)	FWHM (degree)	Crystallite Size (nm)	Lattice Strain	Dislocation Density (nm^{-2})	Interplanar spacing (Å)	Lattice Constant (Å)
X22 (50% Ar, 50% O_2, 300W)							
AS	42.56	1.58	5.33	0.0177	0.0352	2.1224	4.2448
TT1	43.40	1.14	7.44	0.0124	0.0180	2.0833	4.1665
X23 (50% Ar, 50% O_2, 400W)							
AS	42.84	2.48	3.39	0.0276	0.0868	2.1092	4.2184
TT1	43.28	0.99	8.55	0.0109	0.0137	2.0888	4.1775
X24 (95% Ar, 5% O_2, 300W)							
AS	42.98	2.02	4.18	0.0224	0.0572	2.1026	4.2053
TT1	43.14	1.35	6.24	0.0149	0.0257	2.0952	4.1904

6.2.3 Optical Characterization

The optical measurements were performed on NiO films deposited on fused silica. The optical properties of undoped NiO samples followed the structural improvements when compared the undoped NiO samples before and after thermal treatment at 300^oC (TT1). As seen in fig. 6.4 and the table 3 , the optical transmittance of as prepared NiO samples was low and with thermal treatment an increase of optical transmittance was observed. Also the absorption coefficient (α) of samples was decreased with thermal treatment in the visible spectrum range (400-750nm) as a result more photons pass the film without being absorbed. Finally, the energy gap of samples was increased. The thermal treatment improved the stoichiometry of undoped NiO samples and decreased the strain leading to less scattering of photons, as a result the samples became more transparent.

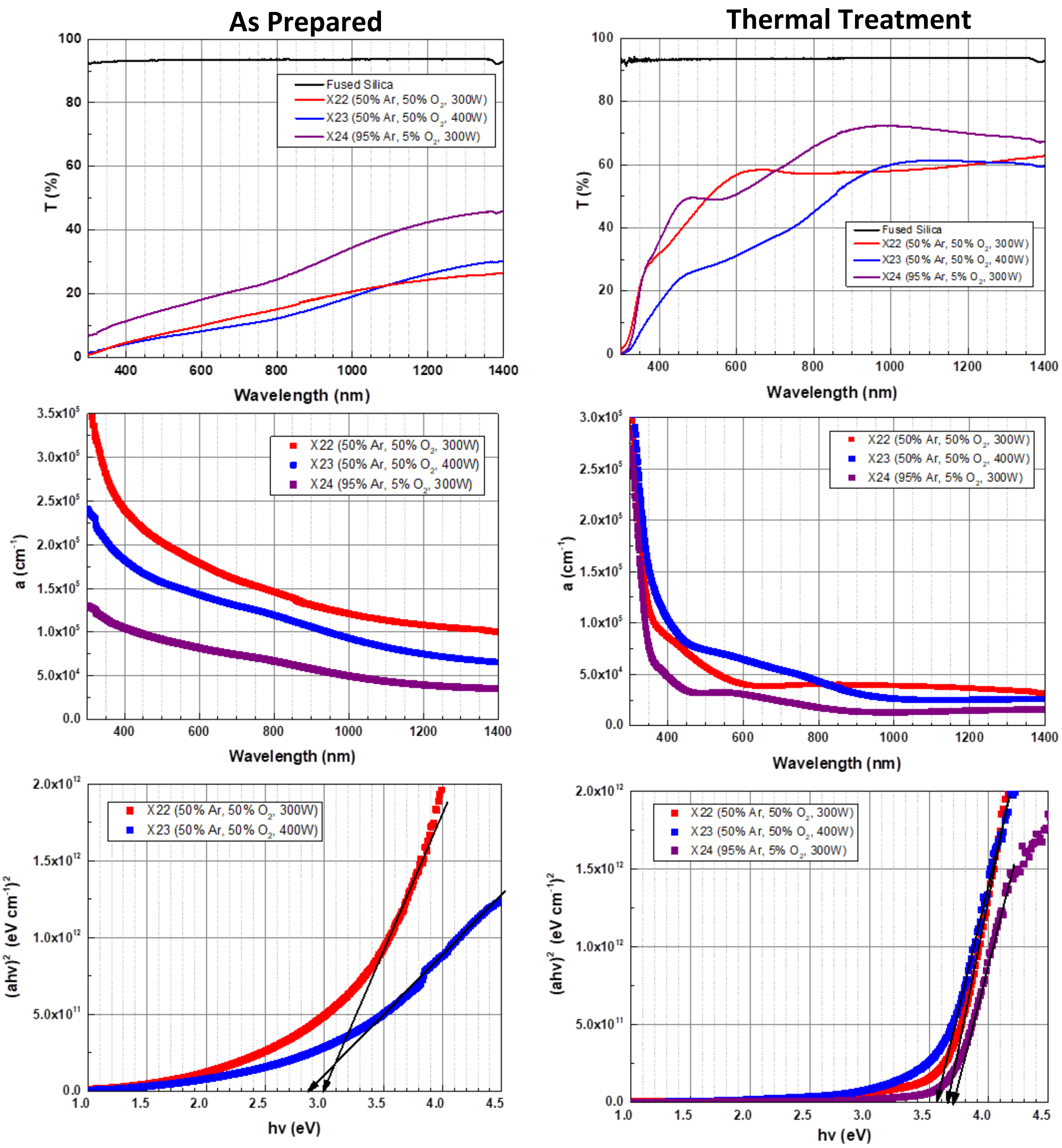

Fig. 6.4: Analysis of optical measurements before and after thermal treatment

Table 3: Analysis of optical measurements (**AS**: as-prepared, **TT1**: thermal treatment at 300°C)

NiO	T (%) (@550nm)	α (cm^{-1}) (@550nm)	E_{gap} (eV)
	X22 (50% Ar, 50% O_2, 300W)		
AS	9	$1.9\cdot10^5$	3
TT1	52	$6.9\cdot10^4$	3.7
	X23 (50% Ar, 50% O_2, 400W)		
AS	7	$1.5\cdot10^5$	2.9
TT1	28	$4.7\cdot10^4$	3.6
	X24 (95% Ar, 5% O_2, 300W)		
AS	16	$8.7\cdot10^4$	-
TT1	49	$3.2\cdot10^4$	3.8

6.2.4 Electrical Characterization

As seen in table 4 the analysis of electrical measurements of undoped NiO samples are presented. From as prepared films the X22 sample presented the least resistivity but after thermal treatment at 300°C the resistivity of all samples increased three orders of magnitude. From literature it is known that as prepared stoichiometric NiO has huge resistivity and it is transparent. So with thermal treatment the structural disorder was decreased and samples became more stoichiometric, as a result the resistivity and energy gap increased. Hall measurements proved that as prepared NiO is a p-type semiconductor with carrier concentration $\sim 2 \cdot 10^{19}$ cm^{-3} and mobility 0.77 cm^2/Vs . Also Seebeck measurements were used for proof of the p-type of NiO as seen in fig 6.5.

Table 4: Analysis of electrical measurements

NiO	**R (Ω)**		**ρ (Ω*cm)**		**Rsh (Ω/sq)**	
	AS	**TT1**	**AS**	**TT1**	**AS**	**TT1**
X22 **(50% Ar, 50% O_2, 300W)**	38k	>100M	0.24	1.56k	12k	78M
X23 **(50% Ar, 50% O_2, 400W)**	153k	>100M	0.81	1.66k	48k	98M
X24 **(95% Ar, 5% O_2, 300W)**	304k	>100M	1.90	2.17k	95k	>100M

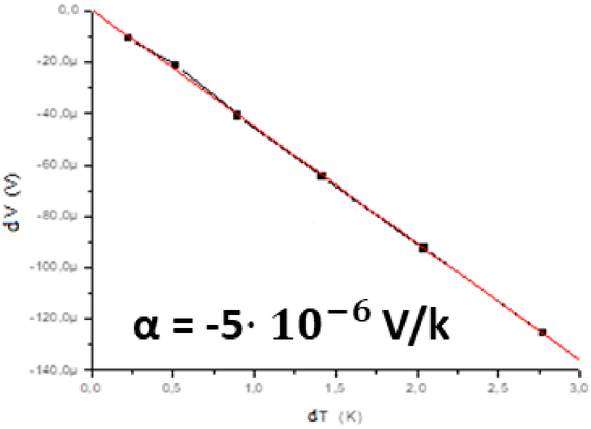

Fig. 6.5: Seebeck measurements for NiO sample

In conclusion three different undoped NiO samples were made. The X22 sample was more oxygen rich, it had the less lattice strain, it was more transparent after thermal treatment at 300°C and it had the less resistivity compared to X23 and X24 samples

6.3 Properties of Nitrogen doped NiO (NiO:N)

Nitrogen doped NiO (NiO:N) films were made from different flow rates of O_2 and N_2 gases in Ar plasma (containing 50% Ar and 50% O_2+N2), at 300W in order to observe the differences of NiO properties. All N-doped NiO grown films with their deposition conditions and their thickness are tabulated in table 5. These films (NN2, NN3, NN4) were made in plasma containing 50% Ar, as the reference NiO film (X22), but O_2 was gradually substituted by N_2 keeping the sum of their flow rates percentage equal to 50% (%O_2 + %N_2 = 50%) . The deposition rate was reduced from 1.59 nm/min for films in N_2 free plasma (X22 sample) to 1.08 nm/min for 40% N_2 in plasma (NN3 sample) because nitrogen atoms are lighter than the oxygen atoms, by gradually substituting O_2 by N_2 gas while keeping the %Ar in plasma constant. The deposition rate was further reduced to 0.58 nm/min when the deposition condition was performed in plasma containing only 6% Ar and 94% (O_2 + N_2) (NN7).

Table 5: Details for deposition conditions of nitrogen doped NiO films

NiO:N	**Flow Rates Ratio (%)**			**Deposition Time (min)**	**Thickness (nm) O:Ni**	**Deposition Rate (nm/min)**
	Ar	**O_2**	**N_2**			
X22	50	50	0	126	200	1.59
NN4	50	40	10	90	126	1.40
NN2	50	25	25	127	137	1.08
NN3	50	10	40	180	194	1.08
NN7	6	47	47	220	128	0.58

6.3.1 Surface Characterization

As seen from the following SEM photos (fig. 6.6), the typical surface morphology of N-doped NiO films did not present apparent differences between samples which contain 50% Ar and 50% (O_2 and N_2). The differences in the surface appearance of film NN7 with that of the rest films are attributed to the Ar-deficient conditions used for its deposition. However, when compared to the surface morphology of undoped NiO (X22), the nitrogen-containing films have a rougher surface with a bigger grain size

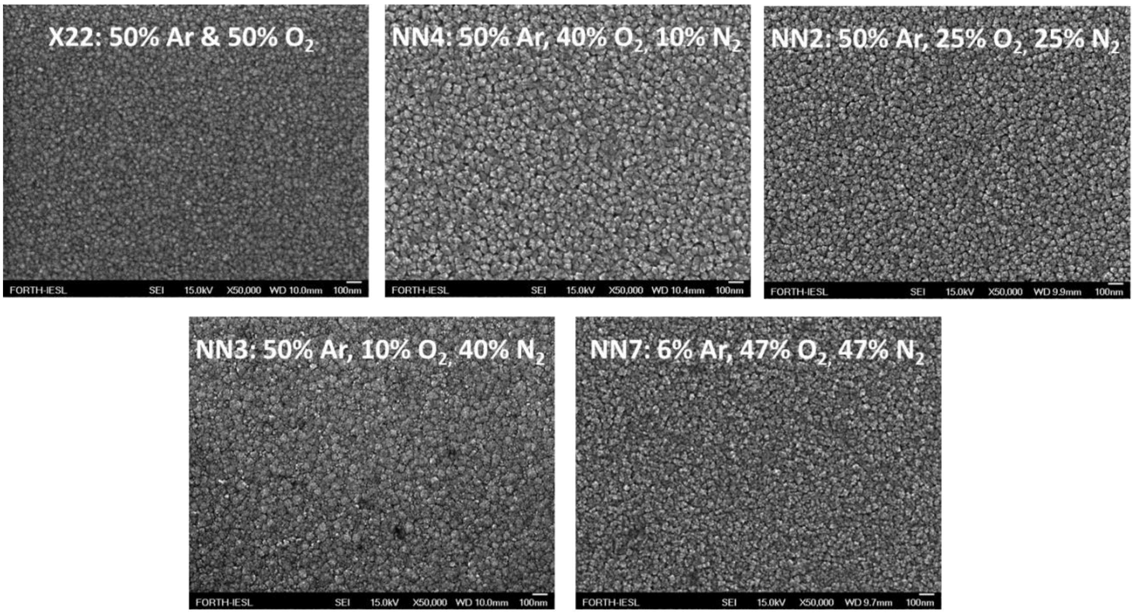

Fig 6.6: SEM photos of undoped and nitrogen doped NiO samples

From AFM measurements, differences in roughness were observed on the surface of undoped and N-doped NiO samples. As seen from fig. 6.7 the NN2 sample (50% Ar, 25% O_2 and 25% N_2) had bigger roughness (3.26nm) than X22 sample (50% Ar & 50% O_2) (2.87 nm) because of the existence of nitrogen in plasma.

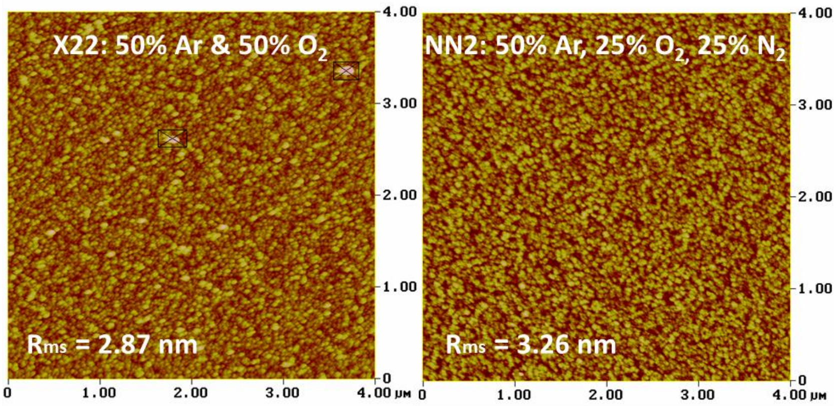

Fig 6.7: AFM photos of undoped and nitrogen doped NiO samples

6.3.2 Structural Characterization

In the following graphs (fig. 6.8) XRD measurements of as prepared (AS) N-doped NiO samples (NN2 and NN3) are presented. As seen, the introduction of nitrogen in the structure of NiO films during growth did not affect its crystallographic cubic phase. Also they remained single-phase NiO films with a preferred (200) crystallographic plane at ~43.29^o (JCPDS card No: 78-0429) and with no evidence of any other nickel oxide or nitride phases (Ni_2O_3, NixNy, etc.).

As tabulated in Table 6, upon nitrogen doping the (200) diffraction peak shifted to higher angles, the crystallite size increased and the lattice strain was reduced when compared to the respective properties of the undoped NiO. These changes were more profound for film NN2 which was grown in plasma containing 50% Ar and 50% of O_2 + N_2 with equal flow rates (O_2:N_2 = 25:25). The crystallite size of samples was increased because the ionic radius of nitrogen (1.71 Å) is bigger than oxygen (1.40 Å) or nickel (0.69 Å) and the lattice strain was reduced because with the introduction of nitrogen in samples the disorder was reduced by reducing-filling of Ni vacancies (Ni^{+3}) and/or substitution of excess oxygen by nitrogen.

An attempt was made to quantify the amount of nitrogen in NiO by EDX measurements. Taking into account that EDX cannot accurately give the at.% of light atoms such as nitrogen and that values of at.% around or less than 1% are the limit of detection above the noise signal, the existence of nitrogen in the NiO structure determined by EDX was used only as a qualitative indicator.

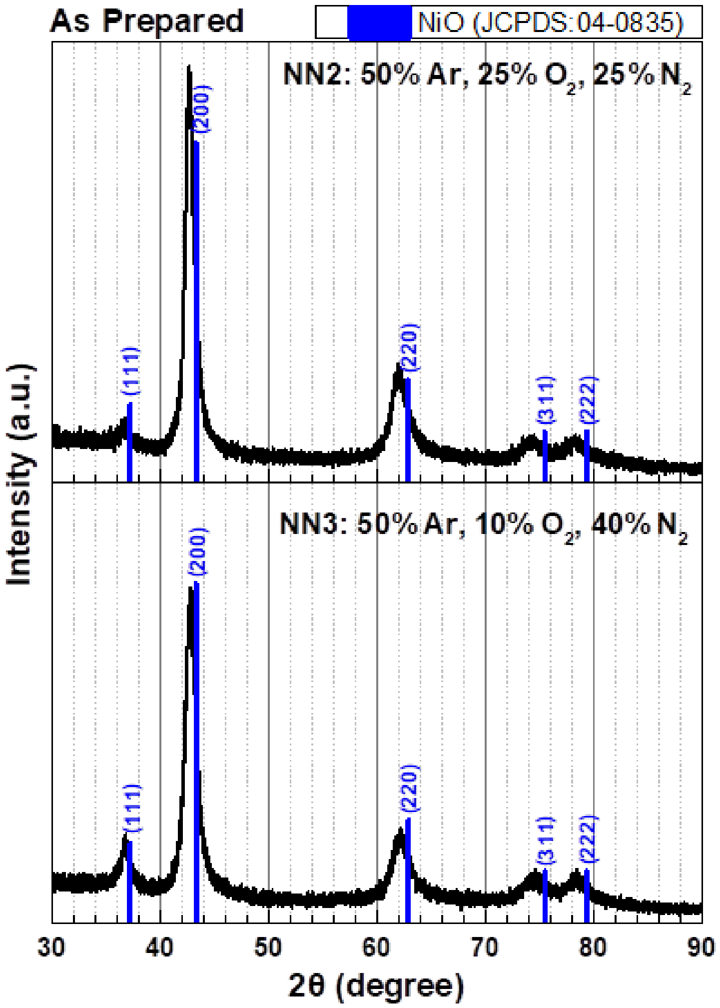

Fig. 6.8: XRD measurements of nitrogen doped NiO

Table 6: Analysis of XRD measurements (**AS**: as prepared)

	Peak Position (degree)	FWHM (degree)	Crystallite Size (nm)	Lattice Strain	Dislocation Density (nm^{-2})	Interplanar spacing (Å)	Lattice Constant (Å)
X22 (50% Ar & 50% O_2)							
AS	42.56	1.58	5.33	0.0177	0.0352	2.1224	4.2448
NN2 (50% Ar, 25% O_2, 25% N_2)							
AS	42.66	0.96	8.81	0.0107	0.0129	2.1177	4.2353
NN3 (50% Ar, 10% O_2, 40% N_2)							
AS	42.78	1.18	7.15	0.0131	0.0195	2.1120	4.2240

6.3.3 Optical Characterization

In the fig. 6.9 the transmittance, the absorption coefficient and the energy gap of N-doped NiO samples are presented. The optical properties of N-doped NiO followed the structural improvements concerning defects and strain when compared to undoped NiO as mentioned above. As seen with introduction of nitrogen in samples the optical transmittance was increased from ~10% to ~50% and after thermal treatment at 300^{o}C the transmittance was reached to ~85%. Also the absorption coefficient was reduced compared to undoped NiO, so more photons pass the film without being absorbed which could be beneficial for p-NiO/TiO_2 photovoltaics. Finally an increase in energy gap of as prepared N-doped NiO samples was observed from 3 eV to 3.7 eV. After thermal treatment undoped and N-doped NiO samples had the same energy gap. The increase in transmittance of Ndoped NiO films when compared to the undoped NiO films could be related to the decrease in Ni vacancies (Ni^{+2}) and subsequently fewer Ni^{+3} ions. It is generally agreed that a structural disorder, Ni vacancies and the presence of Ni^{+3} ions have been associated with the low transmittance of NiO. The less structural disorder and the decrease in the tensile strain of NiO upon nitrogen doping resulted in more transparent films with a larger energy gap.

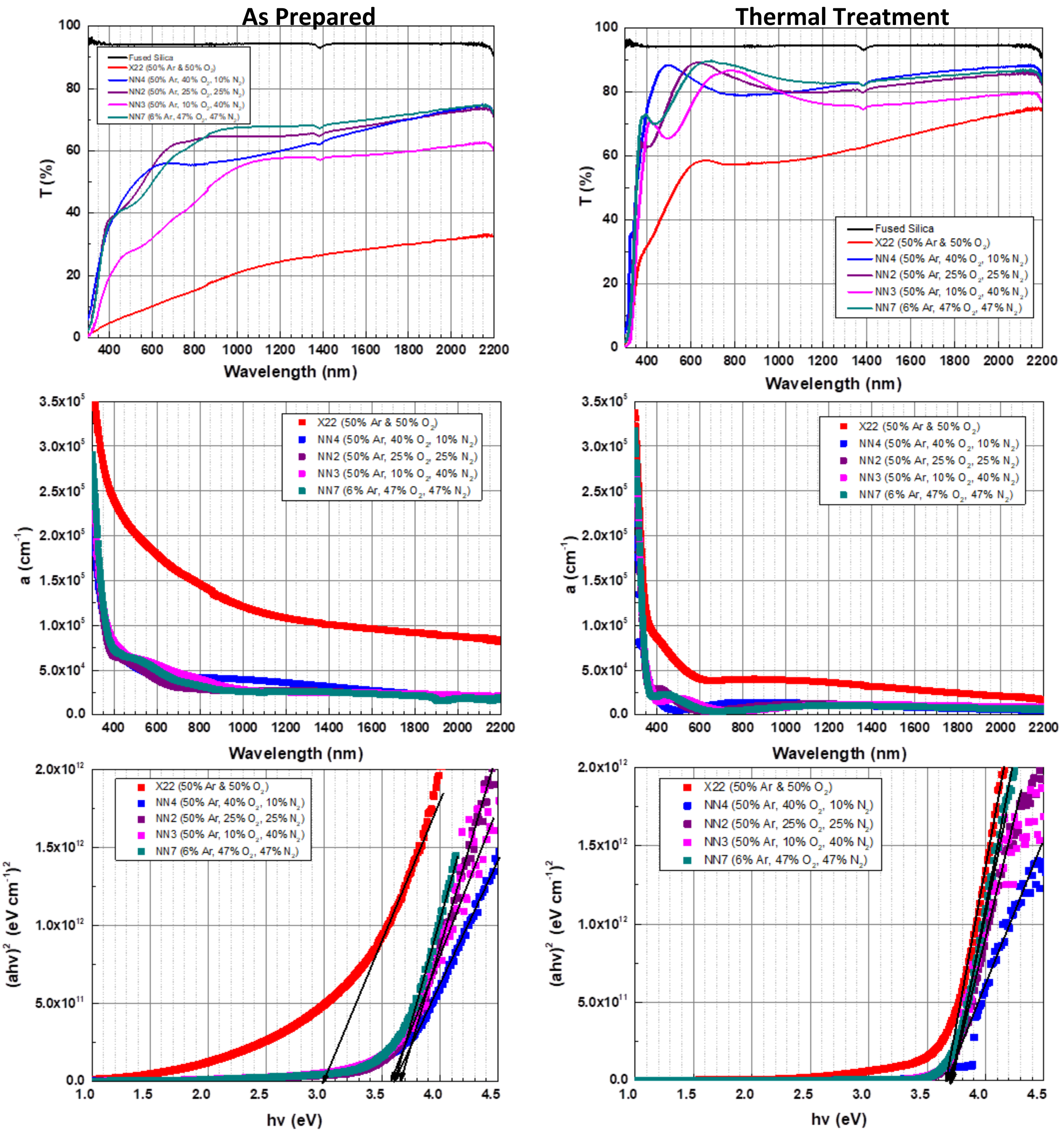

As Prepared

Thermal Treatment

Fig. 6.9: Analysis of optical measurements before and after thermal treatment

Table 7: Analysis of optical measurements (**AS**: as-prepared, **TT1**: thermal treatment at 300°C)

	T (%) (@550nm)	α (cm^{-1}) (@550nm)	E_{gap} (eV)
	X22 (50% Ar, 50% O_2)		
AS	9	$1.9 \cdot 10^5$	3
TT1	52	$6.9 \cdot 10^4$	3.7
	NN4 (50% Ar, 40% O_2 & 10% N_2)		
AS	52	$4.7 \cdot 10^4$	3.6
TT1	86	$6.6 \cdot 10^3$	3.7
	NN2 (50% Ar, 25% O_2, 25% N_2)		
AS	49	$4.7 \cdot 10^4$	3.6
TT1	85	$7.8 \cdot 10^3$	3.7
	NN3 (50% Ar, 10% O_2, 40% N_2)		
AS	29	$6.0 \cdot 10^4$	3.6
TT1	69	$1.6 \cdot 10^4$	3.7
	NN7 (6% Ar, 47% O_2, 47% N_2)		
AS	45	$5.7 \cdot 10^4$	3.6
TT1	81	$1.1 \cdot 10^4$	3.7

6.3.4 Electrical Characterization

The following table 8 contains the analysis of electrical measurements of undoped and N-doped NiO samples. As seen with the introduction of nitrogen the resistivity was increased four orders of magnitude. As mentioned above it is known that as prepared stoichiometric NiO has high resistivity and it is transparent. So with introduction of nitrogen the structural disorder was decreased and samples became more stoichiometric, as a result the resistivity and energy gap increased. Because of increase in resistivity the Hall measurements could not be performed.

Table 8: Analysis of electrical measurements

Samples	R (Ω)	ρ (Ω*cm)	Rsh (Ω/sq)
	AS	AS	AS
X22 (50% Ar & 50% O_2)	38k	0.24	12k
NN2 (50% Ar, 25% O_2, 25% N_2)	>100M	1.75k	>100M

In conclusion N-doped NiO samples were made. With introduction of nitrogen in samples, their properties changed. Their surface became rougher and the lattice strain was decreased. Also they became more transparent as a result their energy gap was increased. Finally their resistivity was increased. These changes come from the decrease of structural disorder.

6.4 Properties of Niobium doped NiO (NiO:Nb)

6.4.1 Influence of niobium doping and power on NiO properties

Niobium doped NiO (NiO:Nb) films were made by 50% Ar and 50% O_2 gases in plasma. Different number of Nb pellets was placed on the nickel target as seen in fig. 6.10. Three of samples were made to a power of 300W while other three samples were made at 400W. As seen in the following table X13 sample had 6 Nb, X14 sample had 10 Nb and X10 sample had 14Nb on the nickel target in plasma containing 50% Ar and 50% O_2 at 300W. While X12 sample had 6 Nb, X15 sample had 10 Nb and X12 sample had 14Nb on the nickel target in plasma containing 50% Ar and 50% O_2 at 400W. The deposition rate was increased with the increase of power from 300W to 400W, which shows that the sputtered atoms obtain more kinetic energy when they arrive at the substrate surface because of higher power. Finally, from EDX measurements, niobium was detected in the NiO structure and its amount depends on the number of niobium pellets and the power during the deposition.

Fig. 6.10: Niobium pellets on the nickel target of sputtering chamber

Table 9: Details for deposition conditions of niobium doped NiO films

50% Ar & 50% O_2						
Power (W)	**Samples**	**Nb (pieces)**	**Deposition Time (min)**	**Thickness (nm)**	**Deposition Rate (nm/min)**	**at.% Nb**
300	**X22**	0	126	200	1.59	0
	X13	6	105	157	1.49	0.9
	X14	10	105	141	1.34	0.9
	X10	14	105	153	1.46	2.4
400	**X23**	0	90	170	1.89	0
	X12	6	70	140	2.00	0.3
	X15	10	70	153	2.19	1.6
	X11	14	70	134	1.91	1.9

6.4.1.1 Surface Characterization

The following SEM photos (fig. 6.11) present the surface of undoped and Nb-doped NiO with the deposition conditions: 50% Ar, 50% O_2 and 300W. The surface morphology of Nb-doped NiO films (NiO:Nb) were almost the same but their surfaces were quite different from undoped NiO. Also undoped NiO had bigger grain size. Moreover in fig. 6.12, SEM photos present the surface of undoped and niobium doped NiO with the deposition conditions: 50% Ar, 50% O_2 and 400W. The surface morphology of Nb-doped NiO films was almost the same but their surfaces were quite different from undoped NiO as well. Also undoped NiO had bigger grain size. The surface of samples, which were made at 300W, presented cracks.

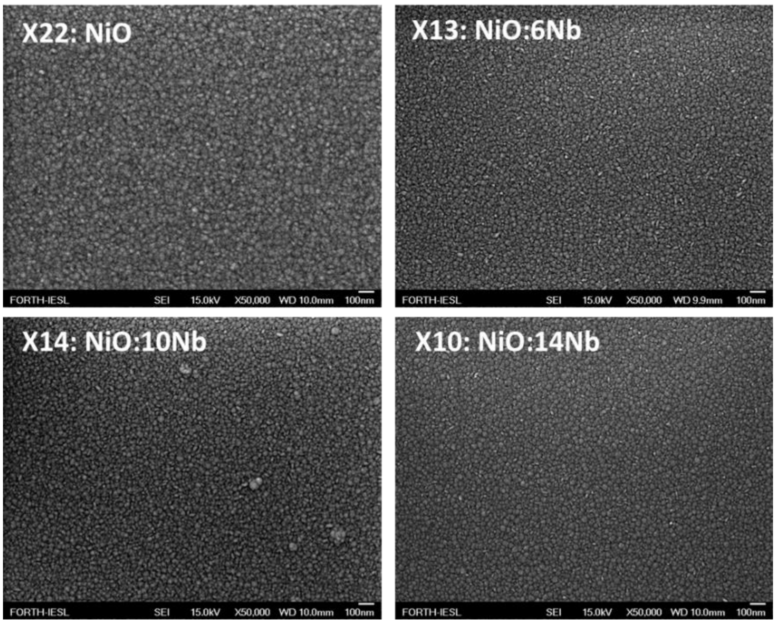

Fig 6.11: SEM photos of undoped and niobium doped NiO samples at 300W

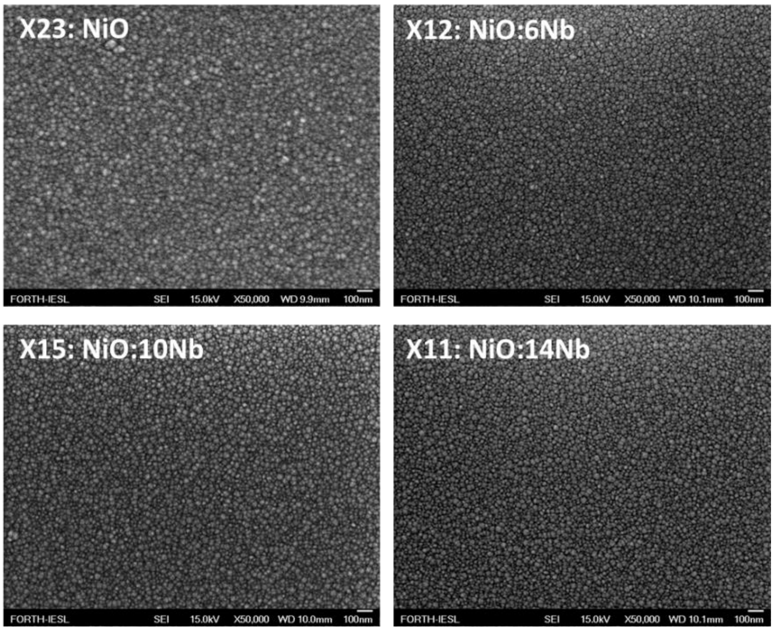

Fig 6.12: SEM photos of undoped and niobium doped NiO samples at 400W

From AFM measurements differences in roughness were observed on the surface of undoped and Nb-doped NiO samples. As seen from fig. 6.13 the X13 sample, which had 6 Nb pellets, had the lowest roughness and X22 sample which was undoped NiO, had the biggest roughness with the deposition conditions: 50% Ar, 50% O_2 at 300W. The same trend was observed in the samples with the deposition conditions: 50% Ar, 50% O_2 at 400W. Finally samples, which made at 400W, had lower roughness than those which made at 300W. It is due to the sputtered atoms obtain more kinetic energy when they arrive at the substrate surface because of higher power. Hence, they had a higher probability to reach the equilibrium positions and lead to a more perfect crystalline structure

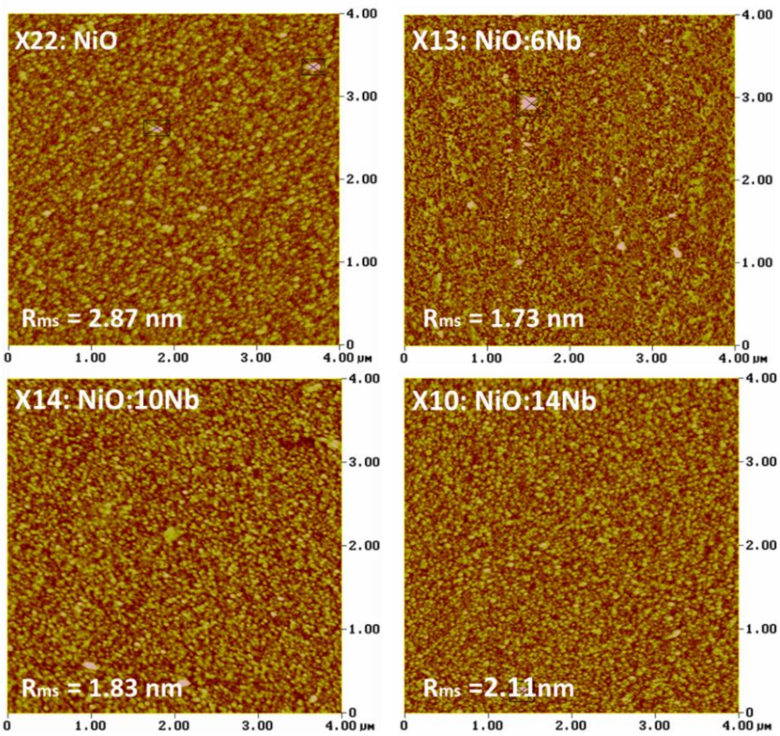

Fig 6.13: AFM photos of undoped and niobium doped NiO samples at 300W

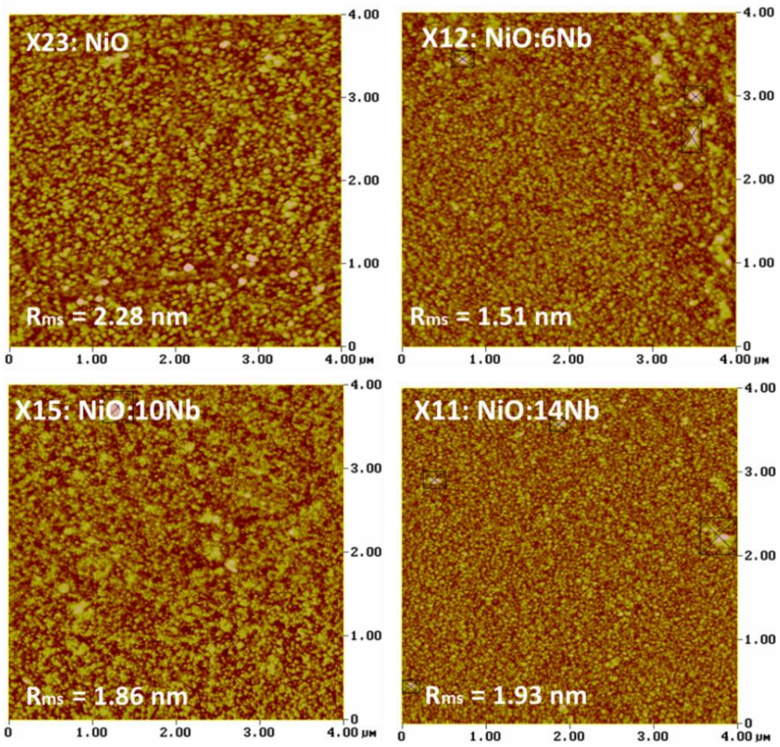

Fig 6.14: AFM photos of undoped and niobium doped NiO samples at 400W

6.4.1.2 Structural Characterization

In the following graphs (fig. 6.15) XRD measurements of Nb-boped NiO (NiO:Nb) are presented before and after thermal treatment at 300^{o}C. They presented a preferred (200) crystallographic plane at ~43.29^{o} (JCPDS card No: 78-0429) but another peak was appeared at around 38.30^{o}, which was very intense after thermal treatment. That peak probably may be due to Ni-Nb-O bond ($NiNb_2O_2$).

As tabulated in Table 10 in the Nb-doped NiO samples, which were made at 300W, the crystallite size was reduced and the lattice strain was increased when compared to the respective properties of the undoped NiO. The crystallite size of samples was reduced because the ionic radius of niobium (0.64Å) is smaller than oxygen (1.40Å) or nickel (0.69Å). The lattice strain was increased because with the introduction of niobium in samples the disorder was not reduced by reducing-filling of Ni vacancies (Ni^{+3}) and/or substitution of excess oxygen by nitrogen. After thermal treatment at 300^{o}C the diffraction peaks shifted to higher angles, the crystallite size was increased and lattice strain was reduced. This indicated that the disordered Nb-doped NiO became less disordered.

On the other hand, in the Nb-doped NiO samples, which were made at 400W, the crystallite size was increased and the lattice strain was decreased when compared to the respective properties of the undoped NiO. Probably there was an aggregation of the grains in that power because sputtered atoms had more kinetic energy. After thermal treatment at 300^{o}C the diffraction peaks shifted to higher angles, the crystallite size was increased and lattice strain was reduced. This indicated that the disordered Nb-doped NiO became less disordered.

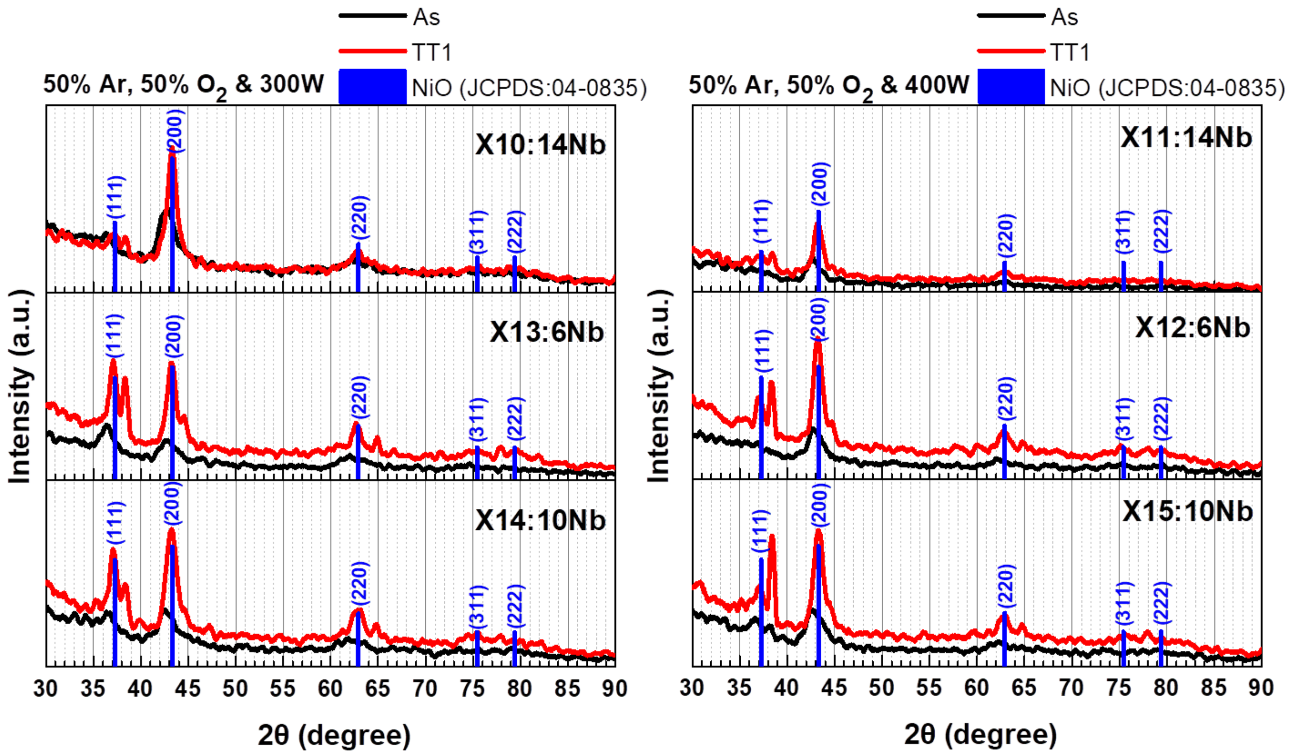

Fig. 6.15: XRD measurements

Table 10: Analysis of XRD measurements

Power (W)	NiO	Peak Position (degree)	FWHM (degree)	Crystallite Size (nm)	Lattice Strain	Dislocation Density (nm^{-2})	Interplanar spacing (Å)	Lattice Constant (Å)
	X22 (NiO)							
300	**AS**	42.56	1.58	5.33	0.0177	0.0352	2.1224	4.2448
	TT1	43.40	1.14	7.44	0.0124	0.0180	2.0833	4.1665
	X13 (NiO:6Nb)							
	AS	42.6	1.97	4.28	0.0221	0.0547	2.1205	4.2410
	TT1	43.18	1.17	7.23	0.0129	0.0191	2.0934	4.1867
	X14 (Ni0:10Nb)							
	AS	42.40	1.98	4.25	0.0223	0.0553	2.1301	4.2601
	TT1	43.24	1.32	6.41	0.0145	0.0243	2.0907	4.1814
	X10 (NiO:14Nb)							
	AS	42.84	1.88	4.49	0.0209	0.04955	2.1092	4.2184
	TT1	43.28	1.07	7.91	0.0117	0.0160	2.0888	4.1775
	X23 (NiO)							
400	**AS**	42.84	2.48	3.39	0.0276	0.0868	2.1092	4.2184
	TT1	43.28	0.99	8.55	0.0109	0.0137	2.0888	4.1775
	X12 (NiO:6Nb)							
	AS	42.66	1.72	4.91	0.0192	0.0415	2.1177	4.2353
	TT1	43.22	1.04	8.12	0.0115	0.0151	2.0915	4.1830

	X15 (NiO:10Nb)							
	AS	42.6	2.13	3.96	0.0238	0.0638	2.1205	4.2410
	TT1	43.30	1.17	7.21	0.0129	0.0192	2.0878	4.1757
	X11 (NiO:14Nb)							
	AS	42.74	1.50	5.64	0.0167	0.0314	2.1139	4.2278
	TT1	43.26	1.00	8.44	0.0110	0.0140	2.0897	4.1794

6.4.1.3 Optical Characterization

In the fig. 6.16 the transmittance, the absorption coefficient and the energy gap of undoped and Nb-doped NiO (NiO:Nb) samples are presented. As seen in table 11 with introduction of niobium in as prepared samples the optical transmittance (~10%) and the absorption coefficient were not affected in relation to the undoped NiO. Moreover undoped NiO presented bigger energy gap at 3 eV than Nb-doped NiO samples, which had energy gap 2.5 eV - 2.7 eV. After thermal treatment at 300^{o}C the transmittance was reached to ∼50%. Also the absorption coefficient was reduced compared to as prepared Nb-doped NiO, so more photons pass the film without being absorbed. Finally an increase in energy gap of thermal treatment doped NiO samples was observed from ∼2.7 eV to 3.7 eV. After thermal treatment undoped and Nb-doped NiO samples had the same energy gap. The increase in transmittance of Nb-doped NiO films after thermal treatment could be related to the decrease in Ni vacancies (Ni^{+2}) and subsequently fewer Ni^{+3} ions. It is generally agreed that a structural disorder, Ni vacancies and the presence of Ni^{+3} ions have been associated with the low transmittance of NiO. The less structural disorder and the decrease in the tensile strain of NiO resulted in more transparent films with a larger energy gap.

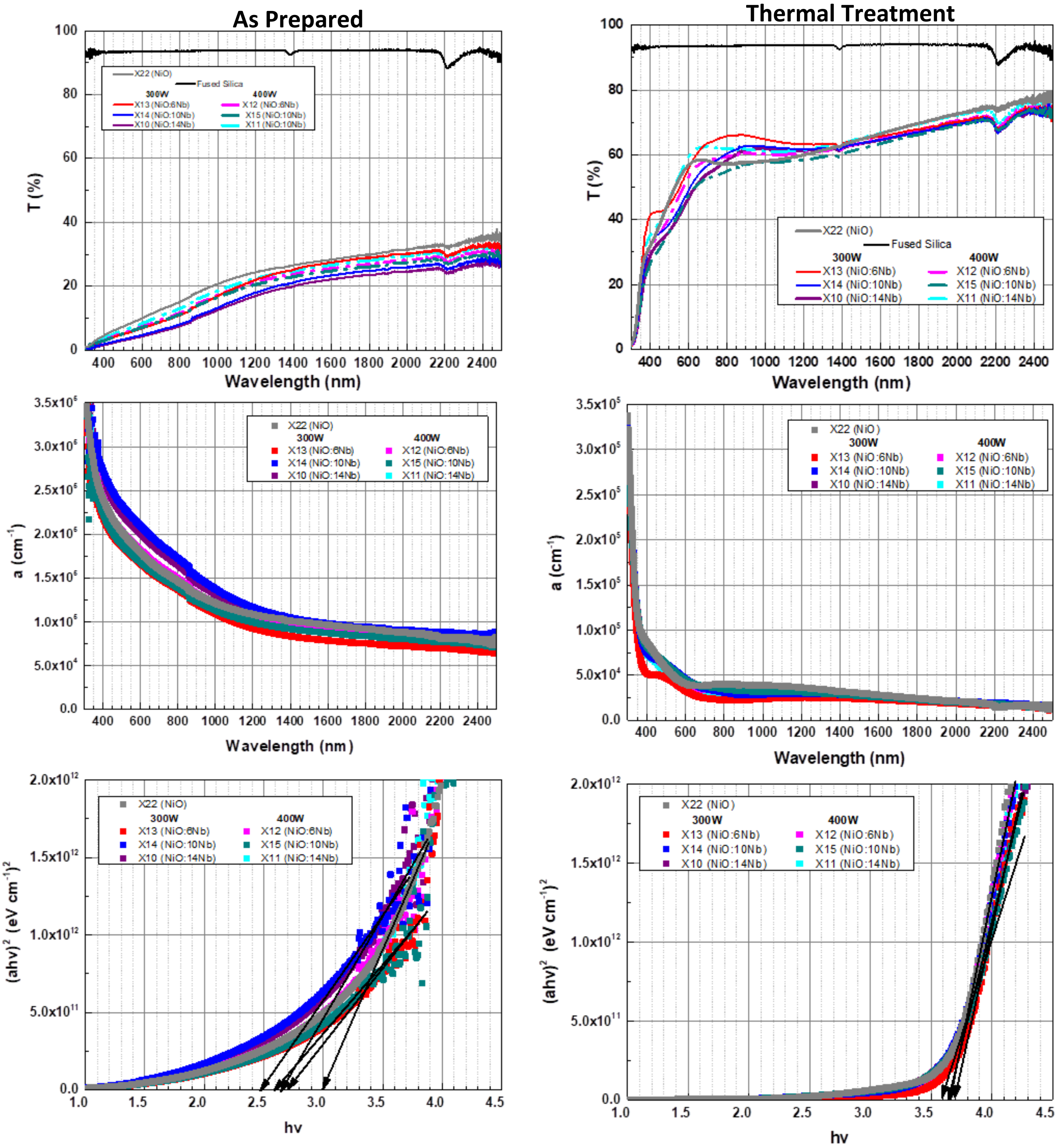

Fig. 6.16: Analysis of optical measurements before and after thermal treatment

Table 11: Analysis of optical measurements (**AS**: as-prepared, **TT1**: thermal treatment at 300°C)

Power (W)		T (%) (@550nm)	α (cm^{-1}) (@550nm)	E_{gap} (eV)
300		**X22 (NiO)**		
	AS	9	$1.9\cdot10^5$	3
	TT1	52	$6.9\cdot10^4$	3.7
		X13 (NiO:6Nb)		
	AS	6	$1.8\cdot10^5$	2.7
	TT1	49	$4.1\cdot10^4$	3.7
		X14 (Ni0:10Nb)		
	AS	4	$2.2\cdot10^5$	2.5
	TT1	43	$5.4\cdot10^4$	3.7
		X10 (NiO:14Nb)		
	AS	4	$2.1\cdot10^5$	2.7
	TT1	41	$5.4\cdot10^4$	3.7
400		**X12 (NiO:6Nb)**		
	AS	6	$1.9\cdot10^5$	2.9
	TT1	47	$4.9\cdot10^4$	3.7
		X15 (NiO:10Nb)		
	AS	6	$1.8\cdot10^5$	2.6
	TT1	42	$5.2\cdot10^4$	3.6
		X11 (NiO:14Nb)		
	AS	7	$1.9\cdot10^5$	2.9
	TT1	53	$4.2\cdot10^4$	3.7

6.4.1.4 Electrical Characterization

The following table 12 contains the analysis of electrical measurements of undoped and Nb-doped NiO samples. As seen with the introduction of niobium the resistivity was decreased. After thermal treatment at 300°C the resistivity was increased four orders of magnitude. As mentioned above it is known that as prepared stoichiometric NiO has huge resistivity and it is transparent. So after thermal treatment the disorder was decreased and samples became more stoichiometric, as a result the resistivity and energy gap increased. Hall measurements for Nb-doped NiO were unreliable. Seebeck measurements were used to confirm the p-type of Nb-doped NiO as seen in fig 6.17.

Table 12: Analysis of electrical measurements

Power (W)	NiO	R (Ω)		ρ (Ω*cm)		Rsh (Ω/sq)	
		AS	TT1	AS	TT1	AS	TT1
300W	X22 (NiO)	38k	>100M	0.24	1.56k	12k	78M
	X13 (NiO:6Nb)	125k	>100M	0.61	6.4k	39k	>100M
	X14 (NiO:10Nb)	42k	>100M	0.18	6.2k	13k	>100M
	X10 (NiO:14Nb)	60k	>100M	0.29	11k	19k	>100M
400W	X23 (NiO)	153k	>100M	0.81	1.66k	48k	98M
	X12 (NiO:6Nb)	78k	>100M	0.34	4.4k	24k	>100M
	X15 (NiO:10Nb)	70k	>100M	0.33	5.3k	22k	>100M
	X11 (NiO:14Nb)	65k	>100M	0.27	11.3k	20k	>100M

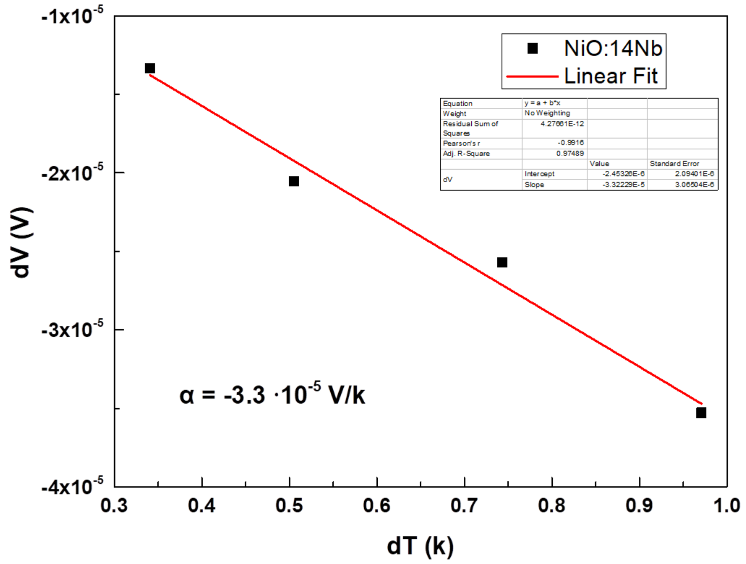

Equation	y = a + b*x		
Weight	No Weighting		
Residual Sum of Squares	4.27661E-12		
Pearson's r	-0.9916		
Adj. R-Square	0.97489		
		Value	Standard Error
dV	Intercept	-2.45326E-6	2.09401E-6
	Slope	-3.32229E-5	3.06504E-6

Fig. 6.17: Seebeck measurements for X10 sample

To summarize, different numbers of Nb pellets were used on nickel target with the purpose of detection of Nb in EDX measurement and observation of changes in properties of samples because of different numbers niobium. Nb-doped NiO had less rough surface than undoped NiO. In the Nb-doped NiO samples, which were made at 300W, the crystallite size was reduced and the lattice strain was increased when compared to the respective properties of the undoped NiO. On the other hand, in the Nb-doped NiO samples, which were made at 400W, the crystallite size was increased and the lattice strain was decreased when compared to the respective properties of the undoped NiO. As prepared Nb-doped NiO samples had low transmittance but after thermal treatment their transmittance and energy gap were increased. Also after thermal treatment the resistivity was increased four orders of magnitude. With thermal treatment the structural disorder of samples was reduced and the samples became more stoichiometric. So, Nb did not affect the optical and electrical properties of as prepared samples and they changed only after thermal treatment.

6.4.2 Influence of plasma and Nb pellets' positions on NiO properties

In the following measurements the influence of plasma and Nb pellets' positions on nickel target on NiO properties was examined. Two different conditions of plasma were examined. The first was 50% Ar & 50% O_2 at 300W, while the second was 95% Ar & 5% O_2 at 300W. The deposition time for all fabrications was 100 min. Moreover as seen in fig. 6.18 fifteen Nb pellets were used, which were deposited in different position on nickel target. In the X16 and X17 samples all Nb pellets were gathered in the center of the target. In the X18 and X19 samples Nb pellets covered almost half of the surface of the target, while in the X20 and X21 samples Nb pellets covered roughly 75% of the surface of the target.

Fig. 6.18: Niobium pellets on the nickel target of sputtering chamber

As seen in the following table the deposition rates for 95% Ar and 5% O_2 gases in plasma were bigger because the sputtered atoms obtain more kinetic energy because of higher content of Ar in plasma. For the same position of Nb pellets on nickel target but different gases in plasma as well the deposition rates for 95% Ar and 5% O_2 gases in plasma were bigger. In the following fig. 6.19 the previous remarks can be observed. On the x-axis the percentage coverage of nickel target from pellets is presented.

Table 13: Details for deposition conditions of niobium doped NiO films

Flow rates ratio (%)	Samples	Thickness (nm)	Deposition Rate (nm/min)	at.% Nb
50% Ar & 50% O_2	**X16**	171	1.71	1.8
	X18	142	1.42	1.1
	X20	110	1.10	1.6
95% Ar & 5% O_2	**X17**	183	1.83	2.9
	X19	165	1.65	3.6
	X21	152	1.52	2.3

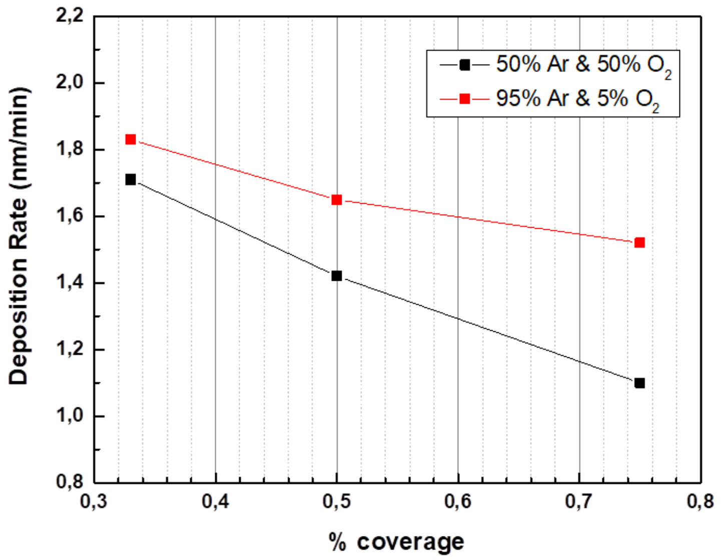

Fig. 6.19: Deposition Rate vs % coverage

6.4.2.1 Surface Characterization

The following SEM photos (fig. 6.20) present the surface Nb-doped NiO (NiO:Nb) with the deposition conditions: Ar:O_2 = 50:50, and Ar:O_2 = 95:5 at 300W respectively. Differences were observed between films with different deposition conditions. As seen, the films which grown with 95% Ar and 5% O_2 in plasma had bigger grain size than the corresponding samples. Moreover AFM measurements of films with 95% Ar and 5% O_2 present bigger roughness, which indicates that the amount of Ar affects the surface morphology of samples.

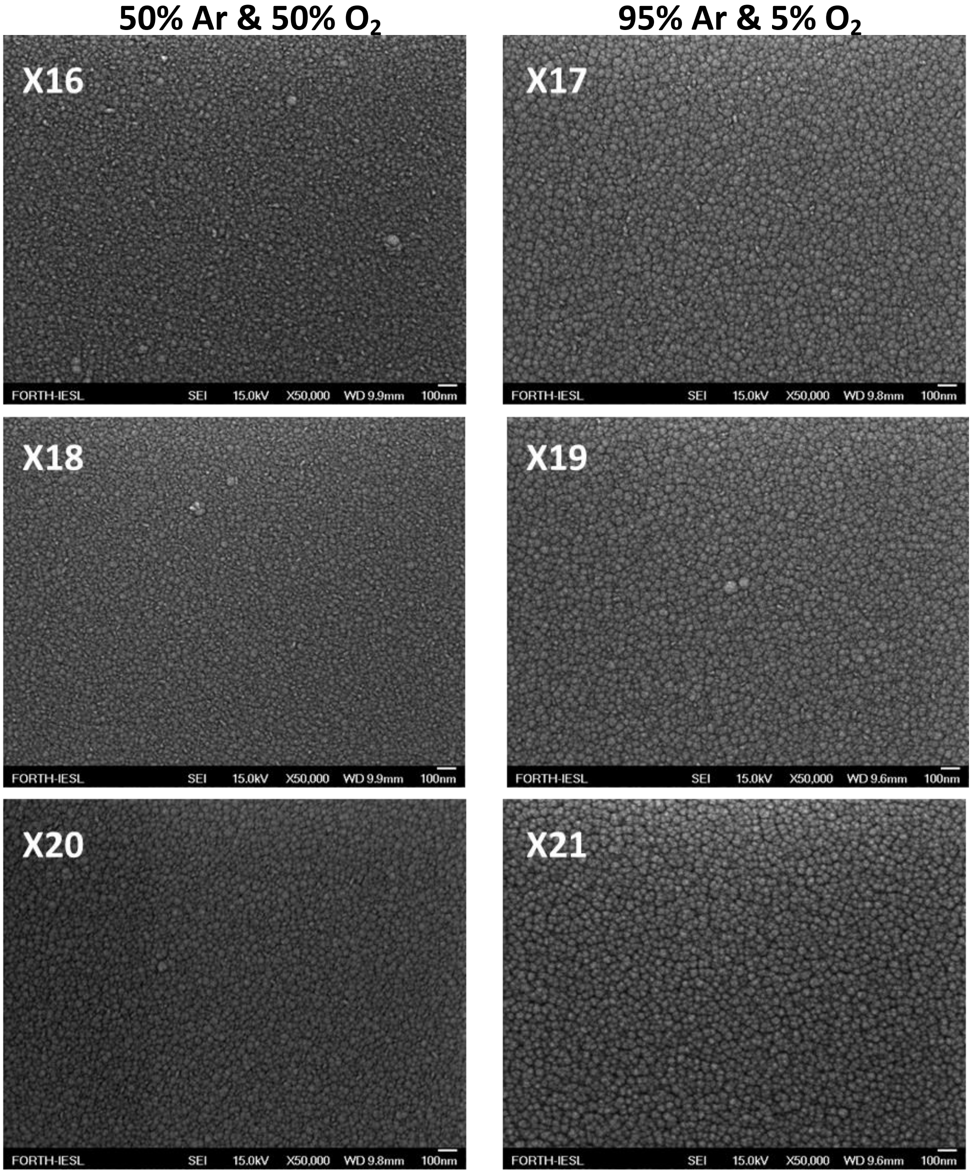

Fig 6.20: SEM photos of niobium doped NiO samples

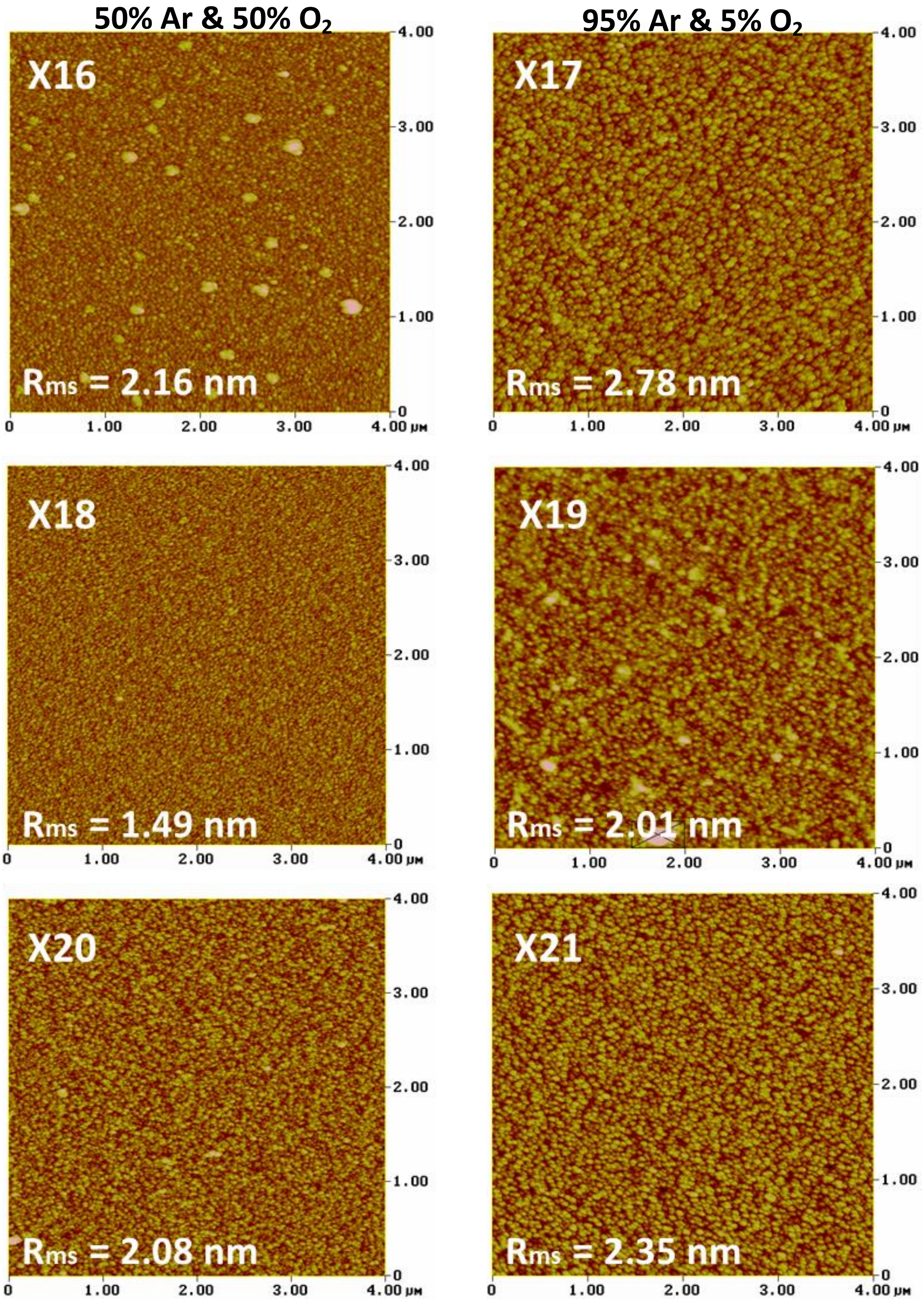

Fig 6.21: AFM photos of niobium doped NiO samples

To summarize, the higher content of Ar in plasma (95%) increased the deposition rate and grains size were bigger than samples which had 50% Ar in plasma respectively. Also these samples had bigger roughness because the plasma was more energetic.

6.4.3 Influence of Argon (Ar) on NiO properties

In the following measurements the influence of Ar on properties of Nb-doped NiO was examined. Two samples were fabricated in plasma which contained higher content of Ar (95% and 97.2% respectively) and the third sample contained less content of Ar (5%). Fourteen Nb pellets were placed on the nickel target covering roughly the 75% of target surface (fig. 6.18) and during deposition the power was 300W. As seen in the table 14, the deposition rate was increased with increase of Ar in plasma because the Ar atoms are heavier and distract more atoms from the target.

Table 14: Information of deposition conditions

Samples	Flow rates ratio (%)		Deposition Time (min)	Thickness (nm)	Deposition Rate (nm/min)	at.% Nb
	Ar	O_2				
X25	95	5	100	170	1.70	3.0
X26	97.2	2.8	95	181	1.90	4.3
X33	5	95	140	160	1.14	1.4

6.4.3.1 Surface Characterization

The following SEM photos (fig. 6.22) present the surface Nb-doped NiO (NiO:Nb) with the different content of Ar in plasma. As seen the films, which grown with 95% Ar and 5% O_2 in plasma, had bigger grain size and cracks. On the other hand the sample X33 had smaller grain size, which indicates that with huge amount of Ar the sputtered atoms obtain more kinetic energy when they arrive at the substrate surface as a result the creation of bigger grains.

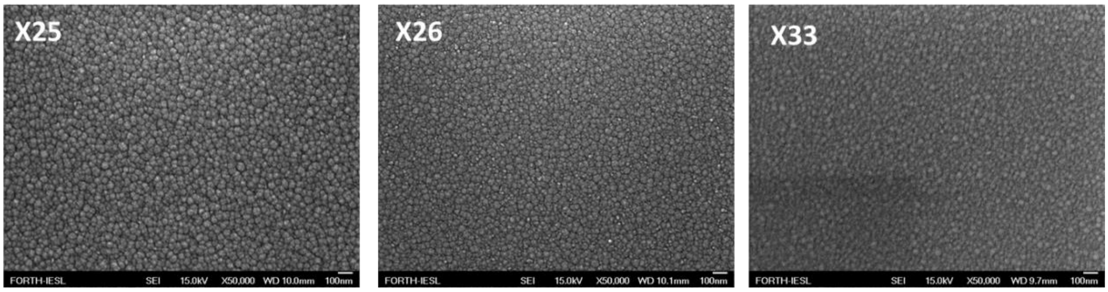

Fig 6.22: SEM photos of niobium doped NiO samples

6.4.3.2 Structural Characterization

In the following graphs (fig. 6.23) XRD measurements of Nb-doped NiO (NiO:Nb) are presented. In these samples huge amount of Ar was used during the deposition. Also XRD measurements of niobium pellets, which were used, are presented. As seen, the introduction of niobium in the structure of NiO films during growth did not affect its crystallographic cubic phase. Also they were presented single-phase NiO films with a preferred (200) crystallographic plane at ~43.29° (JCPDS card No: 78-0429)

As tabulated in Table 15 the crystallite size of Nb-doped NiO samples was increased in relation to X24 sample, which was undoped NiO, while the lattice strain was reduced. There was an aggregation of the grains because sputtered atoms had more kinetic energy due to Ar.

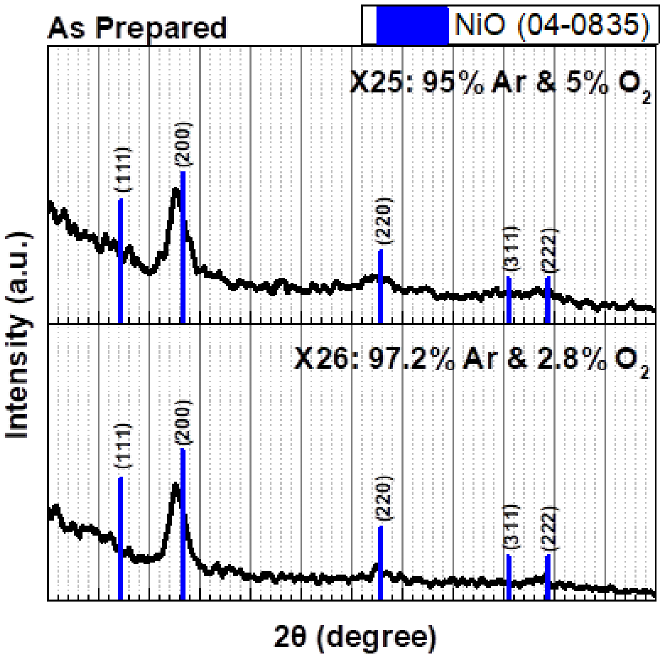

Fig. 6.23: XRD measurements

Table 15: Analysis of XRD measurements

Samples	Peak Position (degree)	FWHM (degree)	Crystallite Size (nm)	Lattice Strain	Dislocation Density (nm^{-2})	Interplanar spacing (Å)	Lattice Constant (Å)
X24 (95% Ar & 5% O_2)							
AS	42.98	2.02	4.18	0.0224	0.0572	2.1026	4.2053
X25 (95% Ar, 5% O_2 & 14Nb)							
AS	42.64	1.93	4.36	0.0216	0.0525	2.1186	4.2372
X26 (97.2% Ar, 2.8% O_2 & 14Nb)							
AS	42.60	1.72	4.90	0.0193	0.0416	2.1205	4.2410

6.4.3.3 Optical Characterization

In the fig. 6.24 the transmittance, absorption coefficient and energy gap of these samples are presented. As seen in table 16 the optical transmittance was very low (~10%), which indicates that there was structural disorder in the samples. From calculation of energy gap, X33 sample, which had 95% O_2 gas in plasma, presented the lower energy gap.

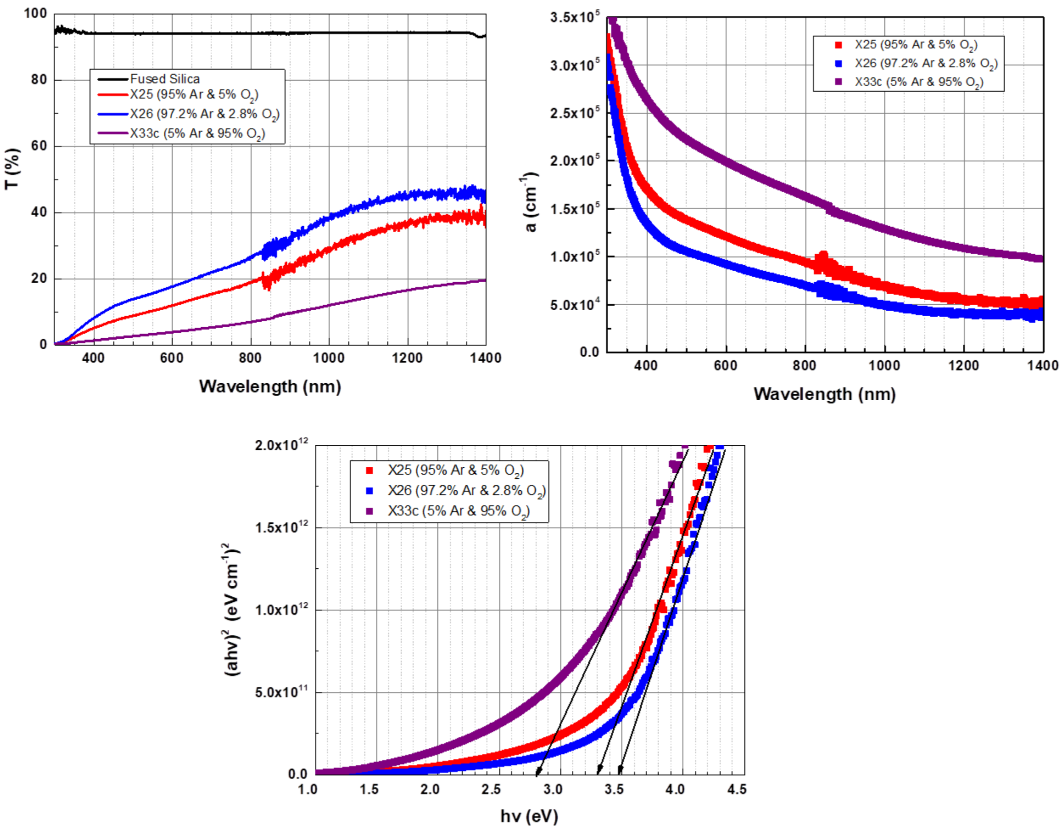

Fig. 6.24: Analysis of optical measurements

Table 16: Analysis of optical measurements (**AS**: as-prepared)

	T (%) (@550nm)	**α (cm^{-1}) (@550nm)**	**E_{gap} (eV)**
	X25 (95% Ar, 5% O_2 & 14Nb)		
AS	10	$1.3·10^5$	3.3
	X26 (97.2% Ar, 2.8% O_2 & 14Nb)		
AS	16	$9.9·10^4$	3.5
	X33c (5% Ar, 95% O_2 & 14Nb)		
AS	3	$2.1·10^5$	2.8

6.4.3.4 Electrical Characterization

The following table 17 contains the analysis of electrical measurements of Nb-doped NiO samples. As seen the samples, which had higher content of Ar gas in plasma, presented huge resistivity while X33 sample, which had higher content of O_2 gas in plasma, presented lower resistivity. So, the amount of Ar gas or O_2 gas in plasma affects the electrical properties of films.

Table 17: Analysis of electrical measurements

NiO:Nb	**R (Ω)**	**ρ (Ω*cm)**	**Rsh (Ω/sq)**
	AS	**AS**	**AS**
X25	0.5M	2.80	0.16M
X26	1.7M	9.52	0.53M
X33c	14k	0.07	4.4k

To summarize, when a sample had higher content of Ar in plasma during deposition it had rougher surface. While the sample with oxygen rich plasma had lower transmittance, higher absorption coefficient and low energy gap but its resistivity is lower than the samples with higher content of Ar in plasma.

6.4.4 Thick Samples

Finally the influence of the samples' thickness in the surface was examined. The following table contains thick films and the corresponding thin films at the same deposition conditions. There were ten Nb pellets on the nickel target and the power was at 300W. The index b indicates the thick samples. The 3N0 samples were made in 100% Ar gas in plasma, the X10 samples in 50% Ar and 50% O_2 gases, the X28 samples were made in 50% Ar, 25% O_2 and 25% N_2 gases, while the X32 samples in 5% Ar and 95% O_2 gases in plasma.

Table 18: Information of deposition conditions

Samples	**Flow rates ratio (%)**			**Deposition Time (min)**	**Thickness (nm)**	**Deposition Rate (nm/min)**	**at.% Nb**
	Ar	**O_2**	**N_2**				
3N0	100	0	0	28	120	4.29	3.2
3N0b				120	660	5.50	3.3
X10	50	50	0	105	153	1.46	2.4
X10b				285	400	1.40	2.2
X28	50	25	25	113	164	1.45	2.5
X28b				255	380	1.49	1.5
X32	5	0	95	120	142	1.18	0
X32b				270	824	3.05	0.8

As seen from the SEM photos the thick films had bigger grain size and as the content of nitrogen gas increased in the plasma as the grains were increased. The X32b samples had the biggest thickness (824nm) and it presented octahedrons. Its surface is very different from the other films and it is due to the huge amount of nitrogen in plasma.

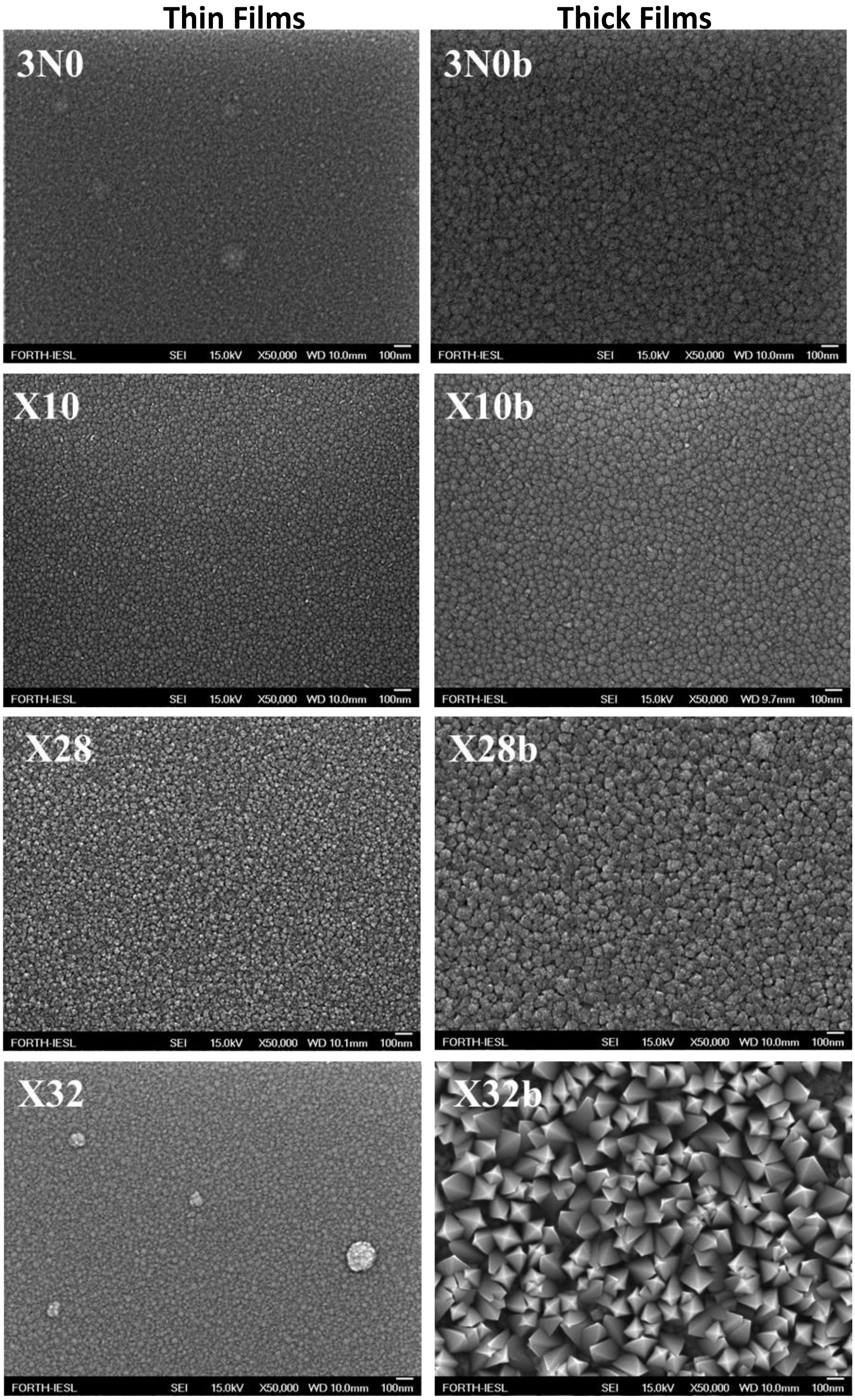

Fig 6.25: SEM photos of thin and thick niobium doped NiO samples

6.5 Properties of double doped NiO (NiO:Nb-N)

Double doped NiO films with dopants niobium and nitrogen (NiO:Nb-N) were made in different percentages gases in plasma for the investigation of their properties. Fourteen Nb pellets were used as seen in fig. 6.26 and the power of deposition was at 300W. These conditions were selected because the detection of Nb from EDX with 14Nb on nickel target was sure and the power of 300W does not make cracks on sample surface. As seen in table 15 all films had nitrogen gas in plasma which was increased gradually. The first sample had only 3% N_2 in plasma and the last sample, which was X32, had arrived to have 95% N_2 in plasma. Also the first three samples (X27-X29) had been reducing Ar in plasma (from 94% to 6%) but keeping equal the ratio of O_2:N_2. The last three samples (X30-X32) were made in N_2-rich plasma. The deposition rates were decreasing with increasing of N_2 gas in plasma because the nitrogen atoms are lighter than argon atoms as a result a few atoms of target are extracted and arrive to substrate. Moreover with increase of nitrogen gas in plasma it is difficult to detect niobium in the samples from EDX measurements because the amount is very low.

Fig. 6.26: Niobium pellets on the nickel target

Table 19: Information of deposition conditions

Samples	Flow rates ratio (%)			Deposition Time (min)	Thickness (nm)	Deposition Rate (nm/min)	at.% Nb
	Ar	O_2	N_2				
X27	94	3	3	100	161	1.61	3.8
X28	50	25	25	113	164	1.45	2.5
X29	6	47	47	200	260	1.30	3.2
X30	0	10	90	50	48	0.96	0
X31	5	5	90	115	113	0.98	0
X32	5	0	95	120	142	1.18	0

6.5.1 Surface Characterization

The following SEM photos (fig. 6.27) present the surface of double doped NiO (NiO:Nb-N) samples with the different deposition conditions in plasma. As seen and looking from X27 to X29 samples, which were made in reducing Ar plasma, the film were becoming more porous and less dense. In addition the X29 sample (6% Ar, 47% O_2 & 47% N_2) presents a different surface morphology from the rest films because it is the thickest film. Consequently, the grain size depends on the thickness of samples. Also very low deposition rate was observed for the film X30, made in Ar-free plasma, which increased lightly when a small amount of Ar gas was introduced in plasma. Films in N_2-rich and Ar+O_2 deficient plasma (X30-X32) showed entirely different morphology from films which contained much less N_2 in plasma (X27-X29).

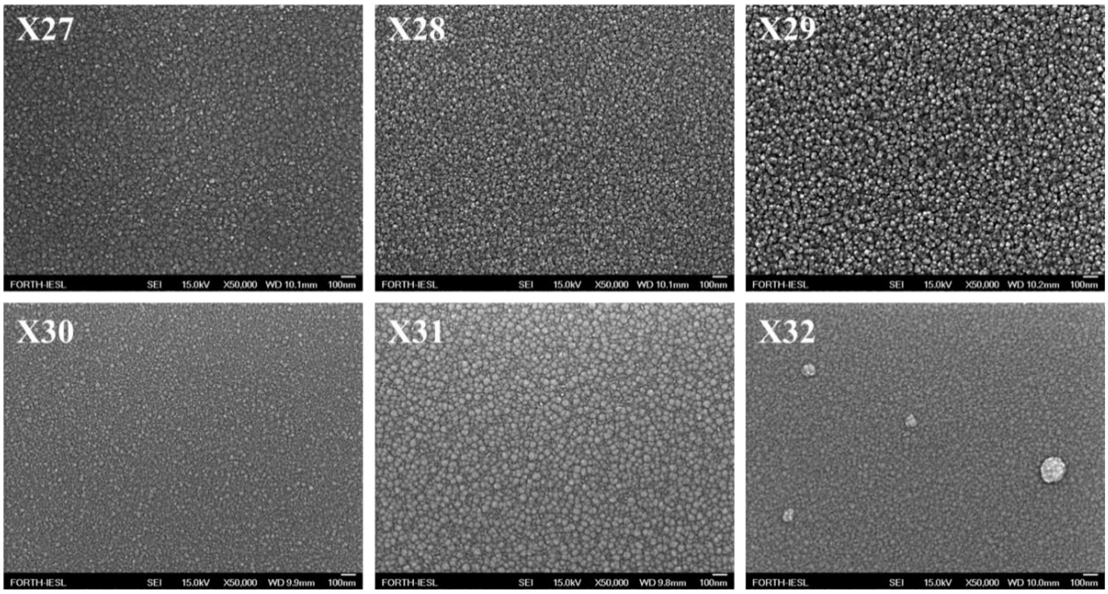

Fig 6.27 SEM photos of double doped NiO samples

From AFM measurements, differences in films' roughness were observed on the surface of double doped NiO samples. The X29 sample, which had the biggest thickness, presented also the biggest roughness. Also the X30 sample with 40nm thickness, it presented the lower roughness, so the roughness depends on the thickness directly.

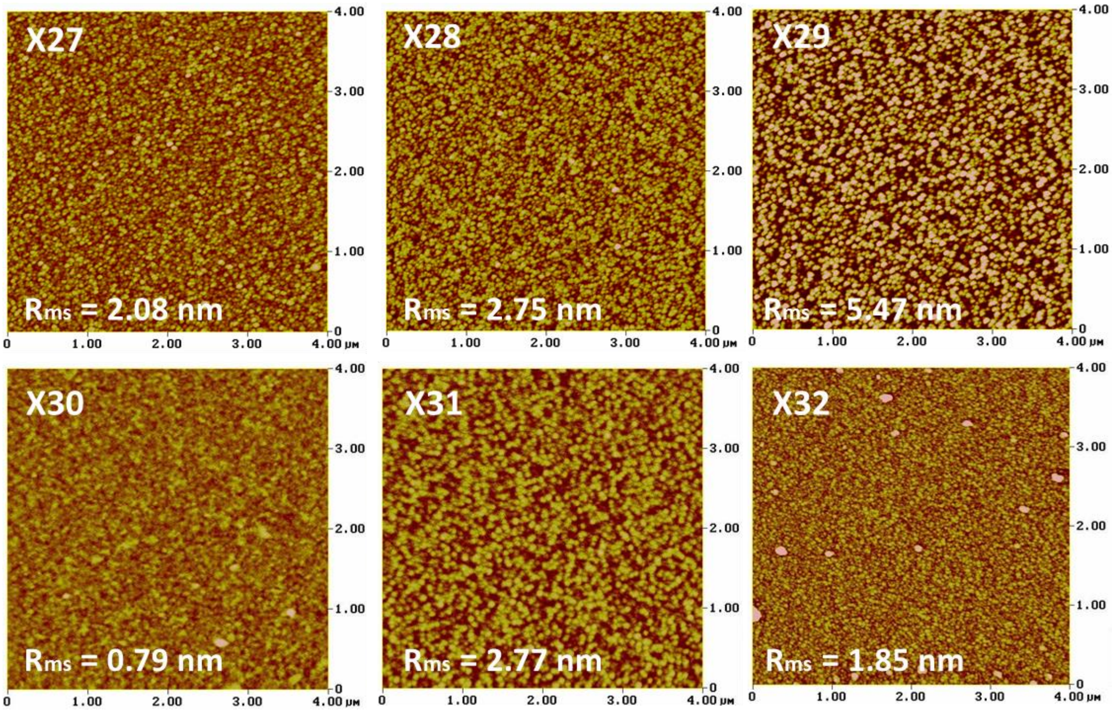

Fig 6.28: AFM photos of double doped NiO samples

6.5.2 Structural Characterization

In the following graphs (fig. 6.29) XRD measurements of double doped NiO (NiO:Nb-N) are presented. As seen, the double doping in NiO films during growth did not affect the crystallographic cubic phase of undoped NiO film. The films presented a preferred (200) crystallographic plane at ~43.29^{o} (JCPDS card No: 78-0429). The X28 and X29 samples also presented an extra peak at ∼38.30^{o}, which could probably from Nb-Ni-O phase and required further investigation. In the table 20 the analysis of XRD measurements are presented. The samples with reducing Ar in plasma (X27-X29) showed decrease of diffraction and lattice strain but increase of crystallite size.

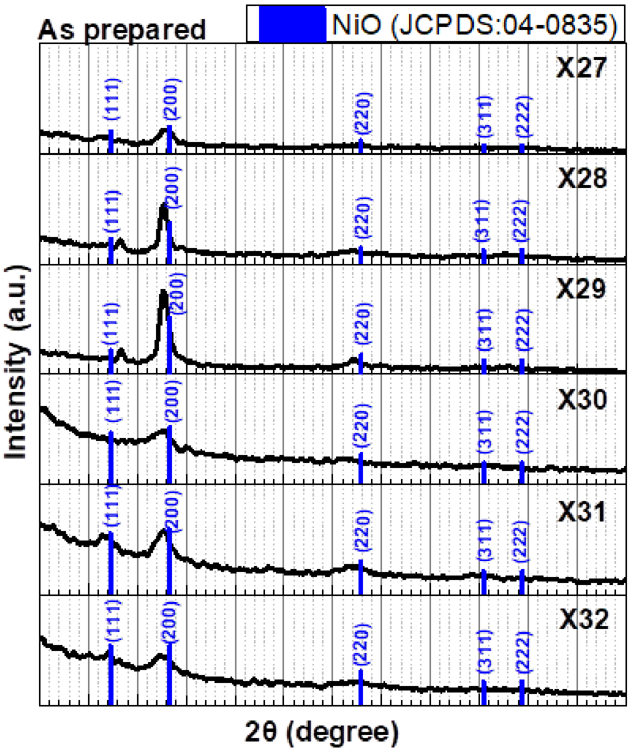

Fig. 6.29: XRD measurements

Table 20: Analysis of XRD measurements

	Peak Position (degree)	FWHM (degree)	Crystallite Size (nm)	Lattice Strain	Dislocation Density (nm^{-2})	Interplanar spacing (Å)	Lattice Constant (Å)
X27 (94% Ar, 3% O_2 , 3% N_2 & 14Nb)							
AS	42.86	1.54	5.49	0.0171	0.0332	2.1083	4.2165
X28 (50% Ar, 25% O_2, 25% N_2 & 14Nb)							
AS	42.66	0.84	10.07	0.0094	0.0099	2.1177	4.2353
X29 (6% Ar, 47% O_2 , 47% N_2 & 14Nb)							
AS	42.66	1.08	7.80	0.0121	0.0164	2.1177	4.2353
X30 (10% O_2, 90% N_2 & 14Nb)							
AS	42.68	2.11	4.00	0.0235	0.0625	2.1167	4.2335
X31 (5% Ar, 5% O_2, 90% N_2 & 14Nb)							
AS	42.74	1.67	5.06	0.0186	0.0391	2.1139	4.2278
X32 (5% Ar, 95% N_2 & 14Nb)							
AS	42.28	3.01	2.80	0.0339	0.1274	2.1358	4.2716

6.5.3 Optical Characterization

In the fig. 6.30 the transmittance, absorption coefficient and energy gap of double doped NiO samples are presented. From table 21 the results of optical measurements for double doped NiO (NiO:Nb-N) and nitrogen doped NiO (NiO:N) are summarized. As seen all as prepared samples had low transmittance at 550nm but after thermal treatment at 300°C their transmittance was increased. Also the as prepared double doped NiO (NiO:Nb-N) samples had lower transmittance than that single doped NiO (NiO:N) but after thermal treatment all samples had the same energy gap at 3.7 eV. To summarize, the as prepared double doped NiO samples had structural disorder but after thermal treatment it was reduced. On the other hand the nitrogen doped NiO had less structural disorder due to the introduction only nitrogen, as a result the energy gap after thermal treatment did not change.

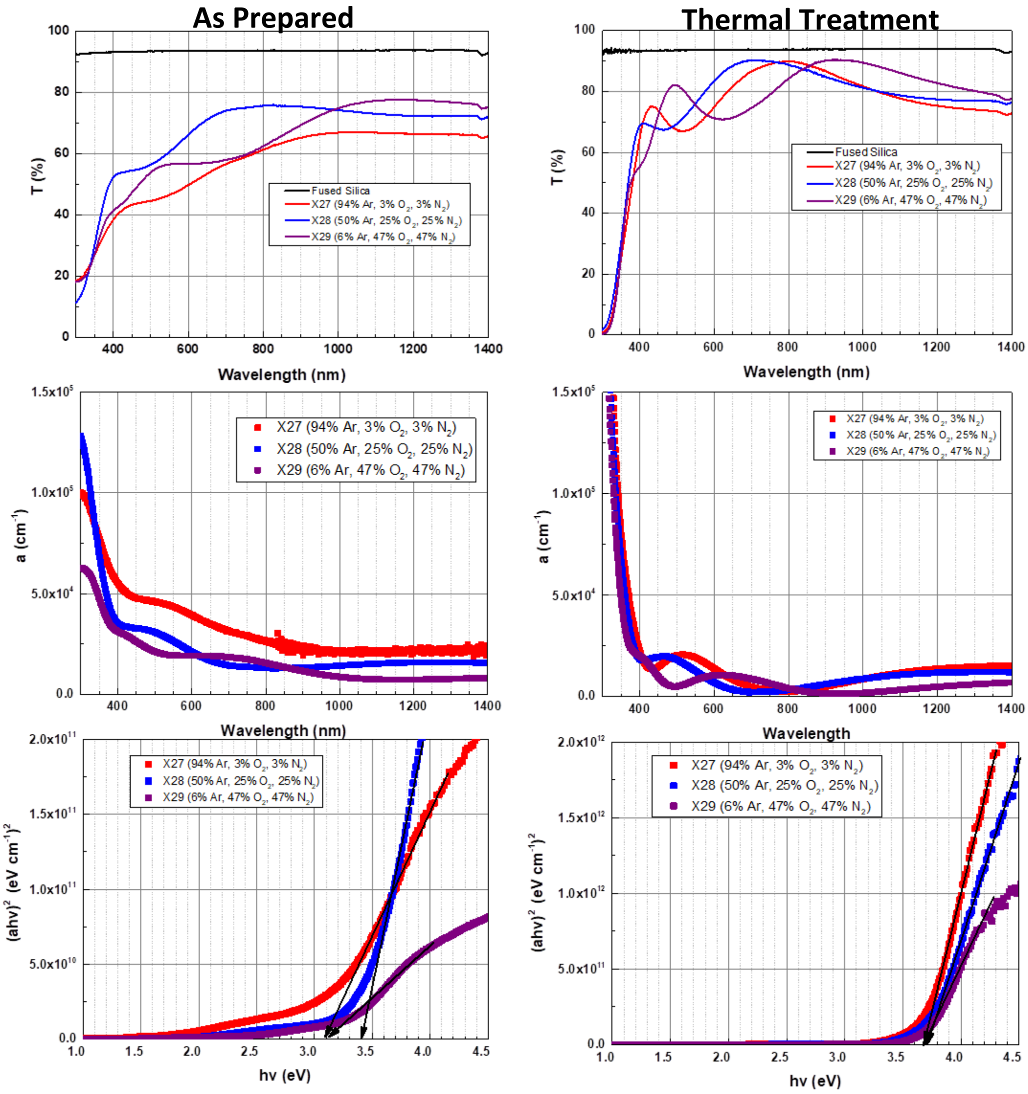

Fig. 6.30: Analysis of optical measurements

Table 21: Analysis of optical measurements

	T (%) (@550nm)	α (cm^{-1}) (@550nm)	E_{gap} (eV)
NiO:Nb-N	**X27 (94% Ar, 3% O_2 , 3% N_2 & 14Nb)**		
AS	46	43k	3.1
TT1	68	19k	3.7
NiO:Nb-N	**X28 (50% Ar, 25% O_2 & 25% N_2 & 14Nb)**		
AS	60	26k	3.4
TT1	76	13	3.7
NiO:Nb-N	**X29 (6% Ar, 47% O_2, 47% N_2 & 14Nb)**		
AS	56	18k	3.1
TT1	75	8k	3.7

6.5.4 Electrical Characterization

The following table 22 contains the analysis of electrical measurements of double doped NiO (NiO:Nb-N) samples. As seen with nitrogen introduction in samples, the resistivity was increased and after thermal treatment the resistivity of samples was impossible to be measured. It is known that as prepared stoichiometric NiO has huge resistivity and it is transparent. So, with introduction of nitrogen and after thermal treatment the disorders were decreased and samples became more stoichiometric, as a result the resistivity and energy gap increased. Hall measurements were impossible to be measured because of the high resistance.

Table 22: Analysis of electrical measurements

NiO	R (Ω)		ρ (Ω*cm)		Rsh (Ω/sq)	
	AS	**TT1**	**AS**	**TT1**	**AS**	**TT1**
X27	50M	-	252	-	15M	-
X28	>100M	-	13k	-	>100M	-
X29	>100M	-	17k	-	>100M	-
X30	>100M	-	3k	-	>100M	-
X31	>100M	>100M	21k	54k	>100M	>100M
X32	12k	>100M	0.05	18k	4k	>100M

To summarize, the as prepared double doped NiO samples (NiO:Nb-N) had lower transmittance than nitrogen doped NiO (NiO:N) but after thermal treatment was increased. Also the resistivity of as prepared samples was high and after thermal treatment was impossible to be measured.

6.6 Properties of TiO_2 Thin Films

The n-type TiO_2 thin films consist of two layers, namely a mesoporous TiO_2 layer (m-TiO_2) on top of a compact TiO_2 layer (c-TiO_2). Both of them were made by spin-coating on FTO/glass substrate. The n-type TiO_2 thin films were used for forming the heterojunction diodes with the p-type NiO.

The surface morphology, the structural and optical measurements of the m-TiO_2/c-TiO_2/FTO/glass configuration is seen in the following figures. The surface of the m-TiO_2 was rough, as seen in fig. 6.31, with root mean square (RMS) roughness of 20 nm, as deduced from atomic force microscopy measurements. As seen in fig. 6.32, the XRD measurements of TiO_2 layers was dominated by the peaks arising from the underneath FTO layer, whose crystallite size, as deduced for the peak at 37.8^o using the Scherer formula, was 21.7 nm. The diffraction peaks originating from TiO_2 had a very small intensity and were ascribed to the anatase phase (JCPDS card No: 01-071-1167) and the rutile phase (JCPDS card No: 01-076-0319). The transmittance of m-TiO_2/c-TiO_2/FTO/glass, and those of FTO/glass, is seen in fig.6.33. TiO_2 did not affect the optical properties of the FTO/glass. The visible transmittance of the m-TiO_2/c-TiO_2/FTO/glass was 75–85%. Also the absorption coefficient of m-TiO_2/c-TiO_2/FTO/glass is presented and its energy gap was 3.7eV.

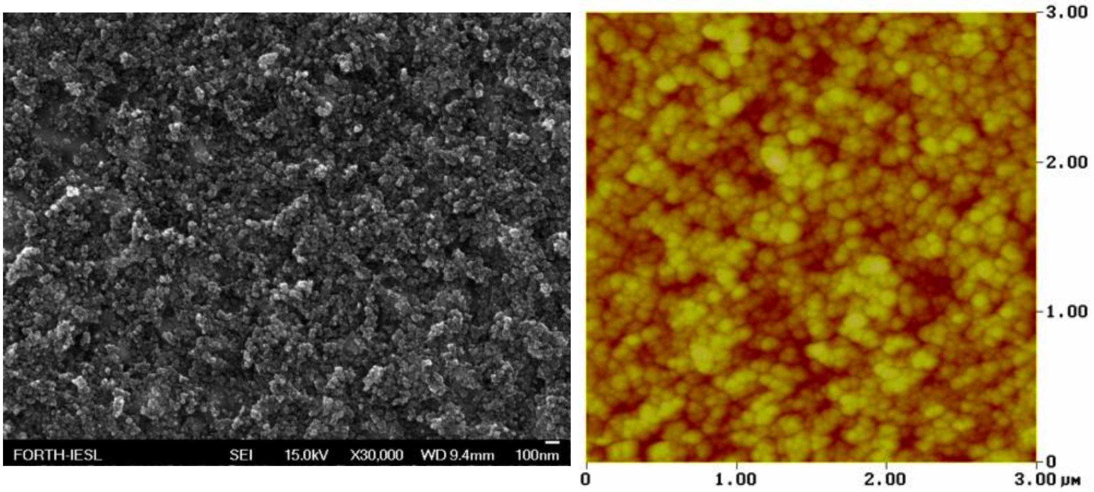

Fig 6.31: SEM and AFM photos of TiO_2

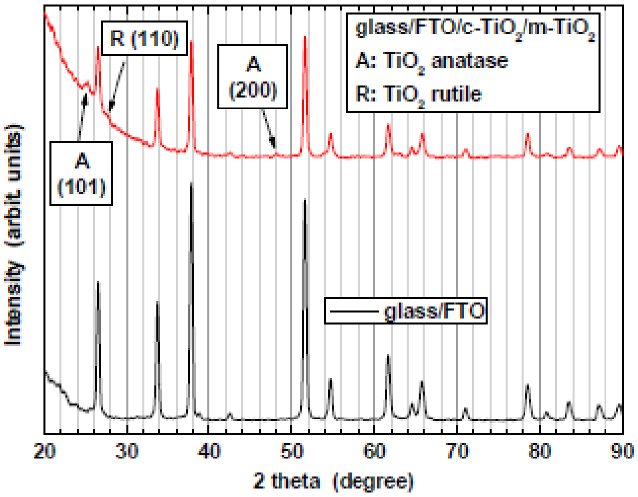

Fig. 6.32: XRD measurements

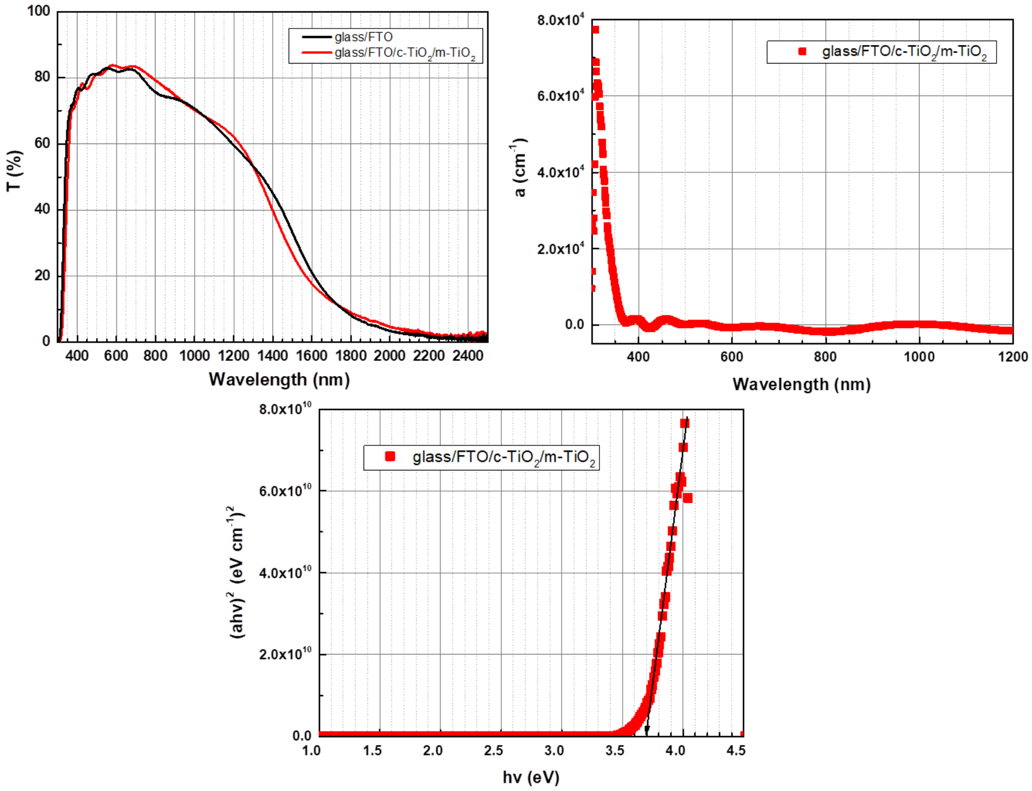

Fig. 6.33: Analysis of optical measurements

6.7 Characterization & Comparison of the p-NiO/n-TiO_2 Diodes

6.7.1 Characterization of films

The m-TiO_2/c-TiO_2/FTO/glass was used as substrate on which the undoped, doped or double doped NiO (NiO, NiO:N, NiO:Nb, NiO:Nb-N) were deposited in plasma. After the characterization of all NiO films the following films in table 23 were chosen for the fabrication of heterojunction diode. These films (X22c, X10c, NN2c & X28c) were chosen because they had optimum structural properties such as less lattice strain and optical properties such as higher optical transmittance. Moreover the X22c and X10c films had the lower resistivity than the other two films. NiO films were made at the same deposition run on different substrates with the heterojuntion diodes for a better characterization of films and diodes. For this reason the samples have the “c” next to their names.

Table 23: Information of deposition conditions

Samples	**Flow rates ratio (%)**			**Nb (pellets)**	**Deposition Time (min)**	**Thickness (nm)**	**Deposition Rate (nm/min)**	**at.% Nb**
	Ar	**O_2**	**N_2**					
X22c	50	50	0	0	95	125	1.32	0
X10c	50	50	0	14	105	175	1.67	1.7
NN2c	50	25	25	0	125	166	1.33	0
X28c	50	25	25	14	105	112	1.07	2.0

6.7.1.1 Surface Characterization

The following SEM photos (fig. 6.34) present the surface of NiO films which were used as p-type semiconductors in a heterojunctions diode. Nitrogen doped nickel oxide presented bigger grains size and niobium doped nickel oxide had smaller grains size. From AFM measurements (Fig. 6.35) differences in roughness were observed on the surface of samples. The nitrogen doped nickel oxide presented the biggest roughness but niobium doped nickel oxide presented the lower roughness, so the roughness depends on the dopants of samples as shown in the previous sections.

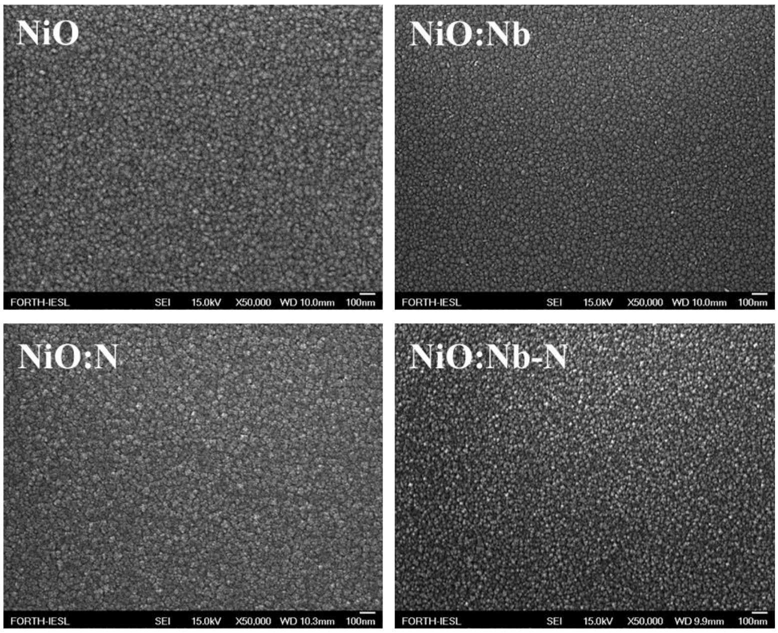

Fig 6.34: SEM photos of NiO samples

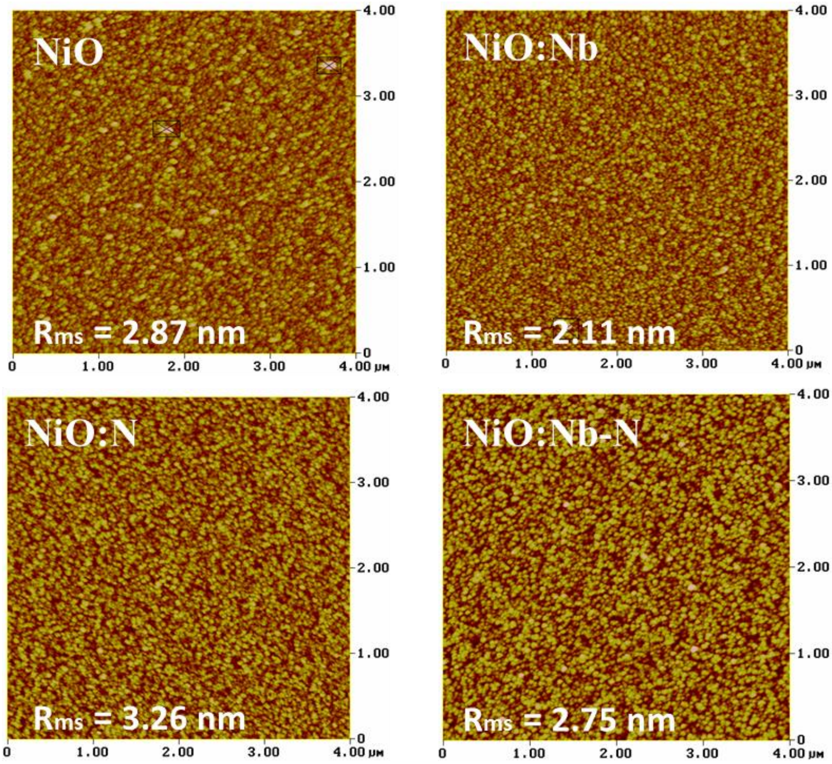

Fig 6.35: AFM photos of NiO samples

Also XPS measurements were made for these samples. The purpose of that measurement was the detection of nitrogen and niobium in the samples as well as a preliminary estimation of their percentages. In the fig. 6.36 all analysis of XPS measurements for every sample is presented. As seen, NiO sample has only the peaks of nickel and oxygen, niobium doped NiO (NiO:Nb) sample has peaks of nickel, oxygen and niobium, while nitrogen doped NiO

(NiO:N) has peaks of nickel, oxygen and nitrogen. Double doped NiO (NiO:Nb-N) has all peaks. All the other peaks in the survey graphs are secondary transitions of Ni and Si. After analyzing peaks of Ni, Nb, N and O of Fig. 6.36 as seen in table 24, niobium doped NiO had 1 at.% Nb, nitrogen doped NiO had 3% N, while double doped NiO had equal amount of nitrogen and niobium.

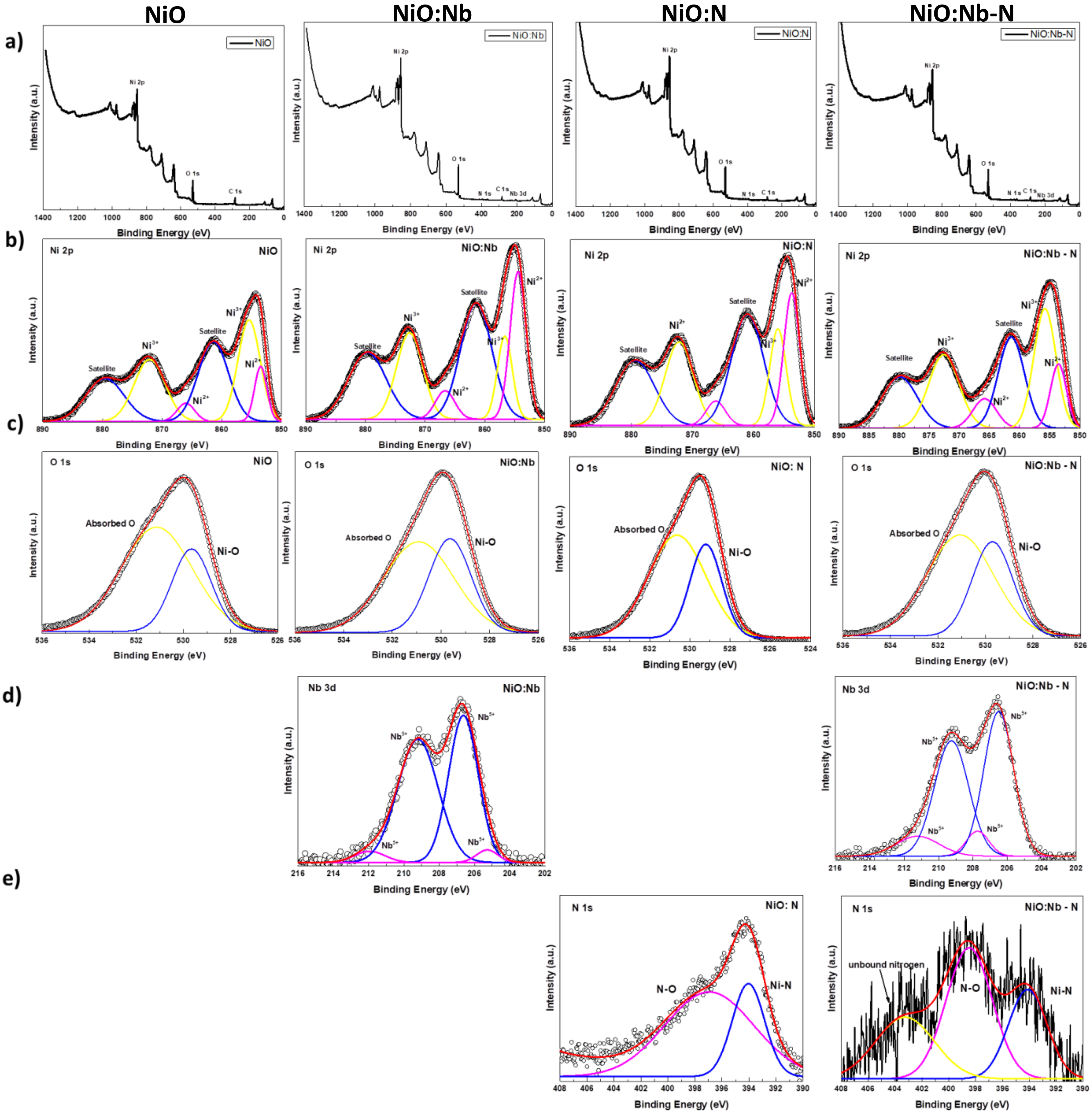

Fig 6.36: Analysis of XPS measurements

Table 24: Preliminary results of XPS

Samples	at. % Ni	at. % O	at. % N	at. % Nb
NiO	46.8	**53.2**	0	0
NiO:Nb	49.9	49.1	0	**1**
NiO:N	50.3	46.7	**3**	0
NiO:Nb-N	47.4	49	**1.8**	**1.8**

6.7.1.2 Structural Characterization

In the following graphs (fig. 6.37) XRD measurements of samples are presented. As seen, the undoped NiO, niobium doped NiO (NiO:Nb) and nitrogen doped NiO (NiO:N) films during growth did not affect its crystallographic cubic phase. The films presented single-phase NiO films with a preferred (200) crystallographic plane at ~43.29^{o} (JCPDS card No: 78-0429). The double doped NiO (NiO:Nb-N) also presented an extra peak at ∼38.20^{o}, which probably comes from Ni-Nb-O bonds (JCPDS card No: 31-0906). In the table 25 the analysis of XRD measurements are presented. The crystallite size of nitrogen doped NiO and double doped NiO was bigger because the ionic radius of nitrogen is bigger than niobium, oxygen and nickel atoms. Also in these samples a reduction of lattice strain was observed because with introduction of nitrogen in samples the disorders were reduced.

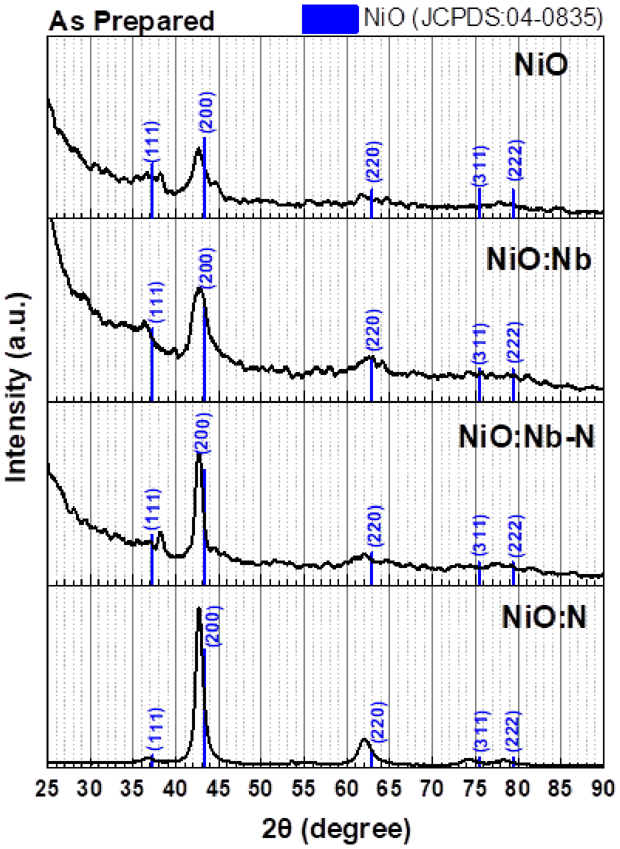

Fig. 6.37: XRD measurements

Table 25: Analysis of XRD measurements

	Peak Position (degree)	FWHM (degree)	Crystallite Size (nm)	Lattice Strain	Dislocation Density (nm^{-2})	Interplanar spacing (Å)	Lattice Constant (Å)
NiO (JCPDS: 04-0835)							
	43.29	-	-	-	-	2.0883	4.1766
X22c (50% Ar & 50% O_2)							
AS	42.56	1.58	5.33	0.0177	0.0352	2.1224	4.2448
X10c (50% Ar, 50% O_2 & 14Nb)							
AS	42.84	1.88	4.49	0.0209	0.04955	2.1092	4.2184
NN2c (50% Ar, 25% O_2, 25% N_2)							
AS	42.72	0.96	8.77	0.0107	0.0130	2.1148	4.2297
X28c (50% Ar, 25% O_2, 25% N_2 & 14Nb)							
AS	42.66	0.84	10.07	0.0094	0.0099	2.1177	4.2353

6.7.1.3 Optical Characterization

In the fig. 6.38 the transmittance, absorption coefficient and energy gap of samples are presented. From table 26 the results of optical measurements are summarized. As seen all as prepared samples, which did not have nitrogen gas in plasma (NiO, NiO:Nb), had low transmittance at 550nm but after thermal treatment at 300°C their transmittance was increased to 60%. The samples, which contain nitrogen gas in plasma, had higher transmittance and after thermal treatment it was increased more and reached almost at 85%. Moreover after thermal treatment the absorption coefficient was decreased one order of magnitude and the energy gaps of samples were almost the same. To summarize, the samples, which did not contain nitrogen, had structural disorder but after thermal treatment they were reduced. On the other hand the nitrogen doped NiO had less structural disorder due to the introduction only nitrogen, as a result the energy gap after thermal treatment did not change.

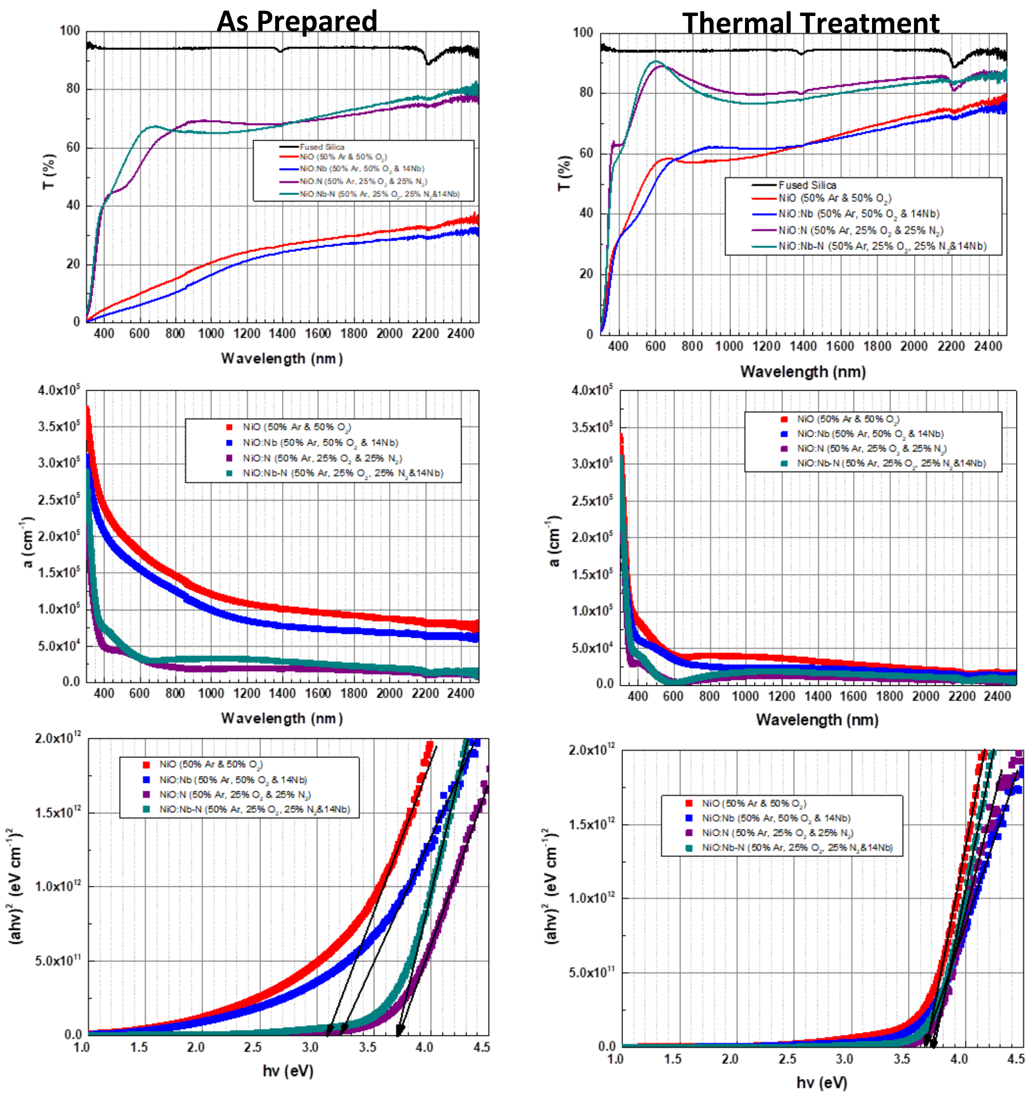

Fig. 6.38: Analysis of optical measurements

Table 26: Analysis of optical measurements

	T (%) (@350nm)	α (cm^{-1}) (@350nm)	E_{gap} (eV)
NiO	**X22c (50% Ar & 50% O_2)**		
AS	3	$2.8 \cdot 10^5$	3.1
TT1	22	$1.2 \cdot 10^5$	3.7
NiO:Nb	**X10c (50% Ar, 50% O_2 & 14Nb)**		
AS	2	$2.4 \cdot 10^5$	3.2
TT1	16	$1.0 \cdot 10^5$	3.7
NiO:N	**NN2c (50% Ar, 25% O_2 , 25% N_2)**		
AS	21	$9.0 \cdot 10^4$	3.7
TT1	51	$4.6 \cdot 10^4$	3.7
NiO:Nb-N	**X28c (50% Ar, 25% O_2, 25% N_2 & 14Nb)**		
AS	27	$1.1 \cdot 10^5$	3.7
TT1	43	$7.1 \cdot 10^4$	3.7

6.7.2 Characterization of diodes

In fig. 6.39 a schematic form of diode, which was made, is presented. As seen, it consisted of one layer of FTO on glass with FTO thickness ~600nm, one layer of c-TiO_2 with thickness 60nm, one layer of m-TiO_2 with thickness 200 nm and top of them there was a layer of NiO. The device was completed by Au ohmic contact on the NiO and FTO layers with thickness 150 nm.

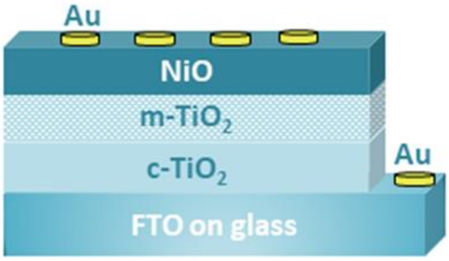

Fig. 6.39: Schematic form of diode

After the deposition of NiO (NiO, NiO:N, NiO:Nb, NiO:Nb-N) as p-type semiconductor on m-TiO_2/c-TiO_2/FTO/glass some devices were peeled off, especially the devices which did not consist nitrogen. The device, which consisted of niobium doped NiO (NiO:Nb), did not peeled off because it was baked at 300°C immediately after deposition. In the fig. 6.40 optical measurements of devices, which had NiO:N, NiO:Nb-N and NiO:Nb as p-type semiconductor, are presented before and after thermal treatment. As seen, the as prepared sample had optical transmittance almost 55% and after thermal treatment it was increased and it reached almost 60-80%. The device, which contains NiO:Nb, had the lower transmittance after thermal treatment because NiO:Nb was not so transparent as NiO:N and NiO:Nb-N.

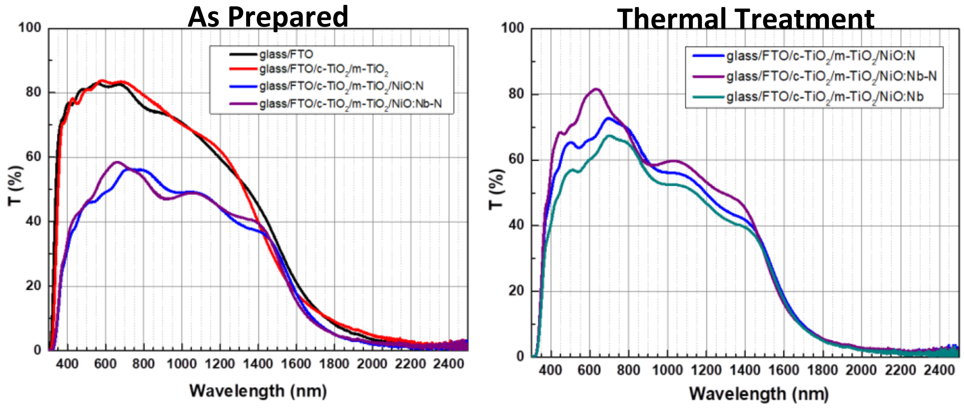

Fig. 6.40: Optical measurements of diodes

In fig. 6.41 the electrical measurements of diodes are presented before and after thermal treatment at 300°C. For analysis of electrical measurements two different methods were used (I-V method & Cheung method). The procedure of analysis for these methods is presented in Appendix 2. As seen in table 27, after thermal treatment the sheet resistance (R_s) was increased in all samples. The saturation current density (J_s) and ideality factor (n) of diode which contained nitrogen doped NiO (NN2) was decreased and barrier height (ϕ_B) was increased. On the other hand the saturation current density (J_s) and ideality factor (n) of diode which contained double doped NiO (X28c) was increased and barrier height (ϕ_B) was decreased.

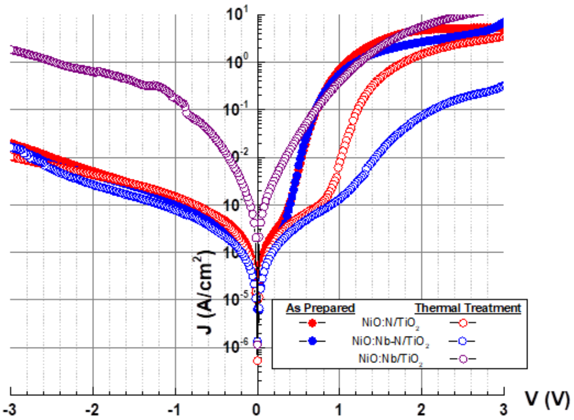

Fig. 6.41: Electrical measurements of diodes

Table 27: Analysis of electrical measurements of diodes

	J_s (A)		R_s (Ohm)		n		ϕ_b (eV)	
	I-V method	**Cheung method**	**I-V method**	**Cheung method**	**I-V method**	**Cheung method**	**I-V method**	**Cheung method**
	X10c (50% Ar, 50% O_2 & 14Nb)							
TT1	$1.8\cdot10^{-3}$	$2.4\cdot10^{-3}$	13	12	7.0	7.4	0.58	0.57
	NN2c (50% Ar, 25% O_2 , 25% N_2)							
AS	$3.8\cdot10^{-6}$	$1.6\cdot10^{-4}$	24	21	3.2	4	0.74	0.64
TT1	$3.8\cdot10^{-8}$	$1.5\cdot10^{-9}$	50	53	2.7	2.6	0.86	0.94
	X28c (50% Ar, 25% O_2, 25% N_2 & 14Nb)							
AS	$1.5\cdot10^{-6}$	$4.0\cdot10^{-8}$	49	50	2.3	1.6	076	0.86
TT1	$1.0\cdot10^{-5}$	$2.4\cdot10^{-2}$	351	398	8.2	7.0	0.71	0.51

All diodes have n>2 which imply that the transport mechanism is not dominated by thermionic emission but through recombination at defects states at interface. Also from the characterization of films, an increase of resistance after thermal treatment was observed, so after thermal treatment of diodes increase of resistance was also observed. Finally differences have been observed between two methods (I-V method & Cheung method). The differences might be attributed to the fact that Cheung's model takes into account the series resistance of the diode and is applied to the whole range of forward voltages, whereas the I–V method is applied for voltages where the linear part of the I–V curve starts, i.e., V > 3 kT/q = 0.78 V.

Finally a UV laser at 325nm was used and it illuminated diodes from their back side, as seen in fig. 6.42. These measurements were made after thermal treatment of diodes. From three diodes only two diodes gave UV photo response as seen in fig. 6.43. These devices consisted of niobium doped NiO (NiO:Nb) and double doped NiO (NiO:Nb-N) as p-type semiconductors. As seen from fig. 6.43 and table 28 the diode which has as p-type semiconductor the double doped NiO (NiO:Nb-N) had better output performance (V_{oc} = 0.5V and I_{sc} = 0.2 mA/cm^2)

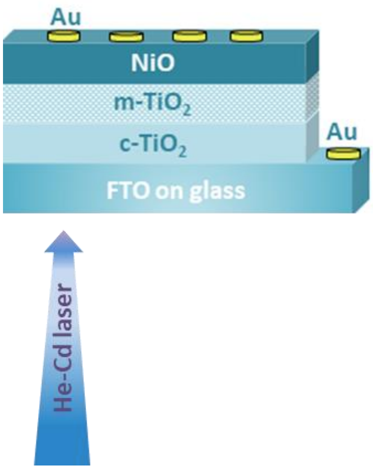

Fig. 6.42: Schematic form of UV measurements

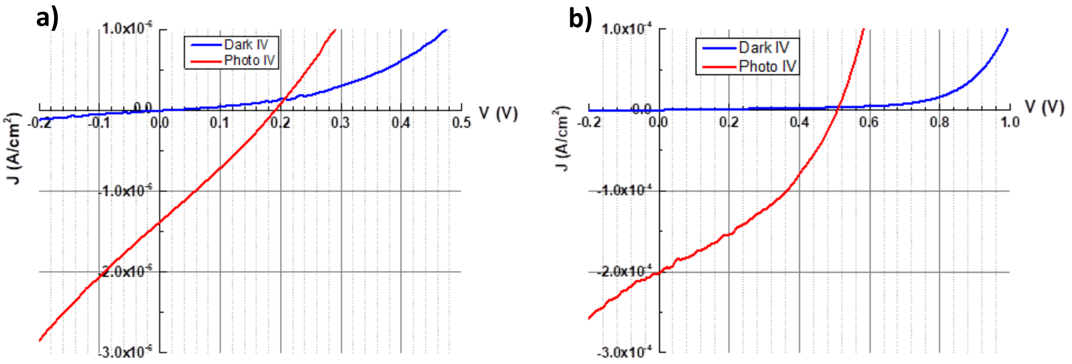

Fig. 6.43: photo UV measurements a) NiO:Nb/mTiO2/cTiO2/FTO/glass
b) NiO:Nb-N/mTiO2/cTiO2/FTO/glass

Table 28: Analysis of UV photo measurements of diodes

Diode	Voc (V)	Jsc (μA/cm^2)
NiO:Nb/m-TiO$_2$/c-TiO$_2$/FTO/glass	0.2	1.4
NiO:Nb-N/m-TiO$_2$/c-TiO$_2$/FTO/glass	0.5	200

Chapter 7 - *Conclusions*

In last years, the importance of transparent conducting oxide (TCO) thin films has increased enormously due to their potential applications in optoelectronic devices. Nevertheless most of TCOs are of n-type semiconductors and only a few TCOs are p-type semiconductors. As a result a scientific focus towards the development of new p-type TCOs is required. Nickel oxide (NiO) is one promising intrinsic p-type TCOs which exhibits several attractive features like wide energy band gap, excellent chemical stability and non-toxicity. Thanks to its chemical stability and non-toxicity, NiO has found numerous applications in photo-bio-catalysis, sensing, microbatteries and transparent optoelectronics like smart windows, ultra-violet (UV) photodetectors and photovoltaics (PVs). In the case of PVs, NiO has been employed in conventional PVs and ultra-violet UV-PVs, additionally to perovskite PVs, in which it is used as a hole transport layer.

Due to the technological importance of NiO material, plenty of attempts have been made to change its properties depending on the application. Some dopants which have been used are: Al, Li, Cu, Nb, N, also co-doping has been reported, like Li-Al, Li-Mg and Cu-N. As in the case where low-temperature depositions are performed, it is generally agreed that different dopants can result in different structural distortions which in turn have significant effects on the electronic structure, defect levels and, consequently, on the properties of the material.

The purpose of this master thesis was the fabrication of undoped NiO as well as doped NiO with dopants nitrogen (N), niobium (Nb), and co-doping (Nb-N) for modifying its properties. All films were made by the rf sputtering technique at room temperature at 5mTorr. The characterization of films concerned their morphology (SEM, AFM), structural (XRD), electronic (EDX & XPS), optical (UV-VIS) and electrical (I-V, Seebeck & Hall Effect) properties. After the characterization of films, the optimum ones, just after fabrication at 300^oC in N_2 or after thermal treatment, were chosen for fabrication of heterodiodes which consisted of NiO as p-type semiconductor and TiO_2 as n-type semiconductor. These diodes were characterized in the dark and under UV illumination.

Firstly, three different undoped NiO samples (X22, X23 & X24) were made in different deposition conditions (gases in plasma and power) in order to observe the differences of their properties. The plasma gases for the X22 film were $Ar:O_2 = 50:50$ and power at 300 W. For the X23 film the same deposition conditions were used but the power was at 400 W. Moreover the plasma gases for the X24 film were $Ar:O_2 = 95:5$ and power at 300 W. The X24 sample had the biggest roughness because of the higher Ar amount and deposition rate. A difference in roughness between X22 and X23 samples was also observed because of the different power used during deposition. XRD revealed that films were polycrystalline having single phase cubic NiO structure, whereas EDX showed that the films were O-rich (O:Ni=1.36). After thermal treatment the diffraction peaks were shifted to higher angles and the lattice strain was decreased. This indicated that the structural disorder of the undoped NiO was decreased. Moreover the optical transmittance of the as prepared undoped NiO samples was low but after thermal treatment an increase was observed. Seebeck measurements were used for proof of the p-type of NiO. In addition, Hall measurements showed that the as prepared NiO is indeed a p-type semiconductor with carrier concentration $\sim 2 \cdot 10^{19}$ cm^{-3} and mobility 0.77 cm^2/Vs.

Afterwards nitrogen (N) doped NiO (NiO:N) films were made in different flow rates of O_2 and N_2 gases in Ar plasma (containing 50% Ar and 50% O_2+N2), at 300W in order to observe the differences of NiO properties. With the introduction of nitrogen in plasma the deposition rate was reduced because nitrogen atoms are lighter than the oxygen atoms. However, when compared to the surface morphology of undoped NiO, the N-containing films have a rougher surface with a bigger grain size. Moreover, the introduction of nitrogen in the structure of NiO films during growth did not affect its crystallographic cubic phase. The films remained single-phase NiO films with a preferred (200) crystallographic plane at ~43.29^o and with no evidence of any other nickel oxide or nitride phases (Ni_2O_3, NixNy, etc.). The optical transmittance of as prepared nitrogen doped NiO films was increased from ~10% to ~50% and after thermal treatment the transmittance was reached to ~85%. However, with the introduction of nitrogen the resistivity was increased by four orders of magnitude. It is known that as prepared stoichiometric NiO has high resistivity and it is generally transparent. So with the introduction of nitrogen the structural disorder was decreased and the samples became more stoichiometric and as a result the resistivity and energy gap increased.

In the next step, different numbers of Nb pellets were used on the nickel target with the purpose of introducing Nb in Ni-O structure and detect it by EDX measurements and observation the changes in the properties of samples with different amount of Nb in Ni-O. Nb-doped NiO had less rough surface than undoped NiO. In XRD measurements Nb-doped NiO (NiO:Nb) presented a preferred (200) crystallographic plane at ~43.29^o but another peak was appeared at around 38.30^o, which was very intense after thermal treatment. That peak probably may be due to Ni-Nb-O bond ($NiNb_2O_2$). In the Nb-doped NiO samples, which were made at 300W, the crystallite size was reduced and the lattice strain was increased when compared to the respective properties of the undoped NiO. On the other hand, in the Nb-doped NiO samples, which were made at 400W, the crystallite size was increased and the lattice strain was decreased when compared to the respective properties of the undoped NiO. EDX experiments revealed that the atomic percentage of Nb in Ni-O was never more than 2.5% in $Ar:O_2$=50:50 reaching 4% in Ar-rich plasma. As prepared Nb-doped NiO samples had low transmittance but after thermal treatment their transmittance and energy gap were increased. Also after thermal treatment the resistivity was increased four orders of magnitude. With thermal treatment the structural disorder of samples was reduced and the samples became more stoichiometric. So, Nb does not affect the optical and electrical properties of as prepared samples and they change only after thermal treatment. Hall measurements for Nb-doped NiO were unreliable. Seebeck measurements confirmed the p-type conduction of Nb-doped NiO.

Moreover the influence of different Nb pellets' positions on nickel target as well as different plasma conditions on NiO properties was examined. Two different conditions of plasma were examined. The first was 50% Ar & 50% O_2 at 300W, while the second was 95% Ar & 5% O_2 at 300W. The higher content of Ar in plasma (95%) increased the deposition rate and grains size was bigger than samples which had 50% Ar in plasma respectively. Also these samples had bigger roughness because the plasma was more energetic. Later, the influence of Ar on properties of niobium doped NiO was examined. One sample was fabricated in plasma which contained higher content of Ar and another one contained less content of Ar (5%). Fourteen Nb pellets were placed and uniformly distributed on the nickel target covering roughly the 75% of target surface and during deposition the power was 300W. When a sample had higher content of Ar in plasma during deposition it had rougher surface. While the sample with oxygen rich plasma had lower transmittance, higher absorption coefficient and low energy gap but its resistivity is lower than the samples with higher content of Ar in plasma. Finally the influence of the samples' thickness in the surface was examined. There were ten Nb pellets on the nickel target and the power was at 300W. The thick films had bigger grain size and as the content of nitrogen gas increased in the plasma as the grains were increased.

Double doped NiO films with dopants niobium and nitrogen (NiO:Nb-N) were made in different percentages gases in plasma for the investigation of their properties. Fourteen Nb pellets were used and the power of deposition was at 300W. These conditions were selected because the detection of Nb in Ni-O structure from EDX experiments with 14Nb on nickel target resulted in 2at.% Nb in NiO and the power of 300W does not create deep intrusions of sample surface. The films presented a preferred (200) crystallographic plane at ~43.29° and the X28 and X29 samples also presented an extra peak at ∼38.30°, which could probably from Nb-Ni-O phase and requires further investigation. As prepared double doped NiO samples (NiO:Nb-N) had lower transmittance than nitrogen doped NiO (NiO:N) but after thermal treatment was increased. Also the resistivity of as prepared sample was high and increase further after thermal treatment.

For the fabrication of p-NiO/ n-TiO_2, the n-TiO_2 was fabricated by spin coating in a chemistry lab. The n-type TiO_2 thin films consist of two layers, namely a mesoporous TiO_2 layer (m-TiO_2) on top of a compact TiO_2 layer (c-TiO_2). Both of them were made by spin-coating on FTO/glass substrate. The n-type TiO_2 thin films were used for forming the heterojunction diodes with the p-type NiO. The surface of the m-TiO_2 was rough with root mean square (RMS) roughness of 20 nm. The XRD measurements of TiO_2 layers was dominated by the peaks arising from the underneath FTO layer and the diffraction peaks originating from TiO_2 had a very small intensity and were ascribed to the anatase phase and the rutile phase. The visible transmittance of the m-TiO_2/c-TiO_2/FTO/glass was 75–85% from which the energy gap of m-TiO_2/c-TiO_2 was calculated to be 3.7eV.

Finally m-TiO_2/c-TiO_2/FTO/glass was used as substrate on which the undoped, doped or double doped NiO (NiO, NiO:N, NiO:Nb, NiO:Nb-N) were deposited in plasma. These films (X22c, X10c, NN2c & X28c) were chosen because they had optimum structural properties such as less lattice strain and optical properties such as higher optical transmittance. XPS measurements were made for these samples and it showed that Nb-doped NiO had 1 at.% Nb, N-doped NiO had 3% N, while double doped NiO had equal amount of nitrogen and niobium. After the deposition of NiO (NiO, NiO:N, NiO:Nb, NiO:Nb-N) as p-type semiconductor on m-TiO_2/c-TiO_2/FTO/glass, the device having undoped NiO peeled off. The as prepared sample had optical transmittance almost 55% and after thermal treatment it was increased and it reached almost 60-80%. The device, which contains NiO:Nb, had the lower transmittance after thermal treatment because NiO:Nb was not so transparent as NiO:N and NiO:Nb-N.

Moreover after thermal treatment the sheet resistance (R_s) was increased for all NiO/TiO_2. The saturation current density (J_s) and ideality factor (n) of diode which contained N-doped NiO (NN2) was decreased and barrier height (ϕ_B) was increased. On the other hand the saturation current density (J_s) and ideality factor (n) of diode which contained double doped NiO (X28c) was increased and barrier height (ϕ_B) was decreased. Finally a UV laser at 325nm was used and it illuminated diodes from their back side. These measurements were made after thermal treatment of diodes. From three diodes only two diodes gave UV photo response. These devices consisted of Nb-doped NiO (NiO:Nb) and double doped NiO (NiO:Nb-N) as p-type semiconductors. The diode which has as p-type semiconductor the double doped NiO (NiO:Nb-N) had better output performance (V_{oc} = 0.5V and I_{sc} = 0.2

mA/cm^2). More experiments are required to understand the behavior at the heterostructures and improve further the dark and illuminated properties.

Appendix 1

Proof of absorption coefficient and refractive index equations

- **Proof of equation** $\boldsymbol{\alpha_1 = \frac{1}{d}\ln\left(\frac{(1-R)^2+\sqrt{(1-R)^4+4R^2T^2}}{2T}\right)}$

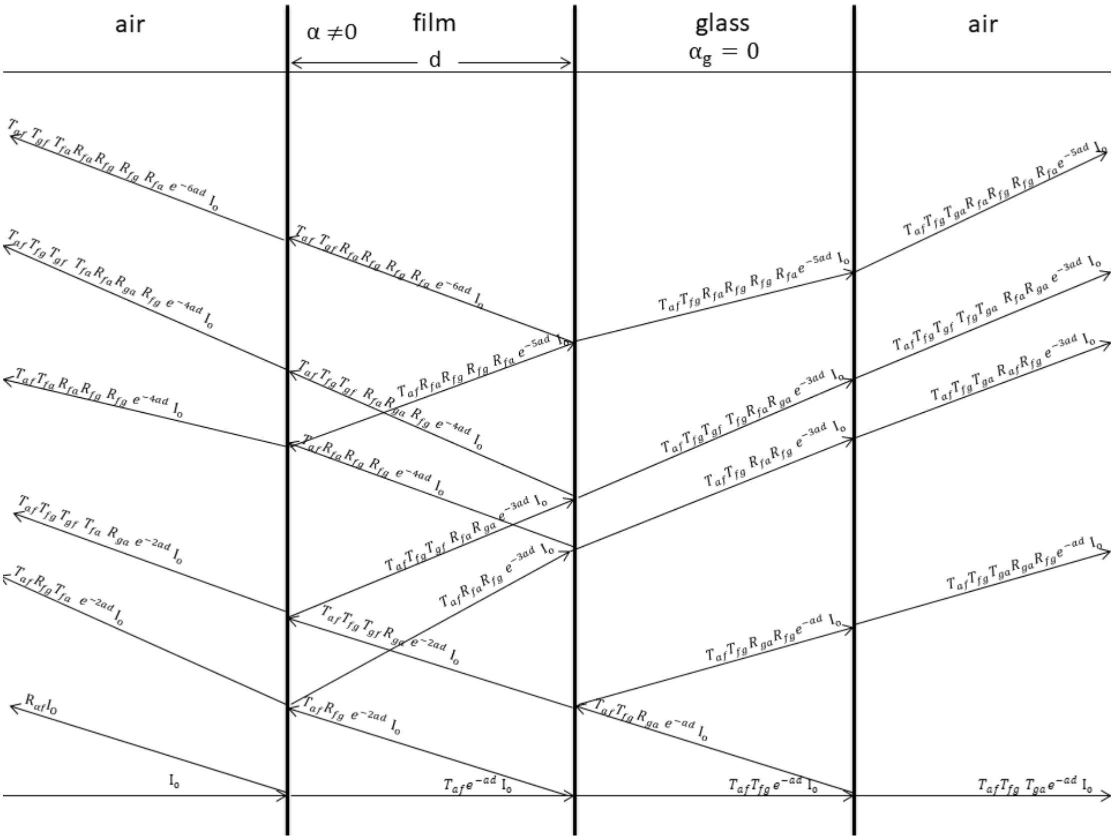

When a beam of light hits the sample, a percentage of light will be reflected, a percentage will be absorbed and a percentage will penetrate the sample. Suppose a sample consists of two layers, the first is the film having thickness d and absorption coefficient α, and the second is substrate (glass). Also there is air before film and after substrate. As assumed that the initial intensity of light is I_o. When it hits film, the radiation which will penetrate and arrive the next layer is $I_T=T_{af}e^{-\alpha d}I_o$, while the radiation, which will be reflected is $I_R=R_{af}I_o$. The term T_{af} is the percentage of transmittance, which passes through air-film interface, and R_{af} is the percentage of reflectance which is reflected back at the air-film interface. Moreover, when the beam is passed through a film, there is absorption. The absorption is indicated by the term $e^{-\alpha d}$, where α is absorption coefficient and d is the thickness of layer.

Each material is defined by a complex refractive index (N), which is given by the relation[62][63]:

$$N = n - ik$$

Where n is the refractive index and k is the absorption index of material.

The k is given from equation: $k = \frac{\alpha\lambda}{4\pi}$

where λ is wavelength of radiation.

The reflectance from a material, which has refractive index n_l, to another material, which has refractive index n_m, is given by Fresnel relation [63]:

$$R_{lm} = \frac{(N_l - N_m)^2}{(N_l + N_m)^2} = \frac{(n_l - n_m)^2 + (k_l - k_m)^2}{(n_l + n_m)^2 + (k_l + k_m)^2}$$

where N_l and N_m are complex refractive indices for materials l and m respectively.

The transmittance from a material is given by: $T_{lm} = 1 - R_{lm}$

Firstly the geometry air/film/glass is only examined and based on the above the reflectance and transmittance is given [63]:

$$R_{afg} = R_{af} + R_{fg}T_{af}T_{fa}x^2 + T_{af}T_{fa}R_{fg}^2R_{fa}x^4 + \cdots =$$

$$= R_{af} + R_{fg}T_{af}T_{fa}\left(x^2 + R_{fg}R_{fa}\ x^4 + \cdots\right) =$$

$$= R_{af} + R_{fg}T_{af}T_{fa}\sum_{\rho=1}^{\infty} x^{2\rho}\left(R_{fg}R_{fa}\right)^{\rho-1} =$$

$$= R_{af} + \frac{T_{af}R_{fg}T_{fa}x^2}{1 - R_{fg}R_{fa}x^2} = R_{af} + \frac{(1 - R_{af})R_{fg}(1 - R_{fa})x^2}{1 - R_{fg}R_{fa}x^2} =$$

$$= \frac{R_{af} - R_{fg}R_{af}R_{fa}x^2 + (R_{fs} - R_{fs}R_{af})(1 - R_{fa})x^2}{1 - R_{fg}R_{fa}x^2} = \frac{R_{af} - 2R_{af}R_{fg}x^2 + R_{fg}x^2}{1 - R_{fg}R_{fa}x^2} \qquad (1)$$

$$T_{afg} = T_{af}T_{fg}\,x + T_{af}T_{fg}R_{fg}R_{fa}x^3 + \cdots =$$

$$= T_{af}T_{fg}\sum_{\rho=1}^{\infty} x^{2\rho-1}\left(R_{fg}R_{fa}\right)^{\rho-1} =$$

$$= \frac{T_{af}T_{fg}x}{1 - R_{fg}R_{fa}x^2} =$$

$$= \frac{(1-R_{af})(1-R_{fg})x}{1-R_{fg}R_{fa}x^2} \qquad (2)$$

where x is equal to $e^{-\alpha d}$, R_{afg} is the percentage of total reflectance from the geometry air/film/glass, R_{af} is the percentage of reflectance which is reflected back at the air-film interface and R_{fg} is the percentage of reflectance which is reflected back at the film-glass interface.

The rest relations are calculated by the same procedure

$$R_{gfa} = R_{gf} + \frac{T_{gf}R_{fa}T_{fg}x^2}{1- R_{fa}R_{fs}x^2} = \frac{R_{fg} - 2R_{af}R_{fg}x^2 + R_{af}x^2}{1- R_{af}R_{fg}x^2}$$

$$T_{gfa} = \frac{T_{gf}T_{fa}x}{1-R_{fa}R_{fg}x^2}$$

Following the same procedure for geometry air/film/glass/air, the reflectance and transmittance is given [63]:

$$R_{afga} = R_{afg} + \frac{R_{ga}{T_{afg}}^2}{1-R_{ga}R_{gfa}} \qquad (3)$$

$$T_{afga} = \frac{T_{ga}T_{afg}}{1- R_{ga}R_{gfa}} \qquad (4)$$

Substituting in equations (3) and (4) the relations (1) and (2), the equations (3) and (4) become:

$$(3) \overset{(1)}{\Rightarrow} R_{afga} = R_{afg} + \frac{R_{ga}\left[\frac{(1-R_{af})(1-R_{fg})x}{1- R_{fg}R_{fa}x^2}\right]^2}{1-R_{ga}\left[\frac{R_{fg} - 2R_{af}R_{fg}x^2 + R_{af}x^2}{1- R_{af}R_{fg}x^2}\right]}$$

$$= R_{afg} + \frac{R_{ga}(1- R_{af})^2(1-R_{fg})^2x^2}{(1-R_{fg}R_{fa}x^2)[(1-R_{fg}R_{ga})-(R_{af}R_{fg}+R_{af}R_{ga}-2R_{af}R_{fg}R_{ga})x^2]}$$

$$= \frac{R_{af} - 2R_{af}R_{fg}x^2 + R_{fg}x^2}{1- R_{fg}R_{fa}x^2} + \frac{R_{ga}(1- R_{af})^2(1-R_{fg})^2x^2}{(1-R_{fg}R_{fa}x^2)[(1-R_{fg}R_{ga})-(R_{af}R_{fg}+R_{af}R_{ga}-2R_{af}R_{fg}R_{ga})x^2]}$$

$$= \left[\frac{R_{af} + R_{fg}(1-2R_{af})x^2}{1- R_{fg}R_{fa}x^2}\right] + \left[\frac{R_{ga}}{(1- R_{ga})^2(1-R_{fg}R_{fa}x^2)}\right] \cdot \left[\frac{(1- R_{af})^2(1-R_{fg})^2(1- R_{ga})^2x^2}{(1-R_{fg}R_{ga})-(R_{af}R_{fg}+R_{af}R_{ga}-2R_{af}R_{fg}R_{ga})x^2}\right] \qquad (3')$$

Setting $M = (1- R_{af})(1 - R_{fg})(1- R_{ga})$
$U = (1 - R_{fg}R_{ga})$
$W = R_{af}R_{fg} + R_{af}R_{ga} - 2R_{af}R_{fg}R_{ga}$

$$(3') \Rightarrow \boxed{R_{afga} = \left[\frac{R_{af} + R_{fg}(1-2R_{af})x^2}{1 - R_{fg}R_{fa}x^2}\right] + \left[\frac{R_{ga}}{(1-R_{ga})^2(1-R_{fg}R_{fa}x^2)}\right] \cdot \left[\frac{M^2x^2}{U-Wx^2}\right]}$$

$$(4) \overset{(2)}{\Rightarrow} T_{afga} = \frac{T_{ga}T_{afg}}{1-R_{ga}R_{gfa}} = \frac{\frac{(1-R_{ga})(1-R_{af})(1-R_{fg})x}{1-R_{fg}R_{fa}x^2}}{1-R_{ga}\frac{R_{fg}-2R_{af}R_{fg}x^2+R_{af}x^2}{1-R_{af}R_{fg}x^2}}$$

$$= \frac{(1-R_{ga})(1-R_{af})(1-R_{fg})x}{(1-R_{af}R_{fg}x^2)-(R_{ga}R_{fg}-2R_{ga}R_{af}R_{fg}x^2+R_{ga}R_{af}x^2)}$$

$$= \frac{(1-R_{ga})(1-R_{af})(1-R_{fg})x}{(1-R_{ga}R_{fg})-(R_{af}R_{fg}+R_{ga}R_{af}-2R_{ga}R_{af}R_{fg})x^2}$$

So, $\boxed{T_{afga} = \frac{M}{U-Wx^2}}$ (4′)

If the following conditions apply:

A) The reflectivity of the back surface of substrate (glass) is equal to zero (R_{ga}=0).

B) The reflectivity on the two surfaces of the film is the same ($R_{af} = R_{fg} = R$).

Then equation (4′) is:

$$T = \frac{(1-R)(1-R)}{1-R^2x^2} = \frac{(1-R)^2x}{1-R^2x^2} = \frac{(1-R)^2e^{-\alpha d}}{1-R^2e^{-2\alpha d}} \qquad (4'')$$

Solving the equation (4′′) for a:

$$(4'') \Rightarrow T\cdot(1-R^2e^{-2\alpha d}) = (1-R)^2e^{-\alpha d}$$

$$\Rightarrow R^2Te^{-2\alpha d} + (1-R)^2e^{-\alpha d} - T = 0$$

$$\xRightarrow{\cdot e^{2\alpha d}} R^2T + (1-R)^2e^{\alpha d} - Te^{2\alpha d} = 0$$

$$\Rightarrow -Te^{2\alpha d} + (1-R)^2e^{\alpha d} + R^2T = 0$$

Setting $x = e^{\alpha d}$

$$\Rightarrow Tx^2 - (1-R)^2x - R^2T = 0$$

$$x = \frac{(1-R)^2 \pm\sqrt{(1-R)^4 + 4R^2T^2}}{2T}$$

$$\Rightarrow e^{\alpha d} = \frac{(1-R)^2 \pm\sqrt{(1-R)^4 + 4R^2T^2}}{2T}$$

$$\Rightarrow \alpha d = \ln\left(\frac{(1-R)^2 \pm\sqrt{(1-R)^4 + 4R^2T^2}}{2T}\right)$$

$$\Rightarrow \alpha_{1,2} = \frac{1}{d} \ln\left(\frac{(1-R)^2 \pm\sqrt{(1-R)^4 + 4R^2T^2}}{2T}\right)$$

There are two solutions:

$\alpha_1 = \frac{1}{d} \ln\left(\frac{(1-R)^2+\sqrt{(1-R)^4 + 4R^2T^2}}{2T}\right)$ and $\alpha_2 = \frac{1}{d} \ln\left(\frac{(1-R)^2-\sqrt{(1-R)^4 + 4R^2T^2}}{2T}\right)$

The acceptable solution is: $\boxed{\alpha_1 = \frac{1}{d} \ln\left(\frac{(1-R)^2+\sqrt{(1-R)^4 + 4R^2T^2}}{2T}\right)}$

Because the absorption coefficient must be positive, the numerator in logarithm must be greater than the denominator.

Appendix 2
Determination of diode characteristics

1. Current-voltage (I-V) method

In the case of the Schottky diode, assuming that the current is due to a thermionic emission (TE) and neglecting the diode's resistance (R_S=0), the relation between the applied forward bias and the current can be given by[64][65][66][60]:

$$I = I_s \exp\left(\frac{qV_d}{nkT}\right)\left[1 - \exp\left(\frac{-qV_d}{nkT}\right)\right]$$

$$\Rightarrow \boxed{I = I_s\left[\exp\left(\frac{qV_d}{nkT}\right) - 1\right]}$$

where I_s: Saturation current

n: Ideality factor

T: Temperature in Kelvin (K),

q: electron charge (1.602×10^{-19} C),

k: Boltzmann constant ($1.38\text{x}10^{-23}$ J/K $=8.62\times10^{-5}$eV/K)

The term $V_{th} = \frac{kT}{q}$ is called thermal voltage and V_{th} = 25.86mV at 300K.

- For $V_d > 3kT/q$ =77.58meV ~0.1V we have:

$$I = I_s \exp\left(\frac{qV_d}{nkT}\right)$$

If $R_S \neq 0$ then from Fig. 2.1 IR_s is the voltage drops across the series resistance of the diode and

$$V = V_d + IR_s \Rightarrow V_d = V - IR_S$$

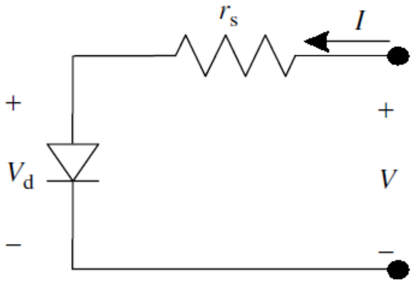

Fig. 2.1: Equivalent circuit of a diode

$$\text{So } \boxed{I = I_s \exp\left(\frac{q(V - IR_S)}{nkT}\right)} \quad (1)$$

For R_S=0, Eq. (1) becomes:

$$\boxed{I = Is \exp\left(\frac{qV}{nkT}\right)} \quad (2)$$

where: V and I are the measured values of voltage and current.

The Eq.(2) becomes:

$$\ln I = \ln I_s + \frac{qV}{nkT}$$

From the linear region of graph $\ln I$–V, ideality factor (n) can be calculated from the slope and I_s from the intercept [64] :

$$\text{Slope} = \frac{q}{nkT} \Rightarrow \boxed{n = \frac{q}{kT} \cdot \frac{1}{\text{slope}}}$$

$$\text{Intercept} = \ln I_s$$

$$\Rightarrow \boxed{I_s = \exp(\text{intercept})}$$

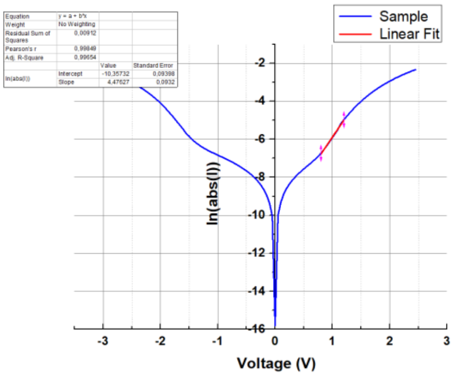

Fig. 2.2: Graph of ln(I) vs V

Calculation of sheet resistance (R_S)

On the linear region of graph $\ln I$ - V, at forward bias, we draw a straight line at the linear region (Fig. 2.3). For a specific value of lnI (I_O), we have two values of V. One voltage (V_{theor}) is on the straight line which we have drawn (theoretical) and the other one (V_{exp}) is on the experimental curve of the graph lnI-V, both for the same value of lnI. In this way, we can calculate the sheet resistance of diode from the relation:

$$R_S = \frac{\Delta V}{I_O} = \frac{V_{exp} - V_{theor}}{I_O}$$

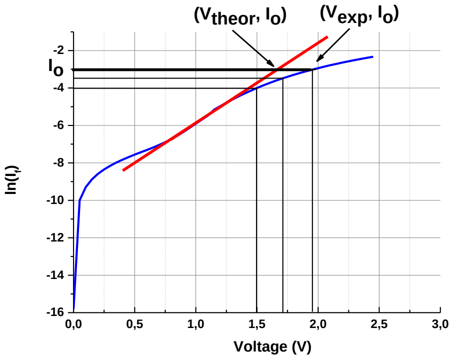

Fig. 2.3: Calculation of sheet resistance

Also we can calculate R_s when we draw three (or more) different lines for three (or more) values of lnI. In this way we have three (or more) values of I_o and three (or more) values of ΔV. From the graph I – ΔV we can calculate the sheet resistance from the slope:

$$\text{slope} = \frac{I}{\Delta V} = \frac{1}{R_S} \Rightarrow \boxed{R_S = \frac{1}{\text{slope}}}$$

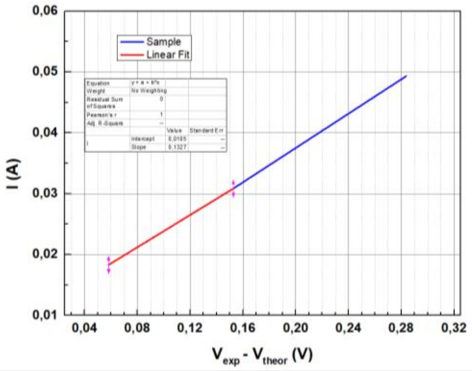

Fig. 2.4: Graph of I vs ΔV

Calculation of barrier height

The saturation current is given by the relation:

$$I_s = AA^*T^2\exp(\frac{-q\Phi_b}{kT}) \quad (3)$$

where A : diode area

A^* : Richardson constant

T : temperature in Kelvin (k)

$V_{th} = \frac{k_B T}{q}$: thermal voltage

Φ_b : barrier height

From equation (3) we have:

$$\boxed{\Phi_b = \frac{kT}{q}\ln\frac{AA^*T^2}{I_s}} \quad (4)$$

The Richardson constant is equal to[65][67][68]:

$$A^* = 4\pi q\frac{k^2m^*}{h^3} = 120\ (A/cm^2K^2)$$

Where k : Boltzman constant

q: electron charge ($1,602\times10^{-19}$ C)

m^* : Electron effective mass (9.11×10^{-31} kg)

h: Plank constant (6.63×10^{-34} m^2 kg/s).

2. Cheung method

In this method we use the same equation (Eq.(1)) as the first method and since $e^{(a+b)}=e^ae^b$ we have[65][67][69]:

Eq.(1): $I = I_s\exp\left[\frac{q(V-IR_S)}{nkT}\right] \Rightarrow I = I_s\exp\left(\frac{qV}{nkT}\right)\cdot\exp\left(-\frac{qIR_S}{nkT}\right)$

Since ln(ab)=lna + lnb and $\ln(a)^b$=blna the above equation becomes:

$$\Rightarrow \ln I = \ln I_s + \ln\left[\exp\left(\frac{qV}{nkT}\right)\right] + \ln\left[\exp\left(-\frac{qIR_S}{nkT}\right)\right]$$

Using Eq.(3) and since $x=\ln(e^x)=e^{\ln(x)}$ the above equation can be written as:

$$\Rightarrow \ln I = \ln\left[AA^*T^2\exp(\frac{-q\Phi_b}{kT})\right] + \frac{qV}{nkT} - \exp\left[\ln\left(\frac{qIR_S}{nkT}\right)\right]$$

Since $e^{\ln(ax)}=e^{(\ln a+\ln x)}=e^{\ln a}e^{\ln x}=ae^{\ln x}$ the above equation becomes:

$$\Rightarrow \ln I = \ln(AA^{*}T^{2}) + \ln\left[\exp(\frac{-q\Phi_b}{kT})\right] + \frac{qV}{nkT} - \frac{qR_s}{nkT}\exp[\ln(I)]$$

$$\Rightarrow \ln I = \ln(AA^{*}T^{2}) - \frac{q\Phi_b}{kT} + \frac{qV}{nkT} - \frac{qR_s}{nkT}\exp[\ln(I)]$$

$$\Rightarrow \frac{qV}{nkT} = \ln I - \ln(AA^{*}T^{2}) + \frac{q\Phi_b}{kT} + \frac{qR_s}{nkT}\exp[\ln(I)]$$

$$\Rightarrow V = \frac{nkT}{q}\ln I - \frac{nkT}{q}\ln(AA^{*}T^{2}) + \frac{n\cancel{kT}}{\cancel{q}}\cdot\frac{\cancel{q}\Phi_b}{\cancel{kT}} + \frac{\cancel{nkT}}{\cancel{q}}\cdot\frac{\cancel{q}R_s}{\cancel{nkT}}\exp[\ln(I)]$$

$$\Rightarrow V = \frac{nkT}{q}\ln I - \frac{nkT}{q}\ln(AA^{*}T^{2}) + n\Phi_b + R_s\exp[\ln(I)] \quad (5)$$

Taking into account that $d(e^{x})/dx=e^{x}$, the derivative $dV/d(\ln I)$ of Eq.(5) gives:

$$dV = d(\frac{nkT}{q}\ln I) - d(\frac{nkT}{q}\ln(AA^{*}T^{2})) + d(n\Phi_b) + d(R_s\exp[\ln(I)])$$

$$\Rightarrow dV = \frac{nkT}{q}d(\ln I) - 0 + 0 + (R_s\exp[\ln(I)])d(\ln I)$$

$$\Rightarrow \frac{dV}{d(\ln I)} = \frac{nkT}{q} + R_s\exp[\ln(I)]$$

$$\Rightarrow \boxed{\frac{dV}{d(\ln I)} = \frac{nkT}{q} + I\cdot R_s} \quad (6)$$

From the linear region of graph $\frac{dV}{d(\ln I)} - I$, we can calculate R_S from the slope and n from the intercept of the straight line with Y-axis:

$$\boxed{\text{Slope} = R_s}$$

$$\text{Intercept} = \frac{nkT}{q} \Rightarrow \boxed{n = \frac{q}{kT}\cdot\text{intercept}}$$

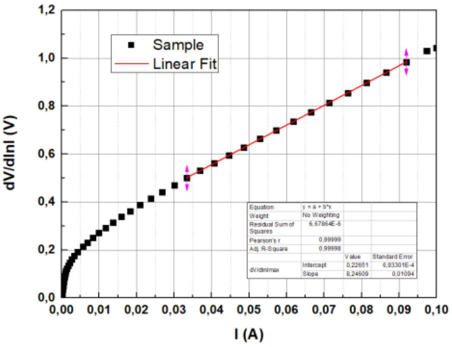

Fig. 2.5: Graph of dV/dlnI vs

From equation (5) and since $\ln(a)+\ln(b)=\ln(a)-\ln(1/b)=\ln(a/b)$ and $x=e^{\ln(x)}$ we have:

Eq.(5): $V = \frac{nkT}{q}\ln I - \frac{nkT}{q}\ln(AA^{*}T^{2}) + n\varphi_b + R_s \exp[\ln(I)]$

$$= \frac{nkT}{q}[\ln I\text{-}\ln(AA^{*}T^{2})] + n\Phi_b + R_s \cdot I$$

$$\Rightarrow V - \frac{nkT}{q}\ln\left(\frac{I}{AA^{*}T^{2}}\right) = n\Phi_b + R_s \cdot I$$

We set: $H(I) = V - \frac{nkT}{q}\ln\left(\frac{I}{AA^{*}T^{2}}\right)$ and the above equation becomes:

$$\boxed{H(I) = n\Phi_b + I \cdot R_s}$$

From the linear region of graph $H(I) - I$, we can calculate R_s from the slope and Φ_b from the intercept:

$$\boxed{\text{Slope} = R_s}$$

$$\text{Intercept} = n\Phi_b \Rightarrow \boxed{\Phi_b = \frac{\text{Intercept}}{n}}$$

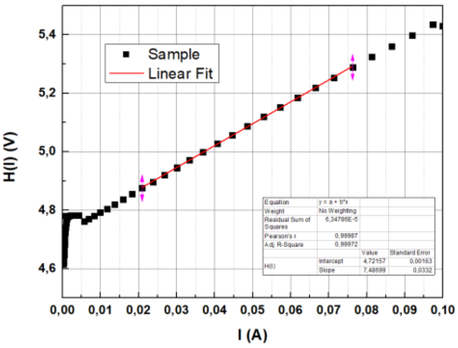

Equation	y = a + b*x		
Weight	No Weighting		
Residual Sum of Squares	6,34786E-5		
Pearson's r	0,99987		
Adj. R-Square	0,99972		
		Value	Standard Error
H(I)	Intercept	4,72157	0,00163
	Slope	7,48699	0,0332

Fig. 2.6: Graph of H versus I

Appendix 3

GIXRD measurements

In the following fig. 3.1 GIXRD measurements are presented. The measured sample was X29 (55% Ar, 47% O_2 & 47% N_2). The sample was not removed during all measurements. Different incident angles were tested in order to find the peak that gives the maximum intensity. The angles were from 0.5^o to 1.6^o. As seen from figure, the peak with the maximum intensity was 1.6^o, as a result all GIXRD measurements of this master thesis were performed at 1.6^o.

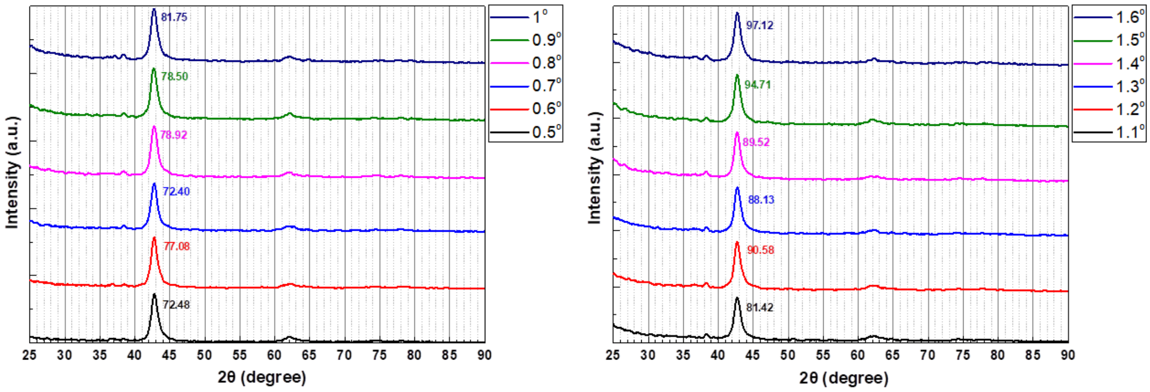

Fig. 3.1: GIXRD measurements in different incident angles

BIBLIOGRAPHY

[1] J. Osorio-Guillén, S. Lany, and A. Zunger, "Nonstoichiometry and hole doping in NiO," *AIP Conf. Proc.*, vol. 1199, pp. 128–129, 2009, doi: 10.1063/1.3295330.

[2] R. Karsthof, M. Grundmann, A. M. Anton, and F. Kremer, "Polaronic interacceptor hopping transport in intrinsically doped nickel oxide," *Phys. Rev. B*, vol. 99, no. 23, p. 235201, 2019, doi: 10.1103/PhysRevB.99.235201.

[3] M. Leskelä and M. Ritala, "Atomic layer deposition (ALD): From precursors to thin film structures," *Thin Solid Films*, vol. 409, no. 1, pp. 138–146, 2002, doi: 10.1016/S0040-6090(02)00117-7.

[4] S. Sajid *et al.*, "Breakthroughs in NiOx-HTMs towards stable, low-cost and efficient perovskite solar cells," *Nano Energy*, vol. 51, pp. 408–424, 2018, doi: 10.1016/j.nanoen.2018.06.082.

[5] T. S. Yang *et al.*, "Atomic layer deposition of nickel oxide films using Ni(dmamp) 2 and water," *J. Vac. Sci. Technol. A Vacuum, Surfaces, Film.*, vol. 23, no. 4, pp. 1238–1243, 2005, doi: 10.1116/1.1875172.

[6] I. Sta, M. Jlassi, M. Hajji, and H. Ezzaouia, "Structural, optical and electrical properties of undoped and Li-doped NiO thin films prepared by sol-gel spin coating method," *Thin Solid Films*, vol. 555, pp. 131–137, 2013, doi: 10.1016/j.tsf.2013.10.137.

[7] S. Yue *et al.*, "Efficacious engineering on charge extraction for realizing high-efficient perovskite solar cells," *Energy Environ. Sci.*, vol. 10, no. 2, pp. 2570–2578, 2013, doi: 10.1039/c7ee02685d.

[8] C. Aivalioti *et al.*, "Transparent All-Oxide Hybrid NiO:N/TiO2 Heterostructure for Optoelectronic Applications," *Electronics*, vol. 10, no. 988, pp. 1–18, 2021, doi: 10.3390/electronics10090988.

[9] S. Dey, S. Nag, S. Santra, S. K. Ray, and P. K. Guha, "Voltage-controlled NiO/ZnO p–n heterojunction diode: a new approach towards selective VOC sensing," *Microsystems Nanoeng.*, vol. 6, no. 1, pp. 1–9, 2020, doi: 10.1038/s41378-020-0139-1.

[10] J. Zhang and A. Yu, "Nanostructured transition metal oxides as advanced anodes for lithium-ion batteries," *Sci. Bull.*, vol. 60, no. 9, pp. 823–838, 2015, doi: 10.1007/s11434-015-0771-6.

[11] P. C. Rosado *et al.*, "Immobilization of His-tagged proteins on NiO foams for recyclable enzymatic reactors," *Appl. Surf. Sci.*, vol. 537, no. September 2020, p. 147848, 2021, doi: 10.1016/j.apsusc.2020.147848.

[12] A. Charisiadis *et al.*, "Photoelectrochemical properties of dyads composed of porphyrin/ruthenium catalyst grafted on metal oxide semiconductors," *Dye. Pigment.*, vol. 185, p. 108908, 2021, doi: 10.1016/j.dyepig.2020.108908.

[13] Z. Zou, J. Ye, K. Sayama, and H. Arakawa, "Direct splitting of water under visible light irradiation with an oxide semiconductor photocatalyst," *Nature*, vol. 414, no. 2000, pp. 625–627, 2001.

[14] Z. Wang, X. Wang, S. Cong, F. Geng, and Z. Zhao, "Fusing electrochromic technology with other advanced technologies: A new roadmap for future development," *Mater. Sci. Eng. R Reports*, vol. 140, p. 100524, 2020, doi:

10.1016/j.mser.2019.100524.

[15] M. Patel, H. S. Kim, H. H. Park, and J. Kim, "Active Adoption of Void Formation in Metal-Oxide for All Transparent Super-Performing Photodetectors," *Sci. Rep.*, vol. 6, pp. 1–11, 2016, doi: 10.1038/srep25461.

[16] R. Karsthof, H. von Wenckstern, J. Zúñiga-Pérez, C. Deparis, and M. Grundmann, "Nickel Oxide–Based Heterostructures with Large Band Offsets," *Phys. Status Solidi Basic Res.*, vol. 257, no. 7, 2020, doi: 10.1002/pssb.201900639.

[17] M. Grundmann *et al.*, "Oxide bipolar electronics: Materials, devices and circuits," *J. Phys. D. Appl. Phys.*, vol. 49, no. 21, 2016, doi: 10.1088/0022-3727/49/21/213001.

[18] J. Tirado, M. Vásquez-Montoya, C. Roldán-Carmona, and M. Ralaiarisoa, "Air-Stable n−i−p Planar Perovskite Solar Cells Using Nickel Oxide Nanocrystals as Sole Hole-Transporting Material." 2019.

[19] A. M. Elseman, S. Sajid, A. E. Shalan, S. A. Mohamed, and M. M. Rashad, "Recent progress concerning inorganic hole transport layers for efficient perovskite solar cells," *Appl. Phys. A Mater. Sci. Process.*, vol. 125, no. 7, pp. 1–12, 2019, doi: 10.1007/s00339-019-2766-7.

[20] M. L. Grilli *et al.*, "Effect of growth parameters on the properties of RF-sputtered highly conductive and transparent p-type NiOx films," *Semicond. Sci. Technol.*, vol. 31, no. 5, 2016, doi: 10.1088/0268-1242/31/5/055016.

[21] J. D. Hwang and T. H. Ho, "Effects of oxygen content on the structural, optical, and electrical properties of NiO films fabricated by radio-frequency magnetron sputtering," *Mater. Sci. Semicond. Process.*, vol. 71, no. May, pp. 396–400, 2017, doi: 10.1016/j.mssp.2017.09.002.

[22] S. Nandy, U. N. Maiti, C. K. Ghosh, and K. K. Chattopadhyay, "Enhanced p-type conductivity and band gap narrowing in heavily Al doped NiO thin films deposited by RF magnetron sputtering," *J. Phys. Condens. Matter*, vol. 21, no. 11, 2009, doi: 10.1088/0953-8984/21/11/115804.

[23] D. Adler and J. Feinleib, "Electrical and optical properties of narrow-band materials," *Phys. Rev. B*, vol. 2, no. 8, pp. 3112–3134, 1970, doi: 10.1103/PhysRevB.2.3112.

[24] S. G. Park *et al.*, "Improved polaronic transport under a strong Mott-Hubbard interaction in Cu-substituted NiO," *Inorg. Chem. Front.*, vol. 7, no. 4, pp. 853–858, 2020, doi: 10.1039/c9qi01052a.

[25] I. Popescu, Z. Skoufa, E. Heracleous, A. Lemonidou, and I. C. Marcu, "A study by electrical conductivity measurements of the semiconductive and redox properties of Nb-doped NiO catalysts in correlation with the oxidative dehydrogenation of ethane," *Phys. Chem. Chem. Phys.*, vol. 17, no. 12, pp. 8138–8147, 2015, doi: 10.1039/c5cp00392j.

[26] J. Keraudy, A. Ferrec, M. Richard-Plouet, J. Hamon, A. Goullet, and P. Y. Jouan, "Nitrogen doping on NiO by reactive magnetron sputtering: A new pathway to dynamically tune the optical and electrical properties," *Appl. Surf. Sci.*, vol. 409, pp. 77–84, 2017, doi: 10.1016/j.apsusc.2017.02.229.

[27] S. Tangwancharoen, P. Thongbai, T. Yamwong, and S. Maensiri, "Dielectric and electrical properties of giant dielectric (Li, Al)-doped NiO ceramics," *Mater. Chem. Phys.*, vol. 115, no. 2–3, pp. 585–589, 2009, doi:

10.1016/j.matchemphys.2009.01.004.

[28] D. Dong *et al.*, “Enhanced electrochromism in short wavelengths for NiO:(Li, Mg) films in full inorganic device ITO/NiO:(Li, Mg)/Ta2O5/WO3/ITO,” *Electrochim. Acta*, vol. 263, pp. 277–285, 2018, doi: 10.1016/j.electacta.2018.01.049.

[29] C. K. Wen, Y. Q. Xin, S. C. Chen, T. H. Chuang, P. J. Chen, and H. Sun, “Comparison of microstructural and optoelectronic properties of NiO:Cu thin films deposited by ion-beam assisted rf sputtering in different gas atmospheres,” *Thin Solid Films*, vol. 677, no. March, pp. 103–108, 2019, doi: 10.1016/j.tsf.2019.03.018.

[30] S. Sriram, A. Thayumanavan, and K. Ravichandran, “Influence of nitrogen doping on properties of NiO films,” *Surf. Eng.*, vol. 32, no. 3, pp. 207–211, 2016, doi: 10.1179/1743294414Y.0000000380.

[31] F. Gillot, J. Oró-Solé, and M. R. Palacín, “Nickel nitride as negative electrode material for lithium ion batteries,” *J. Mater. Chem.*, vol. 21, no. 27, pp. 9997–10002, 2011, doi: 10.1039/c0jm04144k.

[32] M. Nolan, R. Long, N. J. English, and D. A. Mooney, “Hybrid density functional theory description of N- and C-doping of NiO,” *J. Chem. Phys.*, vol. 134, no. 22, 2011, doi: 10.1063/1.3596949.

[33] A. A. Farghali, W. M. A. El Rouby, and M. S. Abdel-Wahab, “Structural, optical and photo-catalytic activity of Nb-doped NiO thin films,” *Dig. J. Nanomater. Biostructures*, vol. 11, no. 3, pp. 811–819, 2016.

[34] K. O. Ukoba, F. L. Inambao, and A. C. Eloka-Eboka, “Fabrication of affordable and sustainable solar cells using NiO/TiO2 P-N heterojunction,” *Int. J. Photoenergy*, vol. 2018, 2018, doi: 10.1155/2018/6062390.

[35] R. Surmenev *et al.*, “Radio Frequency Magnetron Sputter Deposition as a Tool for Surface Modification of Medical Implants,” *Mod. Technol. Creat. Thin-film Syst. Coatings*, 2017, doi: 10.5772/66396.

[36] N. K. Jain, M. Sawant, and S. H. Nikam, “Metal Deposition: Plasma-Based Processes,” *Encycl. Plasma Technol.*, no. September 2020, pp. 722–740, 2017, doi: 10.1081/e-eplt-120053919.

[37] I. Μιχαήλ, “Μελέτη Οξειδίου του Νικελίου (NiO) για ηλεκτροχρωμικές διατάξεις,” 2011.

[38] A. Salman Ali, “Application of Nanomaterials in Environmental Improvement,” *Nanotechnol. Environ.*, pp. 1–20, 2020, doi: 10.5772/intechopen.91438.

[39] M. Kouh and T. Lymperopoulou, “Scanning electron microscope with energy dispersive X – ray spectrometer (SEM – EDAX),” .

[40] G. Kiriakidis and V. Binas, *Introduction to electron microscopy*. Heraklio, 2014.

[41] O. Marti, B. Drake, and P. K. Hansma, “Atomic force microscopy of liquid-covered surfaces: Atomic resolution images,” *Appl. Phys. Lett.*, vol. 51, no. 7, pp. 484–486, 1987, doi: 10.1063/1.98374.

[42] G. Binnig, C. F. Quate, and C. Gerber, “Atomic Force Microscope,” *Phys. Rev. Lett.*, vol. 56, no. 9, p. 5, 1986.

[43] B. Voigtländer, *Atomic Force Microscopy*. 2019.

[44] C. O. Colpan, Y. Nalbant, and M. Ercelik, *Fundamentals of Fuel Cell Technologies*, vol. 4. 2018.

[45] R. Paynter, “XPS Theory,” *Lecture*, 2000.

[46] A. G. Shard, “Practical guides for x-ray photoelectron spectroscopy: Quantitative XPS,” *J. Vac. Sci. Technol. A*, vol. 38, no. 4, p. 041201, 2020, doi: 10.1116/1.5141395.

[47] S. Hofmann, *Auger- and X-Ray Photoelectron Spectroscopy in Materials Science*. 2013.

[48] D. G. R. William D. Callister, Jr., *Materials Science and Engineering An Introduction*, Eighth., vol. 1. 2010.

[49] M. Aftab, M. Z. Butt, D. Ali, F. Bashir, and Z. H. Aftab, “Impact of copper doping in NiO thin films on their structure, morphology, and antibacterial activity against Escherichia Coli,” *Ceram. Int.*, vol. 46, no. 4, pp. 5037–5049, 2020, doi: 10.1016/j.ceramint.2019.10.247.

[50] M. S. Senthil Saravanan, K. Sivaprasad, P. Susila, and S. P. Kumaresh Babu, “Anisotropy models in precise crystallite size determination of mechanically alloyed powders,” *Phys. B Condens. Matter*, vol. 406, no. 2, pp. 165–168, 2011, doi: 10.1016/j.physb.2010.10.023.

[51] V. Gowthami, P. Perumal, R. Sivakumar, and C. Sanjeeviraja, “Structural and optical studies on nickel oxide thin film prepared by nebulizer spray technique,” *Phys. B Condens. Matter*, vol. 452, pp. 1–6, 2014, doi: 10.1016/j.physb.2014.06.030.

[52] H. Ibach and H. Luth, *Solid-State Physics, an introduction to principles of material science.*, vol. 1. 2015.

[53] L. J. Van Der PAUW, “A method of measuring the resistivity and Hall coefficient on lamellae of arbitrary shape,” *Philips Technical Review*, vol. 20, no. 8. pp. 220–224, 1958, [Online]. Available: http://www.mendeley.com/research/method-measuring-resistivity-hall-coefficient-lamellae-arbitrary-shape/.

[54] D. W. Koon and C. J. Knickerbocker, “What do you measure when you measure resistivity?,” *Rev. Sci. Instrum.*, vol. 63, no. 1, pp. 207–210, 1992, doi: 10.1063/1.1142958.

[55] Β. Καμπυλαυκά, “Λεπτά Υμένια Zn3N2:Παρασκευή, μελέτη και εφαρμογές.,” Πανεπιστήμιο Κρήτης, 2008.

[56] F. F. Chen, *Introduction to Plasma Physics and Controlled Fusion*. 1983.

[57] F. Werner, “Hall measurements on low-mobility thin films,” *J. Appl. Phys.*, vol. 122, no. 13, 2017, doi: 10.1063/1.4990470.

[58] A. I. Hofmann, R. Kroon, and C. Müller, *Doping and processing of organic semiconductors for plastic thermoelectrics*. 2019.

[59] S. M. Sze and K. N. Kwok, *Physics of semiconductor devices*, Third. .

[60] D. K. SCHRODER, *Semiconductor Material and Device Characterization*. 2006.

[61] S. Tetsuo, *Nanostructured Materials for Solar Energy Conversion*. 2006.

[62] V. Ganesh *et al.*, “Structural, morphological, optical and third order nonlinear optical response of spin-coated NiO thin films: An effect of N doping,” *Solid State Sci.*, vol. 86, pp. 98–106, 2018, doi: 10.1016/j.solidstatesciences.2018.10.009.

[63] M. M. A. Jafar, “Comprehensive formulations forthe total normal-incidence optical reflectance and transmittance of thin films laid on thick substrates,” *Eur. Int. J. Sci. Technol.*, vol. 2, no. 5, pp. 214–274, 2013.

[64] N. A. Al-Ahmadi, F. A. Ebrahim, H. A. Al-Jawhari, R. H. Mari, and M. Henini,

"Impact of doping on the performance of p-type Be-doped AlGaAs Schottky diodes," *Mod. Electron. Mater.*, vol. 3, no. 2, pp. 66–71, 2017, doi: 10.1016/j.moem.2017.06.001.

[65] R. Y. K. Ya.Ya. Kudryk1, V.V. Shynkarenko1, V.S. Slipokurov1, R.I. Bigun2, "Determination of the Schottky barrier height in diodes based on Au-TiB2-n-SiC 6H from the current-voltage and capacitance-voltage characteristics," *Semicond. Physics, Quantum Electron. Optoelectron.*, vol. 17, no. 4, pp. 398–402, 2014.

[66] E. H. Rhoderick and R. H. Williams, *Metal-Semiconductor Contacts*, no. 2. 1988.

[67] S. Sankar Naik and V. Rajagopal Reddy, "Temperature dependency and current transport mechanisms of Pd/V/n-type InP schottky rectifiers," *Adv. Mater. Lett.*, vol. 3, no. 3, pp. 188–196, 2012, doi: 10.5185/amlett.2012.1316.

[68] L. Yuanjie *et al.*, "Extraction of AlGaN/GaN heterostructure Schottky diode barrier heights from forward current-voltage characteristics," *J. Appl. Phys.*, vol. 109, no. 7, 2011, doi: 10.1063/1.3569594.

[69] S. K. Cheung and N. W. Cheung, "Extraction of Schottky diode parameters from forward current-voltage characteristics," *Appl. Phys. Lett.*, vol. 49, no. 2, pp. 85–87, 1986, doi: 10.1063/1.97359.